UNIVERSITÀ
DEGLI STUDI
FIRENZE

DOTTORATO DI RICERCA IN SCIENZE CHIMICHE

CICLO XXVIII

COORDINATORE Prof. ANDREA GOTI

ELECTROCATALYSIS FOR ENERGY PRODUCTION AND STORAGE

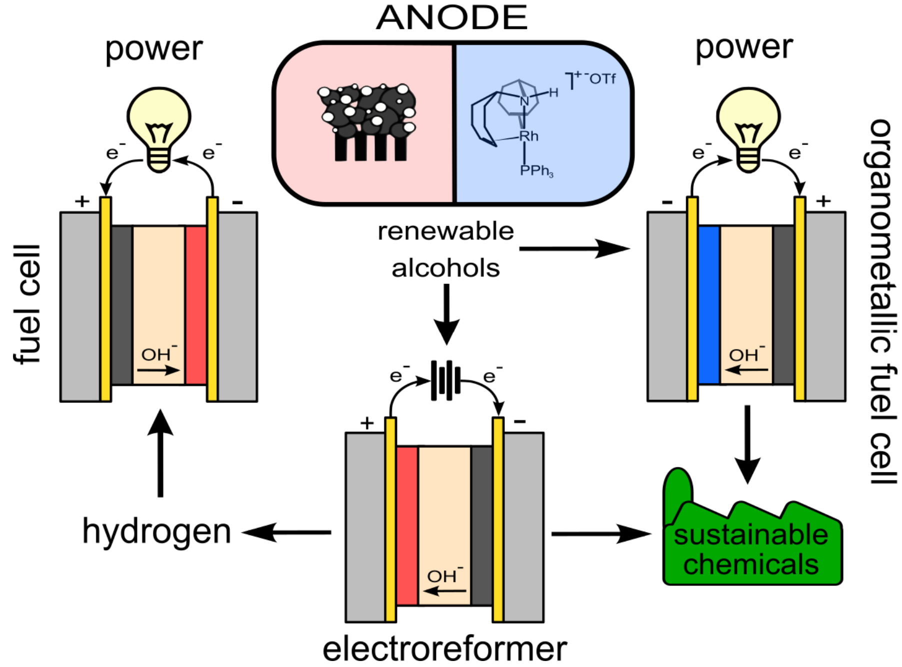

Dottorando
Dott. Marco Bellini

Tutore
Dott. Francesco Vizza

UNIVERSITÀ
DEGLI STUDI
FIRENZE

DOTTORATO DI RICERCA IN SCIENZE CHIMICHE

CICLO XXVIII

COORDINATORE Prof. ANDREA GOTI

ELECTROCATALYSIS FOR ENERGY PRODUCTION AND STORAGE

Settore Scientifico Disciplinare CHIM/03

Dottorando	**Tutore**
Dott. Marco Bellini	Dott. Francesco Vizza

Coordinatore
Prof. Andrea Goti

Anni 2012/2015

Questo lavoro di tesi è stato svolto presso l'Istituto di Chimica dei Composti OrganoMetallici del Consiglio Nazionale delle Ricerche, sede di Firenze.

This thesis was developed at the Institute of Chemistry of the Organometallic Compounds of the Natioan Research Council of Florence.

Ai "ragazzi" dell'ICCOM,
per i bei momenti trascorsi assieme.

To the ICCOM staff,
thank you for the beautiful experience.

Omnia in mensura et numero et pondere[*]

---

[*] Frase scritta nel fregio dell’aula magna del Dipartimento di Chimica “Giacomo Ciamician” dell’Università di Bologna, Alma Mater Studiorum. La frase è stata adattata da “Omnia in mensura et numero et pondere disposuisti”, Sapienza (11,20), e rappresenta i tre principi base della chimica moderna.

Sentence written in the aula magna of the Chemistry Departemnt “Giacomo Ciamician” of the University of Bologna, Alma Mater Studiorum. The sentence is adapted from “Omnia in mensura et numero et pondere disposuisti”, Book of Wisdom (11,20), and summarizes the three main principles of the modern chemistry.

Table of Contents

List of the main abbreviation

AE: Alkaline Electrolyser

AEM: Anion Exchange Membrane

AEMFC: Anion Exchange Membrane Fuel Cell

AOR: Alcohol Oxidation Reaction

C: Carbon black

CC: Carbon Cloth

CE: Counter Electrode

CV: Cyclic Voltammetry

DAFC: Direct Alcohol Fuel Cell

EASA: Electrochemical Active Surface Area

EDX: Energy Dispersive X-rays spectroscopy

EG: Ethylene Glycol

FC: Fuel Cell

G: Glycerol

GDL: Gas Diffusion Layer

J: current density

KtjBk: Ketjen Black

HER: Hydrogen Evolution Reaction

HOR: Hydrogen Oxidation Reaction

HR-TEM: High Resolution Transmission Electron Microscopy

ICP-MS: Inductively Coupled Plasma – Mass Spectroscopy**MEA**: Membrane Electrode Assembly

NP: NanoParticle

OCV: Open Circuit Voltage

OER: Oxygen Evolution Reaction

OMFC: OrganoMetallic Fuel Cell

ORR: Oxygen Reduction Reaction

OTf: Trifluoromethanesulfonate

PEM: Polymer Exchange Membrane

PEMFC: Proton Exchange Membrane Fuel Cell

Pc: Phtalocyanine

PTFE: PolyTetraFluoroEthylene

RE: Reference Electrode

RDE: Rotating Disk Electrode

RHE: Reference Hydrogen Electrode

Sa: Specific activity

STEM: Scanning Transmission Electron Microscopy

TEM: Transmission Electron Microscopy

THF: Tetrahydrofuran

TON: Turn Over Number

UPD: Under Potential Deposition

WE: Working Eectrode

wt. %: weight ratio

XRPD: X-Rays Powder Diffraction

1,2-P: 1,2-propanedeiol

1,3-P: 1,3-propanediol

1,4-B: 1,4-butanediol

1. Abstract

The world’s system of production and exploitation of fossil fuels is reaching a breaking point: finiteness, pollution and geopolitical problems mean that an energy economy based on these resources is no longer “sustainable”. The development of a new energy strategy is now a priority and renewable energies are the main candidates for replacing fossil fuels, especially for electrical energy production.

Solar energy is the most abundant and easily available renewable source but it is neither constant nor distributed equally over the surface of the globe. Hydrogen and biofuels, like bioethanol, have the potential, as solar energy storage vectors, to play a fundamental role in the development of a new energy era based on renewable sources. There are two electrochemical devices, which will be fundamental for the realization of such an energy system. Firstly, fuel cells, which are devices that can convert cleanly the chemical energy stored in hydrogen or bioalcohols into electrical energy and secondly, electrolyzers, which are the best candidates for storing electric energy produced from renewable sources as hydrogen.

The focus of this thesis is the development of innovative anodic electrocatalysts for three energy-related devices: a) Direct Alcohol Fuel Cells (DAFCs), b) H_2/O_2 fed Anion Exchange Membrane Fuel Cells (AMFCs) and c) anion exchange membrane alcohol electroreformers. Catalysts have been synthesized and characterized for their morphology and electrochemical activity, both in half-cell and in the complete cell systems. An anion exchange membrane is used in all devices because the alkaline environment is the most promising way to overcome the problems that hinder the development of fuel cells and electrolyzers that belong to the state of the art. For example, in alkaline media, alcohol oxidation kinetics are faster compared the traditional proton exchange membrane based devices. In Chapter 2 a description of the state of the art of fuel cells and electrolyzers is provided and describes the advantages in replacing the traditional proton exchange membrane electrolytes with anion exchange membranes.

Chapter 3 introduces the OrganoMetallic Fuel Cell (OMFC), which employs a rhodium complex as anodic electrocatalyst. In contrast to established technologies based on metal nanoparticles, in OMFCs every single metal atom is catalytically active and thereby reduces the metal loading of fuel cell electrodes by several orders of magnitude. Because the performance of the metal complexes can be optimized based on established methods of synthetic organometallic and coordination chemistry, the approach via OMFC's – though in its infancies – should allow to truly design electrodes which in principle can operate with earth-abundant, inexpensive metals. Organometallic fuel cells catalyse the selective electrooxidation of renewable diols, simultaneously providing high power densities and chemicals of industrial importance. It is shown that the unique organometallic complex $[Rh(OTf)(trop_2NH)(PPh_3)]$, employed as molecular active site in an anode of an OMFC, selectively oxidizes a number of renewable diols, such as ethylene glycol (EG), 1,2-propanediol (1,2-P), 1,3-propanediol (1,3-P), and 1,4-butanediol (1,4-B) to their corresponding mono-carboxylates. The electrochemical performance of this molecular catalyst is discussed, with the aim to achieve cogeneration of electricity and valuable chemicals in a highly selective electrooxidation from diol precursors.

Removal of platinum from polymer electrolyte membrane fuel cells is one of the most commonly cited objectives for researchers in this field.

In Chapter 4 is described a platinum free anion exchange membrane fuel cell (AEM-FC) that employs nanostructured Pd anode and Fe-Co cathode electrocatalysts. AEM-FC tests run on dry hydrogen and pure air show peak power densities of more than 200 mW cm^{-2}. Such high power output is shown to be due to a nanoparticle Pd anode catalyst with a composite Vulcan XC-72 carbon-CeO_2 support that exhibits enhanced kinetics for hydrogen oxidation in alkaline media.

In chapter 5, a nanostructured anodic electrocatalyst (Au@Pd supported on Vulcan XC-72) is employed in an alkaline alcohol electroreformer, which provides a net energy saving for hydrogen production compared to traditional water electrolysis. In addition, hydrogen production is coupled with the contemporaneous conversion of a bioalcohol into valuable chemicals, for example lactate and glycolate, which are industrially relevant feedstock. Traditional nanostructured palladium based anodic electrocatalysts are not selective in the oxidation of renewable polyols to carboxylic compounds. Modifying the nanoparticle architecture is a way to increase this selectivity. In addition, the energy consumption for hydrogen production by electrolysis was lowered from the 50-60 kWh $kg_{H_2}^{-1}$ of a traditional electrolyzer to ca. 20 kWh $kg_{H_2}^{-1}$.

Chapter 6 summarizes the conclusions of this thesis. The results of this research clearly demonstrate that the architecture of the anodic electrocatalyst plays a fundamental role in the enhancement of the electrochemical performances of devices such as OMFCs, AMFCs and alcohol electroreformers. In addition, the anodic catalyst architecture has the important role for driving the selectivity of the alcohol oxidation reaction towards carboxylic compounds in OMFCs and electroreformers. These devices produce chemicals of industrial relevance with a contemporaneous release of energy or hydrogen at low temperature and atmospheric pressure, matching several principles of sustainable "green chemistry".

2. Introduction

2.1. The energy issue, a short overview

Energy plays a crucial role in every human activity in industrialized countries [1,2], in fact, starting from the 19th century the exploitation of fossil energy sources, oil, coal and natural gas, has allowed the biggest economic, technological and population boom in the history of humanity [1,3,4]. Fossil fuels have allowed this huge development due to their high energy density and due to the easiness and cheapness of their extraction and transportation [3]; indeed every activity of the industrialized world, nowadays, is directly or indirectly reliant on fossil fuel sources [2,4]. In addition to fossil fuels, humanity has also used over the last two centuries other energy sources, but up till now oil, coal and natural gas are still the most employed, as represented in figure 2.1-a [5].

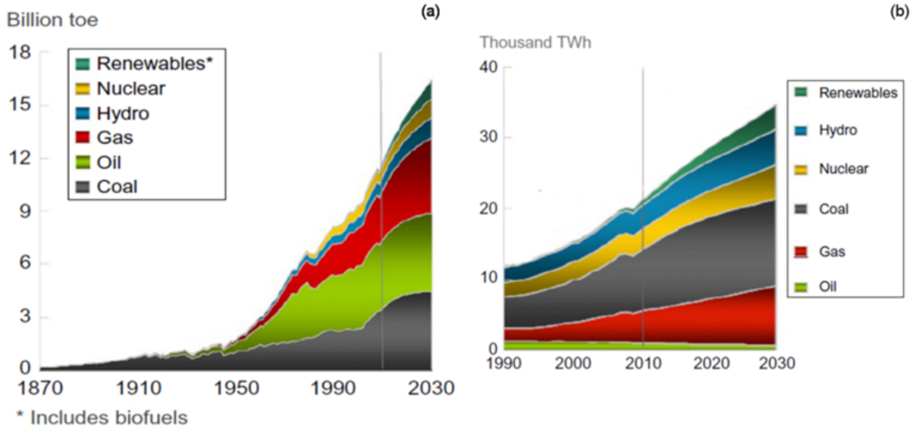

Figure 2.1: (a) Global energy consumption by type from 1870 to 2030 (toe: tons of equivalent oil). The grey line represents the year 2010; (b) Word electric power generation by source type from 1990 to 2030. The grey line represents the year 2010 [5].

Electricity is an intermediate energy form that has played a key role in the development of modern society during the 20th century. It is now employed in multiple aspects of human life, from lighting to heating to powering electronic devices [6]. During the 21st century electrical energy will gain even more importance, becoming the primary energy source; for example in the near future electricity will have a key role to play in the automotive field [6]. Right now the major part of electric energy is produced from fossil energy sources (figure 2.1-b): fossil fuels are burned to produce heat that is converted into mechanical work and then in electricity [1,5,6].

During the last decades of the 20th century, limitations in the employment of fossil fuel sources became more important than the benefits of the easiness of extraction and the high energy density. The main limitations of fossil fuel sources are:

> **Finiteness.** Oil, coal and natural gas are non-renewable resources, this means that the human consumption rate of these goods is higher than the natural rate to regenerate them [3]: the amount of extracted fossil fuels will reach a maximum and then it will decrease as described by the Marion King Hubbert's "bell shaped curve" [7]. This trend is inversed with respect the annual world energy consumption, that increases by 2% every year [1] due to the expanding world population and economic development, especially in the "emerging economies" like India, China and Brazil [8,9].
>
> **Energy security.** The main oil, coal and natural gas deposits are located only in particular regions of the globe. For example, oil fields are mostly concentrated in the Middle East and in North Africa [10].

These areas suffer from political instability, so countries in these regions can limit fossil fuel production or increase oil prices thus taking advantage of periods of international instability. The main example of this was the “oil crisis” of 1970s [10–12].

Environment. Burning coal, oil and their derivative products and burning natural gas has a negative impact on the environment due to the release of several pollutants into the atmosphere [3]. In particular, combustion reactions release into the atmosphere carbon monoxide (CO) sulfur and nitrogen oxides (NO_x and SO_x), Volatile Organic Compounds (VOCs), heavy metals and Particulate Matter (PM) [13,14]. These pollutants are responsible for damaging the environment, like acid rain and the depletion of the ozone layer; epidemiologic studies show the link between these pollutants and several human diseases, from cancer to respiratory and cardiovascular diseases [3,13,14]. The main product of fossil fuel combustions is CO_2, that together with CO and CH_4 are the most relevant anthropogenic green-house gases. The earth’s climate is changing; most of the scientific community believe that anthropogenic green-house gases contribute to increasing the green-house effect and so have a role in climate changing [9,15,16].

Planning a new energy strategy is now a priority; there is no unequivocal solution in finding an energy source that can ensure energy supply security and low environmental impact. Any new energy source should meet the energy demand of several services, from industry to household and transportation [3]. Renewable energy sources are the main candidates in replacing fossil fuels. First of all the regeneration rate of these sources is quicker than their consumption rate, so in principle, they are inexhaustible [3]. Renewable sources are widespread all over the world, avoiding the problem of the “concentration” of the energy source in only some specific area. In addition there is a huge variety of renewable energy sources, so each region can choose the energy source that fits its needs; the principle of the diversification of the energy source is another opportunity to create an energetic system widespread all over the world, matching the energy security supply needs [17,18]. Finally, renewable energies sources have a lower environmental impact with respect to fossil energy sources [9,15,16].

There are several renewable sources that can be used to produce energy, especially electrical energy. Most of them are directly or indirectly related to the energy transported to the earth by solar radiation. The most common renewable energy sources are: thermal or photovoltaics from sunlight, wind, hydroelectricity and geothermal heat [1,3]. Solar energy can be converted into energy vectors, like liquid fuels, by the fixation of the CO_2 into organic compounds by photosynthetic processes; this aspect will be treated in detail in paragraph 2.1.2.

There are two main drawbacks to the exploitation of renewable energy sources, which limits their large diffusion, especially for electrical energy production:

> **Low efficiency.** The radiation coming from the sun by year is the most abundant energy source that reaches the earth; it is 10000 times more plenty than the energy consumed by humanity over the same time [19]. Unfortunately, until now there isn’t a cheap process that can harvest this huge amount of energy with high efficiency, in order to replace the easiness and cheapness of energy extraction by the conventional energy sources [3].

Discontinuity of the supply. At first approximation, conventional power plants can produce energy “on demand”, so industrialized society is built upon the principle that energy can be used when it is requested. Unfortunately, most of renewable energy sources have an intermittent nature; wind and solar radiation are the best examples of this non programmability in energy supply. For example after sunset there is a huge consumption of electrical energy for lighting, but this energy can’t be supplied directly by solar fed photovoltaics [20]. So it is important to implement renewable electrical energy power plants with systems of storing the produced energy so that it may be released when needed [3].

2.1.1. Energy Vectors and “Hydrogen Economy”

An energy vector is a material, a device or a chemical compound that can store the surplus of energy produced and release it on demand in different times and places [20,21]. This concept was introduced by John O’Mara Bockris in the 1970s during the energy crisis. The Bockris idea was to store the surplus of electric energy produced by nuclear power plants synthesizing molecular hydrogen by water electrolysis; when the energy demand was higher than production, hydrogen could be converted into electrical energy in fuel cells or into mechanical energy in internal combustion engines [21]. This last choice is not the best solution due to the low energy efficiency of thermal engines and due to the production of NO_x in the fuming exhaust of combustion [3]. In principle the use of hydrogen both as fuel and as an energy vector can substitute the fossil fuel energetic system, so hydrogen could be the basis for a new energy era: “the hydrogen economy” [21].

The hydrogen economy seeks to solve the problem of discontinuity in the energy supply from renewable resources [21]. There are several ways to convert sunlight in hydrogen, for example by photocatalysis [22] or by bacteria [23]; actually the only process commercially available is the exploitation of photovoltaic electrical energy to obtain H_2 and O_2 by water electrolysis [24]. The production of hydrogen from non-polluting sources is called the “hydrogen environmental economy”, due to the fact that renewable resources have a lover environmental impact with respect traditional fuels [3,25].

There are several limitations in the development of the hydrogen economy, especially due to the storage, distribution and safety problems related to this gas: hydrogen has a low density, so it must be compressed at more than 700 bar to store large amounts in cylinders; these issues limit hydrogen use especially in automotive applications [23,26]. In addition, water electrolysis is still an expensive process for hydrogen production: it requires huge amounts of electrical energy, circa 50-60 kWh $kg_{H_2}^{-1}$ [27,28], so it remains noncompetitive with traditional industrial processes for hydrogen synthesis, despite the fact that hydrogen obtained from electrolytic water splitting has a 99.999% assay [28]. Traditionally about 97% of hydrogen is produced from fossil fuels, in particular by methane steam reforming and coal gasification. Methane and coal react at high temperature with $H_2O_{(g)}$ to form “syngas”, a mixture of CO and H_2, that again reacts with water steam at high temperature in the presence of iron based catalysts to generate H_2 and CO_2 (water gas shift reaction) [29]. The main drawback of these processes is the production of CO_2, a well-known green-house gas. In addition the hydrogen obtained contains CO impurities, so it can’t be used in fuel cells to generate electricity because the major part of the commercially available fuel cells employ platinum based catalyst, which suffer from CO poisoning; this phenomenon limits seriously fuel cell efficiency [30]. So, the use of hydrogen today is still limited to the chemical industry, in particular the main uses are the synthesis of ammonia and in the petrochemical industry [23].

2.1.2. Biomass and bioalcohols

Solar energy can be stored by CO_2 fixation into organic compounds, like sugars, by photosynthetic processes in biomass. Until the beginning of the 20th century, biomass was the main energy source and it still has a huge relevance nowadays [31,32]. Biomass is in principle a renewable energetic source if it is continuously renewed by seeding new plants and trees; in addition biomass exploitation has a quasi-zero CO_2 emission impact because the CO_2 produced by their exploitation is fixed again by photosynthesis in new plants [31].

There are several ways to exploit biomass for energy production, for example burning directly biomass as fuel for heating purposes [33,34]. The production of liquid and gaseous fuels from biomass is an attractive use of these energy sources; in particular bioethanol (EtOH) and biodiesel are very interesting biomass derivatives due to their employment for electric energy generation and in automotive fuels [3,34–36]. Burning these fuels in an internal combustion engine has a zero CO_2 balance but it is not the best choice because the combustion reaction produces pollutant gases, like NO_x, and particulate matter [33]. Fuel cells have a lower environmental impact in the exploitation of bioethanol: a particular class of fuel cells, called Direct Alcohol Fuel Cells (DAFCs), can directly convert ethanol and other short chain alcohols to electrical energy, working at low temperatures and atmospheric pressure with zero-emission of pollutants [3,37].

Bioethanol is mostly produced from sugar fermentation; corn, sugarcane and sugar beet are the main sources of sugars for ethanol production [38–40]. These biomasses are involved in the food chain so there is the danger to create a competition between food production and fuel production [33]. “Second generation biomass” resolves this problem because biofuels are produced from not-food biomass sources, for example bioethanol can be produced from lignocellulose hydrolysis and from urban wastes [41]. Methanol (MeOH), ethylene glycol (EG) and 1,2-propanediol (1,2-P) are other interesting renewable alcohols obtained from second generation biomass: from lignocellulose transformation processes [3]. Glycerol is another renewable alcohol obtained from not-food sources: it is a biodiesel byproduct [42].

2.1.2.1. The EROEI parameter for bioalcohols

The exploitation of an energy resource has always efficiency lower than 100% because some energy is spent in the operations necessary to make this energy source available. For example, to use the energy stored in oil, energy is spent in extracting, refining and transporting it. The EROEI parameter, Energy Return for Energy Invested, describes the amount of energy that an energy resource can return as compared to the energy spent to recover it (eq. 2.1) [3].

$$EROEI = \frac{\text{"}energy\ obtained\ from\ the\ source\text{"}}{\text{"}energy\ spent\ in\ the\ source\ production\text{"}} \qquad \text{Eq. 2.1}$$

In order to obtain an energy gain from the exploitation of a resource, the EROEI must be larger than 1. Oil has an EROEI value of 40, so the energy amount extracted from this source is forty times higher than the energetic costs required for its extraction and refining [43]. The exploitation of biofuels should take into account the EROEI parameter, to obtain a real energetic gain from the use of these resources. For example, ethanol obtained from the first generation of biomasses, like corn, has an EROEI parameter lower than 1, so the energy spent for ethanol production is higher than the energy extracted from this fuel [44]. Fortunately, the production of ethanol and other bioalcohols from second generation biomass is a more efficient process: in some cases the EROEI values are larger than 10, in particular 8 for ethanol obtained from sugar cane and 38 for ethanol obtained from lignocellulose steam reforming [3].

2.2. Fuel Cells

A fuel cell is an electrochemical device which converts the free energy of the spontaneous chemical reaction between a fuel and an oxidant into DC (Direct Current) electrical energy and heat (figure 2.2) [30]. Hydrogen is the most common fuel, but even hydrocarbons like methane or alcohols (EtOH and MeOH) can be used. Generally the oxidant is pure or atmospheric oxygen [3,45]. Fuel cells generate electrical energy by electrochemical processes; these devices have higher energy efficiency than typical thermal processes employed to generate electricity, which suffer the limitations of the Carnot's cycle. Generally a fuel cell has a real energy efficiency between 40 and 60% [30,46].

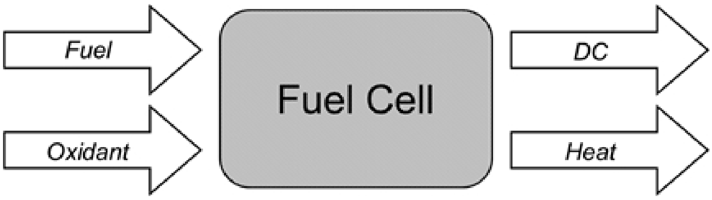

Figure 2.2: Schematic representation of a fuel cell.

Fuel cells consist of three main components: an electrolyte sandwiched between an anodic electrode (negative pole, oxidation site) and a cathodic electrode (positive pole, reduction site). This ensemble constitutes the Membrane Electrode Assembly (MEA), the fuel cell core, involved in the oxido-reductive processes. The electrolyte allows the spatial separation between the anodic and the cathodic compartment, so the chemical reaction between the fuel and the oxidant is split in two half reactions: the fuel oxidation which occurs at the anodic side and the oxidant reduction which occurs at the cathodic side. Fuel oxidation generates electrons which are collected in an external circuit, in order to reach the cathodic electrode where they are involved in the O_2 reduction; the current flow in the external circuit can be exploited to generate an electric work. A contemporaneous flow of ionic species occurs in the electrolyte in order to insure the cell electro-neutrality and to close the circuit. Catalyst are deposited on both the anodic and the cathodic electrode in order to ease and speed up the two half reactions, and so to increase fuel cell performances. Noble metals are the most active catalysts for fuel cells; platinum is the most employed one. Generally the catalysts are based on metal nanoparticles dispersed on high conductive supports; nanosizing the catalyst allows to reduce the precious metal loading and to increase the catalyst performances, due to a very high electrochemical active surface area [30,45,46].

There are several types of fuel cells, classified by the working temperature, the electrolyte employed and the power density delivered, which relate to the fuel cell application. An individual H_2/O_2 fuel cell has a relative small electrical potential, from 0.7 up to 1.0 V, so single cells are placed in series, stacks, in order to reach the voltage required for certain applications [47]. A short overview of the main fuel cells types is reported in table 2.1 [48–51].

Table 2.1: Fuel cells classification by working temperature, application and electrolyte.

	Polymer Elecrtolyte Membrane Fuel Cells (PEMFCs)	**Phosphoric Acid Fuel Cells (PAFCs)**	**Alkaline Fuel Cells (AFCs)**	**Molten Carbonate Fuel Cells (MCFCs)**	**Solid Oxide Fuel Cells (SOFCs)**
Electrolyte	proton exchange membrane (Nafion^{TM})	H_3PO_4 adsorbed on a SiC matrix	concentrated KOH solution	Li_2CO_3 or Na_2CO_3 or K_2CO_3 on ceramic matrix	Zr and Y oxides based ceramics
Ions exchanged	H^+	H^+	OH^-	CO_3^{2-}	O^{2-}
Working temperature	25-100°C	160-220°C	60-220°C	600-650°C	1000°C
Fuel	hydrogen, alcohols, short chain hydrocarbons	hydrogen, short chain hydrocarbons	hydrogen	hydrogen, short chain hydrocarbons	hydrogen, hydrocarbons
Catalysts	platinum based	platinum based	platinum based, platinum free	platinum based, platinum free	platinum based, platinum free
Applications	household, automotive, portable power supply	stationary high power density supply	automotive, aerospace industry	stationary high power density supply	stationary high power density supply

2.2.1. H_2/O_2 Polymer electrolyte membrane fuel cells, the state of the art

The hydrogen/oxygen (air) fed PEMFC (Polymer Electrolyte Membrane Fuel Cell) is the most diffused low temperature fuel cell (figure 2.3). The electrolyte is composed of a polymeric backbone grafted with ionic functional groups that confer ionic conductivity. The membrane must have low permeability of the reactants, in order to reduce the cross over phenomenon, high ionic conductivity, and high chemical, mechanical and thermal stability. The DuPont Nafion^{TM} membrane is the state of the art of PEMs; it is composed of a PTFE backbone grafted with perfluorosulfonic groups, which favor H^+ conduction [46]. Nanostructured platinum is the most diffused anodic and cathodic electrocatalyst, due to its high efficiency in both the Hydrogen Oxidation Reaction (HOR) and in the Oxygen Reduction Reaction (ORR), which happen at the anodic and the cathodic cell compartments respectively [45,46].

A short description on how a PEMFC works now follows. The fuel, hydrogen gas, is delivered to the anodic electrode by diffusion channels with a specific flow rate in order to avoid fuel depletion at the electrode that leads to a drop cell activity. Hydrogen penetrates into the catalyst pores and reacts on the catalyst surface as described in reaction eq. 2.2. The protons migrate to the cathode through the membrane, while the electrons reach the cathodic electrocatalyst passing through the external circuit. Protons and electrons are involved in the oxygen reduction reaction on the cathodic catalyst surface (eq. 2.3); the ORR is the limiting process in the PEMFC efficiency, hence the cathodic electrocatalyst has quite a high platinum loading (0.3 mg_{Pt} cm^{-2}) in order to speed up the oxygen reduction reaction. The polymeric ion exchange membrane must be wet to allow H^+ ions migration from the anode to the cathode; proton migration is coupled with water migration from the anode to the cathode. This H_2O flux, the electro-osmotic drag, dries the membrane, reducing the ionic conductivity in the electrolyte with a consequent fuel cell activity drop. In order to avoid electrolyte dehydration, the fuel and the oxidant must be humidified before their inlet in the cell. The distribution channels deliver H_2 and O_2 to the anode and to the cathode, in addition the channels allow to remove the fuel and the unreacted oxidant and other reaction products [30,46,52].

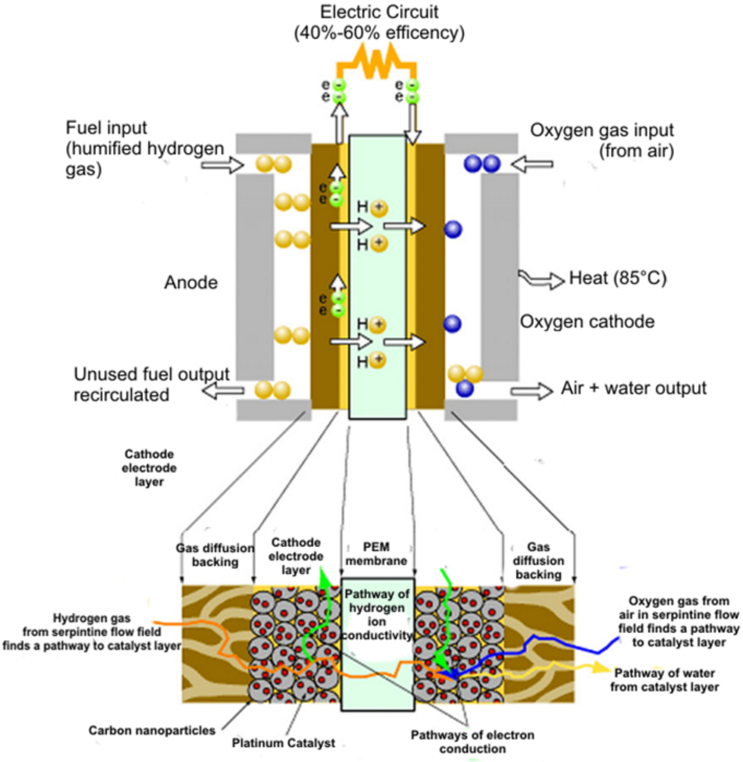

Figure 2.3: schematic representation of a hydrogen/oxygen fed PEMFC.

Anode $$H_2 \rightarrow 2H^+ + 2e^- \quad (E_a^0 = 0.0V)$$ *Eq. 2.2*

Cathode $$\frac{1}{2}\, O_2 + 2H^+ + 2e^- \rightarrow H_2O \quad (E_c^0 = 1.23V)$$ *Eq. 2.3*

Cell $$\frac{1}{2} O_2 + H_2 \rightarrow H_2O \qquad (E_{cell}^0 = E_c^0 - E_a^0 = 1.23V)$$ *Eq. 2.4*

H_2/O_2 fed PEMFC stacks can deliver power of up to 250 kW. This kind of fuel cells has a huge potential in the automotive field and in portable power supply applications. The use of the hydrogen as fuel has several logistical problems, like a safe distribution system. The true “bottle-neck” that limits the diffusion of H_2/O_2 PEMFCs is the use of platinum based electrocatalysts: platinum, in fact, has a low natural abundance and a high cost [3]. In addition, PEMFCs suffer from corrosion related problems due to the acidic environment of the membrane [30].

2.2.2. Direct alcohol fuel cells, the state of the art

A Direct Alcohol Fuel Cell (DAFC) is a PEMFC fed with an aqueous solution of an alcohol, generally methanol (Direct Methanol Fuel Cells, DMFCs) [3,48]. Methanol is oxidized on the anodic side, releasing electrons and protons that flow to the cathode passing respectively through the external circuit and the proton exchange membrane; at the cathode, they are involved in the oxygen reduction reaction (figure 2.4, eq. 2.5, eq. 2.6, eq. 2.7).

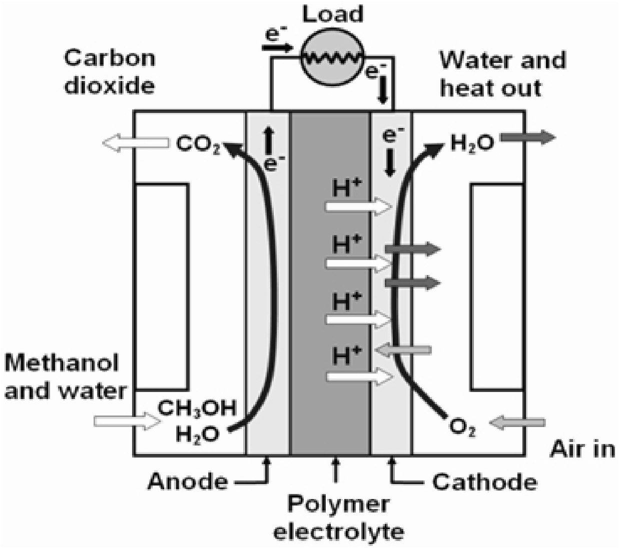

Figure 2.4: schematic representation of a direct methanol fuel cell.

Anode $CH_3OH + H_2O \rightarrow 6H^+ + CO_2 + 6e^- \quad (E_a^0 = 0.046)$ *Eq. 2.5*

Cathode ${}^{1}/_{2}\ O_2 + 2H^+ + 2e^- \rightarrow H_2O \quad (E_c^0 = 1.230V)$ *Eq. 2.6*

Cell ${}^{3}/_{2}\,O_2 + CH_3OH \rightarrow CO_2 + 2H_2O \quad \left(E_{cell}^0 = E_c^0 - E_a^0 = 1.180V\right)$ *Eq. 2.7*

Methanol has some interesting features, like a high energy density (6.1 kWh kg^{-1}) and the easiness of storage and handling due to its liquid nature, that make DMFCs very interesting devices for energy supply to portable devices [3]. Unfortunately, there are several drawbacks that limit the development of DMFC technology; in particular, methanol has a high toxicity, a high flammability and a high vapor pressure [53–55]. In addition DMFCs suffer from high cross-over phenomenon: the alcohol permeates through the PEM membrane reaching the cathodic side where it is oxidized by the cathodic catalyst, lowering the cell potential, and hence the fuel cell efficiency. DMFCs like PEMFCs also suffer from problems of corrosion due to the acidic membrane [53,54].

Over the last decade research has focused on the replacement of methanol with heavier alcohols, like ethanol, ethylene glycol, 1,2-propanediol and glycerol. These alcohols, in fact, have a lower toxicity, flammability and vapor pressure; in addition they have a higher energy density (8 kWh kg^{-1} for ethanol) than methanol and they can be obtained from first and second generation biomass, with an EROEI ratio of up to 40 [53,54,56–58]. Unfortunately to date the sluggish oxidation kinetics of these alternative alcohols strongly limit their employment in DAFCs that operate under acidic conditions [59].

At the current state of the art, both anodic and cathodic electrocatalysts are based on platinum alloys (Pt, PtSn and PtRu). There are a number of problems related to using these catalysts which limit DMFC performance [53–55]:

- Slow methanol oxidation kinetics that generally are compensated with a high platinum loading in the catalyst.
- Catalyst poisoning by MeOH oxidation intermediate species, like CO.
- Platinum is an expensive material and it has a low natural abundance.

2.3. Anion exchange membrane, a new perspective for H_2/O_2 PEMFC and DAFCs

Platinum-based electrocatalysts are the main limiting factor hindering the large scale development of proton exchange membrane fuel cells, due to the high cost of this metal and to the high Pt loading necessary to speed up the sluggish ORR reaction in H_2/O_2 PEMFCs and the sluggish methanol oxidation reaction in DMFCs. Another limiting factor of platinum based catalysts is the CO poisoning effect. Unfortunately, Pt and its alloys are the best catalytic materials for the hydrogen and alcohol oxidation reactions and for the oxygen reduction reaction performed in acidic environments. Platinum is also the only metal that can tolerate the strong acidic environment of proton exchange membranes [60–62].

Operating in an alkaline environment is the only way to overcome these issues as in principle non platinum electrocatalysts, even non noble based electrocatalysts, can be used and the reactions kinetics are generally faster with respect to acidic conditions. Alkaline conditions are also much less corrosive for FCs components [60,62–64]. The main drawback of traditional Alkaline Fuel Cells is the liquid electrolyte, a highly concentrated KOH aqueous solution, that suffers from drying and flooding effects and of poisoning due to absorption of atmospheric CO_2 [60,62].

The development of anion (OH^-) exchange membranes (AEM) can overcome such limiting factors, making these cells an interesting field of study, in particular for the development of innovative platinum free and non-noble metal based electrocatalysts [60]. In the literature there are several examples of anion exchange membranes; in this work the Tokuyama Corporation A-201® membrane will be employed.

The Tokuyama AEM is composed of a polyethylene backbone functionalized with quaternary ammonium groups that allow OH^- ion conduction (figure 2.5) [65]. Various physical properties of two membranes Tokuyama A-201® and A-901 are described in table 2.2. The solubilized form of this membrane, the Tokuyama AS-4® ionomer can be employed as ionomer and catalyst binder in electrodes for testing catalysts in fuel cells.

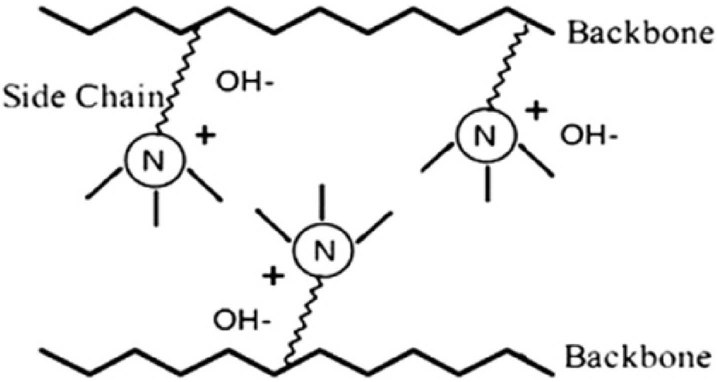

Figure 2.5: Schematic representation of a Tokuyama membrane, OH^- type.

Table 2.2: Main features of the two main Tokuyama anion exchange membranes.

	A 201	**A 901**
Counter ion	OH^-	OH^-
Tickness (µm)	28	11
Ion exchange capacity (mmol g^{-1})	1.7	1.6
Water %	19	19
Resistance (Ω cm^{-2})	0.3	0.2

Regarding the cathodic catalyst, in alkaline environment platinum can be easily replaced by a wide choice of non-noble metals [66–68]; for example transition metal phthalocyanines, [69,70] heat treated (600-1000 °C) carbon supported iron and silver or cobalt phthalocyanines [71,72] and nitrogen doped carbon materials that may or may not contain transition metals [73,74].

The main challenge of the alkaline environment is the development of high efficiency anodic electrocatayst.

The main challenge of working with alkaline membranes is the development of highly efficient anodic electrocatalysts [61,75–78]. In stark contrast to PEMFCs, the kinetics of the HOR reaction is quite slow under alkaline conditions even when Pt is used. Indeed, the HOR activity on carbon supported noble metals (Pt, Pd and Ir) decreases by circa 100*X* when switching from low to high pH [79]. This factor has been the main obstacle preventing the realization of a Pt free AEM-FC with useful power output (figure 2.6-A). Since Lu and co-workers first presented a noble metal free AEM-FC in 2008 (H_2/O_2, Tcell 60 °C, maximum power density 50 mW cm^{-2}) [80], little progress has been made primarily due to the challenge of overcoming poor HOR kinetics in AEM-FCs [61,75–78].

The development of alkaline DAFCs (figure 2.6-B) has been the subject of much research over the last decade. In fact, these devices have several advantages with respect to traditional DMFCs operating with acidic membranes; first of all alcohols oxidation reactions are faster in alkaline environments. In addition, alcohol cross-over through the membrane is strongly limited by the electro-osmotic migration of the OH^- ions in the electrolyte, which happens in the opposite way with respect to the alcohol flux from the anodic to the cathodic compartment [53,55,58,75–78,81,82].

The use of non-noble metal based cathodic electrocataysts, which are inactive for alcohol oxidation, removes any negative effect from fuel crossover. Heat treated carbon supported iron and cobalt phthalocyanines are the most common examples of cathodic electrocatalysts employed in DAFCs [71,72].

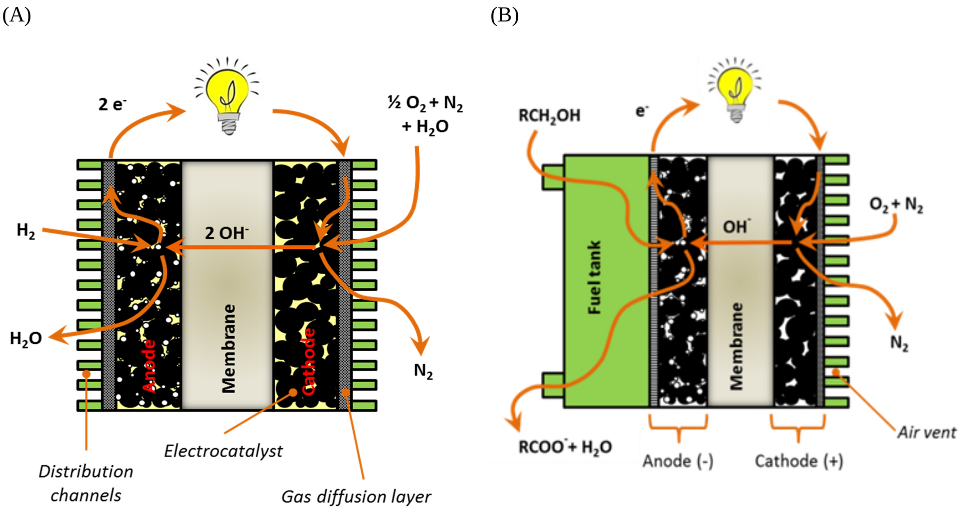

Figure 2.6: Schematic representation of (A) H_2/O_2 fed AFC and (B) DAFC.

Nanostructured Pd based electrocatalysts represent the state of the art of DAFCs anodic electrocatalysts. Palladium has a higher natural abundance than platinum and consequently a lower commercial price [53]. In strong alkaline environments ($pH \geq 13$), palladium is not able to cleavage the C-C bond of alcohols like ethanol, and this makes alcohol oxidation reactions strongly selective to the corresponding carboxylic compounds [53,54,58,81,82]. At lower pHs, Pd based electrocatalysts can partially cleave the C-C bond [3]. At first sight, this strong selectivity for partially oxidized products limits the faradic efficiency of the oxidation reaction, but the very fast oxidation kinetics compensate this limitation. In addition, alcohol oxidation to carboxylic compounds do not pass through the CO reaction intermediate that have strong poisoning effects on such catalysts [53].

The partial oxidation of ethanol to acetate in DAFCs (eq. 2.8, eq. 2.9 and eq. 2.10) makes these devices a potential “biorefinery”, in addition to a power source. In fact acetate, is a very important raw chemical for the fine chemical and pharmaceutical industry [83]. The high added value of acetate is an economic way to compensate for the low faradic yield of ethanol oxidation on Pd based anodic catalysts. At present, the Monsanto® and Cativa® industrial processes of methanol carbonylation are the most convenient ways to synthetize acetic acid. These processes require high temperatures and Ir and Rh organometallic compounds as homogeneous catalysts [84,85], while in DAFCs acetate is produced at low temperature (25-100°C) and atmospheric pressure.

Anode $CH_3CH_2OH + \ 5OH^- \rightarrow CH_3COO^- + 4H_2O + 4e^- \quad (E_a^0 = -0.743V)$ *Eq. 2.8*

Cathode $O_2 + 4e^- + 2H_2O \ \rightarrow 4OH^- \quad (E_c^0 = 0.401V)$ *Eq. 2.9*

Cell $CH_3CH_2OH + \ O_2 + OH^- \ \rightarrow \ CH_3COO^- + 2H_2O \qquad (E_{cell}^0 = \ 1.144V)$ *Eq. 2.10*

Until now, alkaline DAFCs are able to oxidize selectively ethanol to acetate (up to 100% selectivity). Unfortunately these device fail in the selective oxidation of other interesting renewable alcohols like ethylene glycol, glycerol and 1,2-propanediol [83,86]. The main challenge of the research then is to develop a catalyst that can selectively oxidize these alcohols to their respective carboxylic compounds, in order to set up a device that does not require costly product purification processes. Figure 2.7 describes the main products of the oxidation of various renewable alcohols under strong alkaline conditions on Pd based electrocatalysts.

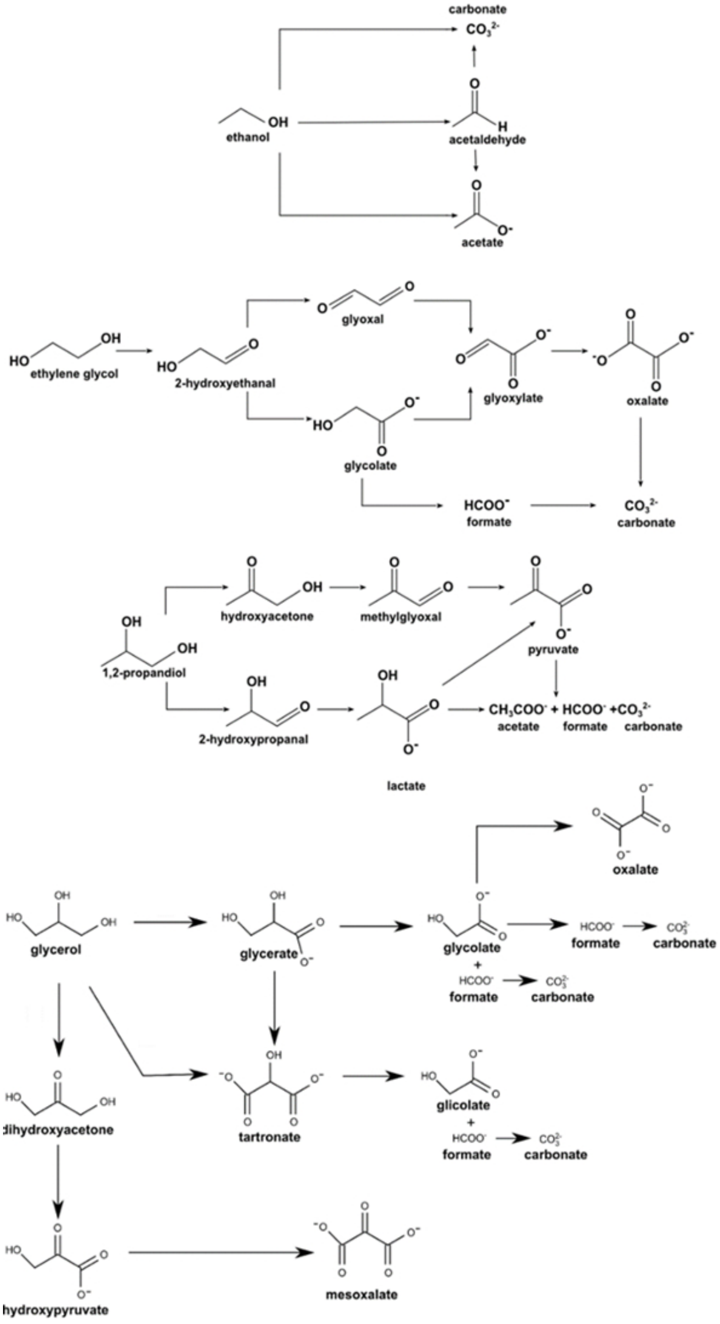

Figure 2.7: Main electro-oxidation products of ethanol, ethylene glycol, 1,2-propanediol and glycerol when the reactions are performed on palladium based electroctalysts in alkaline environment [3].

2.4. Electrolysis

Electrolyzers are electrochemical devices that convert electrical energy in chemical energy, splitting water into molecular hydrogen and oxygen (figure 2.8) [3,87,88]. An electric generator applies a DC current between the anode and the cathode, in order to force the non-spontaneous reactions of Oxygen Evolution Reaction (OER) at the anodic side and the Hydrogen Evolution Reaction (HER) at the cathodic side. The water solution must be conductive to maintain the electroneutrality of the system [28,87,88].

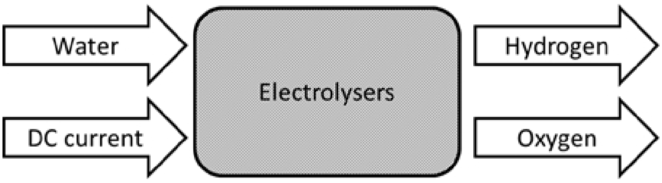

Figure 2.8: Schematic representation of an electrolyzer

Electrolysis is a well-established technique for the production of pure hydrogen (99.999% assay) and the main application is in laboratories for in-situ hydrogen production [3,89]. Electrolysis has a particular appeal when used in the “hydrogen economy” system because the electricity obtained from renewable sources can be stored by synthesizing molecular hydrogen. At the state of the art there are five main typologies of electrolyzers, classified by the type of electrolyte employed [87,88,90,91]:

- Acid electrolyzers. The electrolyte is an aqueous acidic solution.
- Alkaline Electrolyzers (AE). The electrolyte is an aqueous KOH (25-35 wt.%) solution, and the device working temperature is 80°C.

- Proton Exchange Membrane Electrolyzers (PEME). The electrolyte is a cation exchange polymeric membrane sandwiched between the anode and the cathode that is fed by pure water.
- Zero Gap Electrolyzers (ZGE). This device is an alkaline electrolyzer in a particular configuration that avoids the use of the separator between the anodic and the cathodic compartment.
- Solid Oxide Electrolyzer Cells (SOEC). The electrolyte is a ceramic membrane based on yttria and zirconia oxides sandwiched between the anode and the cathode. SOECs are the only devices that work at high temperature (500-1000°C).

2.4.1. Proton exchange membrane electrolyzers, the state of the art

Proton electrolyte membrane electrolyzers (PEME) are the best low temperature (< 100°C) devices for hydrogen production from water electrolysis because they have low ohmic drops respect the traditional alkaline electrolyzers, so they can operate at high current densities ($J > 1\ A\ cm^{-2}$) that allow a high hydrogen production rate. At the state of the art, platinum is the most diffused catalytic material for the cathodic side of the cell, while the high potentials and the low pH values at the anode requires catalytic materials based on Ir, Ta and Ru oxides mixtures [27].

A short description of how a proton electrolyte membrane electrolyzers works is now reported (figure 2.9).

The DC load applied to the electrodes polarizes the anode, in order to force the oxygen evolution reaction that generates gaseous oxygen, electrons and H^+ ions (eq. 2.11). Protons migrate through the membrane reaching the cathode, where they recombine with the electrons provided from the DC load to obtain hydrogen (eq. 2.12). The membrane has both the role of electrolyte that allow the H^+ ions migration and of gas separator, in order to avoid an hydrogen and oxygen explosive mixture inside the cell [92,93].

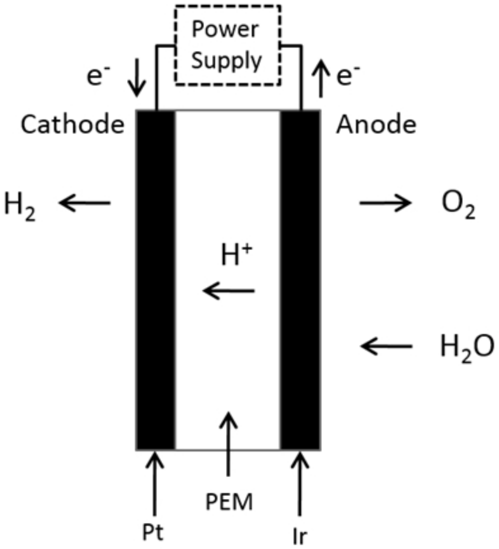

Figure 2.9: Schematic representation of the proton exchange membrane electrolyzer.

Anode $2H_2O \rightarrow 4H^+ + O_2 + 4e^- \quad (E_a^0 = 1.23V)$ *Eq. 2.11*

Cathode $4H^+ + 4e^- \rightarrow 2H_2 \;\; (E_c^0 = 0.00V)$ *Eq. 2.12*

Cell $2H_2O \; \rightarrow \; 2H_2 + O_2 \qquad (E_{cell}^0 = \; 1.23V)$ *Eq. 2.13*

The thermodynamic potential E° for water splitting in hydrogen and oxygen in acidic environment is 1.23V, but the iR drops of the system and the activation overpotentials of the anodic and cathodic half reactions impose to work with a higher working potential. The optimal working potential applied to the elctrolyzer is about 2V, in oreder to have quite fast anodic and cathodic half reactions for a quantitative gases evolution with low energy consumption. The best PEME has an energy consumption of 50-55 kWh per kg of hydrogen produced. The high energy consumption of this class of electrolyzers is the main limiting factor for their massive development [27,93,94]. In addition, the Department of Energy of the USA (DOE) stated that by the 2020 the hydrogen production by electrolytic processes must have an energy consumption lower than 43 kWh $kg_{H_2}^{-1}$, keeping constant the hydrogen production rate [27].

2.4.2. Anion exchange membrane alcohol electroreformers

Oxygen evolution is thermodynamically a costly reaction and hence the OER is largely responsible for the high working potential and the high-energy consumption of electrolyzers. The thermodynamic contribution of the OER alone requires an energy of 33.6 kWh for each kilogram of hydrogen produced. In addition sluggish electrode kinetics increase the energy consumption up to 50 kWh $kg_{H_2}^{-1}$ [3]. Replacing the OER with an easier reaction is one way to lower the energy cost of hydrogen production through electrolysis [3]. Recently Botte et al. replaced the OER at the anode with the oxidation of ammonia to nitrogen. This lowers the thermodynamic electrolyzer potential to 0.06V, saving about the 30% of the energy employed in a conventional device [95,96]. The high amount of Pt and Ir in the anodic electrocatalyst, the catalyst poisoning by nitrogen intermediates and the high energy cost of ammonia synthesis have limited the development of this technology [3].

The oxidation of an alcohol under alkaline conditions is a more suitable reaction to replace the OER (eq. 2.14) [27,92,97,98]. Alkaline alcohol electroreformers (AER) are the best devices for this purpose (figure 2.10) because they use the same technology used for alkaline DAFCs, the only difference is that a DC current load is now applied between the two electrodes, in order to force the cathodic hydrogen evolution reaction (eq. 2.15) [27,89]. In a recent example of an alkaline alcohol PEME (or alkaline alcohol electroreformer), an energy consumption for the device of 26 kWh $kg_{H_2}^{-1}$ was determined that corresponds to an energy saving about the 60% with respect to a traditional water electrolyzer [27].

Alkaline alcohol electroreformers are safer devices with respect to traditional water electrolyzers because no oxygen is produced at the anode. The absence of any potential explosive mixture of H_2/O_2 inside the reformer makes it, at least in theory, possible to compress the hydrogen produced at high pressures [3].

The alcohol reformer hardware is the same as DAFCs, with the only difference being that a DC load is applied to the electrodes, in order to force at the cathode the not spontaneous water reduction to hydrogen and OH^- anions (eq. 2.15). The OH^- species migrate through the membrane from the cathodic compartment to the anodic one, where they are involved in the alcohol oxidation reaction (eq. 2.14). This ionic flow maintains device electro-neutrality (figure 2.10). The cathodic compartment is solution free, because sufficient water permeates through the membrane feeding the HER at the cathode. This “dry” nature of the cathodic compartment improves the efficiency by reducing ohmic losses through bubble formation [99].

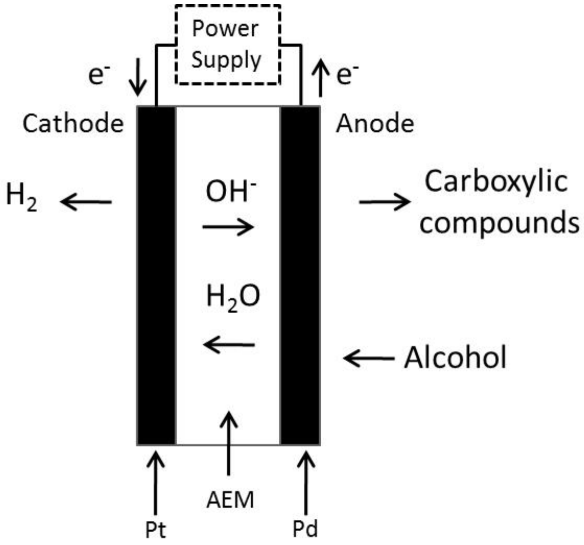

Figure 2.10 :Schematic representation of an alkaline alcohol electroreformer fed at the anodic side with an aqueous KOH and alcohol solution [99] .

Anode $$CH_3CH_2OH + 5OH^- \rightarrow CH_3COO^- + 4H_2O + 4e^- \quad (E_a^0 = -0.743V)$$ *Eq. 2.14*

Cathode $$4H_2O + 4e^- \rightarrow 2H_2 + 4OH^- \quad (E_c^0 = -0.83V)$$ *Eq. 2.15*

Cell $$CH_3CH_2OH + OH^- \rightarrow CH_3COO^- + 2H_2 \quad (E_{cell}^0 = 0.11V)$$ *Eq. 2.16*

Palladium is the best material to be employed as anodic electrocatalyst for the following reasons [3,27,89]:

- Under strongly alkaline conditions (pH ≥ 13), palladium is not able to effect complete oxidation to CO_2, so alcohols are generally partially oxidized to respective carboxylic compounds. Such chemicals have added value because they are raw materials used in the fine chemical industry, therefore alcohol PEMEs, like

DAFCs, are possible “biorefineries” that allow to extract energy and valuable chemicals from a renewable source, working at low temperature and atmospheric pressure [3].

- The fast oxidation kinetics of the alcohols compensate the low faradic yield of the oxidative process.
- Renewable alcohols like ethanol, ethylene glycol, 1,2-propanediol and glycerol can be employed as fuels.
- Standard non noble metal cathodic electrocatalysts can be easily employed [94].

2.5. Electrocatalysts

Electrocatalysts consist of an electroactive phase (generally nanostructured metals) dispersed on a conductive support material (figure 2.11) [51].

The active phase is the electrocatalytic material where oxidation and reduction reactions happen; the electroactive material promotes the kinetics of the electrochemical reactions, reducing the cell voltage drop due to the activation polarization phenomenon [3]. Nanostructuring of the catalytic material increases the Electrochemical Active Surface Area (EASA) of the catalyst. In addition, the nanosizing process reduces the noble metal amount employed in the catalyst, reducing the costs of the electrochemical devices in which they are employed [3]. Replacing the nanostructured active phase with an organometallic compound increases dramatically the catalyst electroactive area, because each metal site is active in the reaction. In addition, the complex structure can be tuned to influence directly the catalyst activity and the reaction selectivity.

In all cases the complex must be air stable and soluble in different solvents to allow its deposition on conductive supports [86,100].

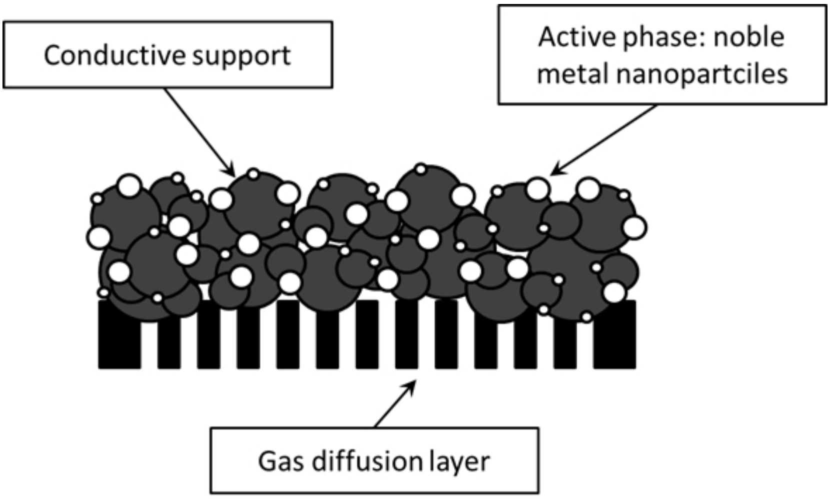

Figure 2.11: Schematic representation of the electrocatalyst.

The conductive support material must have a high surface area and usually has dual scale porosity: the nanoscale porosity helps to increase the catalyst dispersion, while pores bigger than 100 nm ease the mass transport of the reactants and the products into the catalyst active phase. The support material must be chemically inert and stable to corrosive environments (both acidic and alkaline); in addition it must have a high electronic conductivity to drive the electrons involved in the reactions to the current collector plates. Carbon black, like Vulcan XC-72 or Ketjen Black EC 600 JD, is the most diffused carbon support; new types of high performance carbon supports can be employed, like single walled and multi walled carbon nanotubes (SW/MW-CNTs), graphene and non-carbon supports like titania nanotubes arrays (TNTAs). These supports have high chemical resistance, high electron conductivity and high porosity [3,53,59,101].

In fuel cells fed with H_2 and O_2, the catalyst is mixed with an ionomer that has the function of increasing the ionic conductivity in the catalyst layer, reducing the catalyst layer resistance. The ionomer is usually a solubilized ion exchange polymer that can be deposited with the catalyst particles to form the electrode. On the contrary, fuel cells and electrolysers fed by liquid fuels with dissolved electrolyte (e.g. KOH or NaOH) do not employ ionomers in the catalytic material because the fuel solution guarantees the ionic conductivity inside the catalyst layer. In this case another polymer, the binder, is added to the catalyst to hold together all the catalyst components and ensure the catalyst mechanical stability; PTFE is the most employed binder [3,51].

In anodic and cathodic electrocatalysts fed by a gaseous reactant, the catalytic material is deposited on to a conductive chemically inert support to obtain an electrode that can be sandwiched in the MEA. This support, the Gas Diffusion Layer (GDL), have also the role of distributing homogeneously the reactants to the catalyst layer and of preventing catalyst flooding removing the water and heat excess. GDLs are carbon based fiber materials, like Carbon Paper (CP) and Carbon Cloth (CC) [51]. Alternative supports can be used especially with liquid fed cells for example nickel foam, titanium and nickel mesh [3].

3. Organometallic Fuel Cells

3.1. Introduction

Direct alcohol fuel cells (DAFCs) have a crucial role to play in sustainable chemistry because they convert a renewable source, an alcohol, into electrical energy and chemicals, like aldehydes, ketones, and carboxylic acids. The simultaneous production of energy and industrially relevant feedstocks allows the complete exploitation of the resource, without the generation of byproducts. The more the oxidation of the alcohol is selective for a particular product, the more the process is efficient [57,86,102].

The anodic electrocatalyst is the main component responsible for promoting the selective oxidation of alcohols to carboxylic compounds [82]. Traditional palladium based anodic electrocatalysts are extremely efficient for the selective oxidation of ethanol but they fail in the selective oxidation of renewable polyols and sugars [86].

Recently, Vizza and coworkers introduced a breakthrough in the concept of anodic electrocatalysts for alkaline DAFCs, switching from traditional nanostructured catalysts to a molecular based one. In principle, a metal complex offers enormous advantages in the rational design and optimization of anode electrocatalysts. A significantly reduced metal loading on the electrode is expected because all metal sites are active, unlike catalysts based on metal nanoparticles [57,86]. The first example of a molecular anodic electrocatalyst employs the $Rh[(trop_2NH)PPh_3]OTf$ (figure 3.1; $trop_2N$ = bis(5-H-dibenzo[a,d]cyclohepten-5-yl)-amide) organometallic compound supported on carbon black (Vulcan XC-72, Cabot Corp.). This innovative fuel cell was called OrganoMetallic Fuel Cell (OMFC) and showed a 100% selectivity in ethanol oxidation to acetate, providing a maximum power density of 25 mW cm^{-2} at 60°C [57]. After this example, other groups have realized working OMFCs fed with sugars [103] or alcohols [104,105]. Rh[(trop$_2$NH)PPh$_3$]OTf is still the most performing organometallic electrocatalyst and the use of a high surface area (1400 m^{2}g^{-1}) carbon support Ketjenblack EC 600JD (KtjBk) instead of the Vulcan XC-72 increases the complexes electro-oxidative performances. In fact, KtjBk allows to high dispersion of the complex crystallites, increasing the number of catalyst active sites and reducing catalyst poisoning effects [102].

In this chapter, the Rh[(trop$_2$NH)PPh$_3$]OTf/KtjBk (**1@C** in figure 3.9) anodic activity in OMFCs for renewable polyalcohol oxidation will be investigated; the fuel cells cathodic side is equipped with a proprietary FeCo/C catalyst [71] and the electrolyte used is a Tokuyama® A-201 anion exchange membrane. The attention will be focused on ethylene glycol and on longer aliphatic chain alcohols like 1,2-propanediol. In order to understand the oxidation mechanisms of the complex based anode, the diols series was completed by 1,3-propanediol and by the 4 carbon aliphatic chain alcohol 1,4-butanediol. The Rh[(trop$_2$NH)PPh$_3$]OTf based OMFC successfully oxidizes the renewable polyols ethylene glycol and 1,2-propanediol to potassium glycolate and lactate with a 100% selectivity. These products are high value raw chemicals for the fine chemical industry. Finally, the OMFC has been shown to have the best activity ever reported among organometallic fuel cells, with a power density delivered of more than 40 mW cm^{-2} at 80°C with 1,4-butanediol as fuel.

3.1.1. The choice of the complex

The complex Rh[(trop$_2$NH)PPh$_3$]OTf (MW: 911.78 g/mol, figure 3.1) has been successfully employed by Prof. Grützmacher’s research group (ETH-Zürich) for the oxidation of methanol and low aliphatic alcohols in in the presence of hydrogen acceptors and palladium nanoparticles [106,107]. After this experience, Vizza’s research group supported the complex on Vulcan XC-72 and realized the anode for the first OMFC fed with ethanol [57].

Rh[(trop$_2$NH)PPh$_3$]OTf structure strongly deviates from the expected planar form of a tetra-coordinated ML_4 complex (M = d^8 metal center, L = 2 electron donor ligand) with a 16 valence electron configuration. Instead, a saw-horse-type structure is created by the combination of two π-acceptor olefinic binding sites, and an amido and phosphane σ-donor groups, each placed in a trans-position (figure 3.1) [106,107]. As a result, the amido function is Lewis basic (the highest occupied orbital (HOMO) is localized on the N center) and the adjacent rhodium center is Lewis acidic (the lowest unoccupied orbital (LUMO) is localized on the metal center). The PPh$_3$ ligand and the unique geometry of the trop ligand confers a high stability to the Rh-complex: it is air stable as a solid or supported and it does not decompose at temperatures below 100 °C [106,107].

Rh[(trop$_2$NH)PPh$_3$]OTf is easily soluble in organic polar solvents, like acetone and THF, this allows the deposition of this molecule on several supports by the impregnation method. On the other hand, this complex is insoluble in water and small alcohols, the main components of the fuels for DAFCs [57,86].

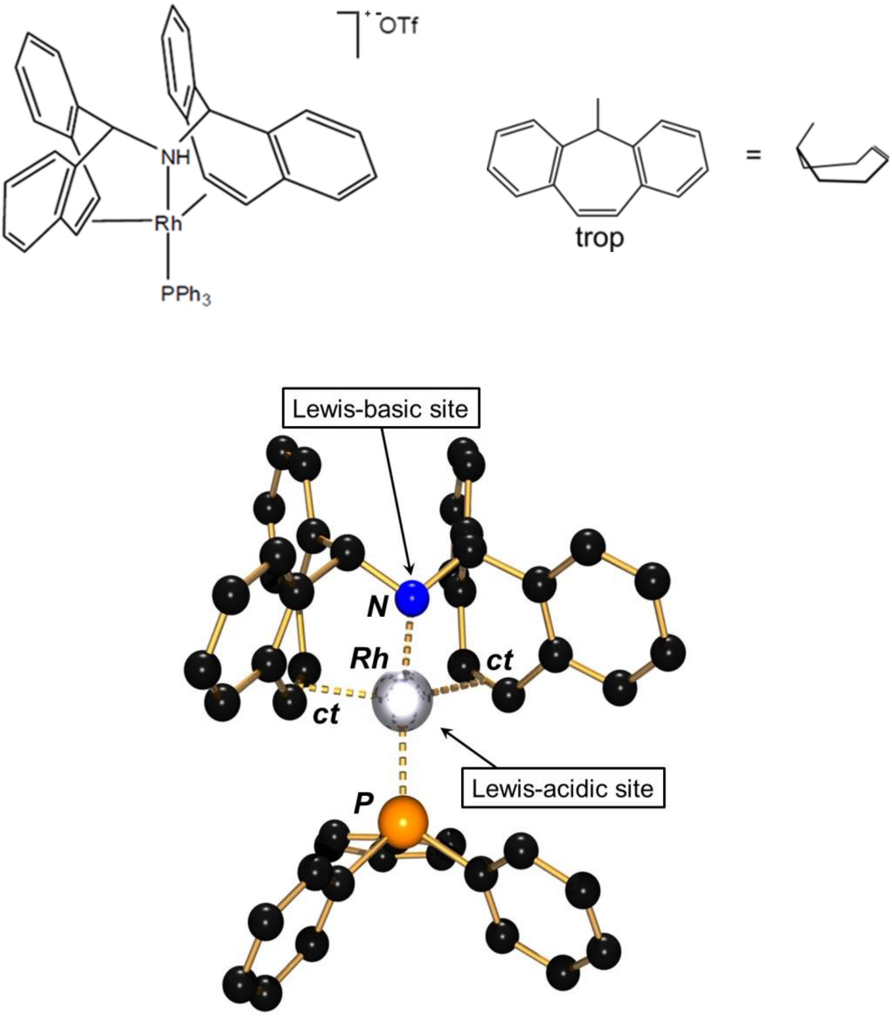

Figure 3.1: The Rh[(trop$_2$NH)PPh$_3$]OTf complex.

3.2. Synthesis

The synthesis of the catalyst consist in two main steps: the synthesis of the Rh complex and its deposition onto carbon black by an impregnation method, in order to obtain a catalytic powder that can be then deposited onto a conductive support to obtain an electrode for fuel cells.

All of the synthesis was performed under argon atmosphere with standard Shlenk-vacuum glassware. All the glassware was dried at 120°C overnight before the use. All the solvents were used as purchased (Sigma-Aldrich, ACS purity grade) and were deoxygenated by bubbling argon for one hour. The reaction products were controlled by ^{1}H, ^{13}C and ^{31}P-NMR spectroscopy.

3.2.1. Synthesis of the Rh[(trop$_2$NH)PPh$_3$]OTf complex

The synthesis of the complex was performed by Prof. Grütmacher's group in the Laboratory of Inorganic Chemistry of the ETH of Zürich. Here, the synthetic procedure is not reported because now belongs to the state of the art: it is completely described in [108–110].

3.2.2. Rh[(trop$_2$NH)PPh$_3$]OTf impregnation on KtjBK

The Catalyst deposition onto Ketjen Black EC-600 JD (Akzo Nobel Corp.) was performed as reported in the literature (figure 3.2) [57,102]; all the steps were performed at room temperature under argon atmosphere:

- In a 100 mL Shlenk tube, 650 mg of the complex (0.667 mmol) was dissolved in 50 mL of deareated acetone.

- The solution was added drop wise (one drop per second ca.) to a vigorously stirring suspension of KtjBk (1.160 g) in 72 mL of acetone.
- The solution was then stirred for 2 hours, in order to deeply impregnate the complex into the carbon support.
- The solvent was then completely removed under argon flow to obtain the catalyst in a solid power form. The drying process was performed as slow as possible, keeping the solution under stirring, in order to obtain a good complex dispersion into the carbon black.
- The powder was washed three times with aqueous ethanol (5 wt.%) and then the solid material was dried under reduced pressure.
- A small part of the catalyst was suspended in deuterated THF (THF-d_8) to extract the complex into the solvent and check with ^{31}P-NMR the organometallic compound integrity: the spectrum shows only the doublet peak due to the Rh-PPh_3 coupling (δ 40.6 ppm, J 137.7 Hz). No other signals are visible.

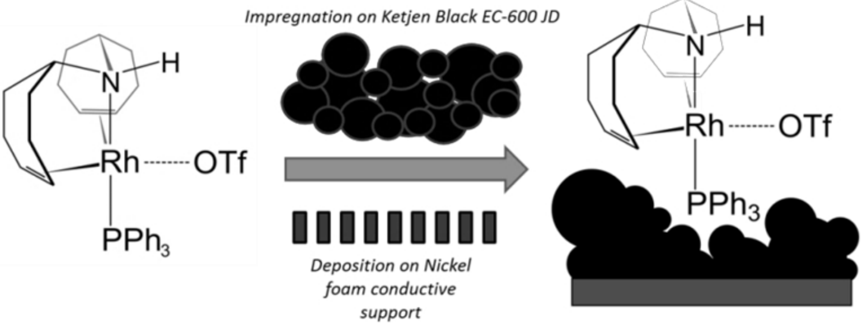

Figure 3.2: Schematic representation of the Rh-complex impregnation procedure.

3.3. Electrochemical characterization

The Rh[(trop$_2$NH)PPh$_3$]OTf complex supported on KtjBk was electrochemically characterized both in half cells and in complete OMFCs fed with 2 M KOH and 2 M ethylene glycol (EG), 1,2-propanediol (1,2-P), 1,3-propanediol (1,3-P) or 1,4-butanediol (1,4-B) aqueous solutions.

3.3.1. Cyclic voltammetry

The electrochemical activity of [Rh(trop$_2$NH)(PPh$_3$)]OTf deposited on Ketjenblack EC 600 JD, **1@C** (figure 3.9), was first investigated by cyclic voltammetry at room temperature in deoxygenated 2 M aqueous KOH containing either 2M EG, 1,2- P, 1,3-P or 1,4-B at a scan rate of 50 mVs^{-1} (vs. RHE). The experimental procedure is reported in chapter 7, paragraph 7.6. As expected, the CV response of **1@C** in a 2M KOH solution did not show any electrochemical activity up to the oxygen discharge potential (figure 3.3, trace X, KOH). In contrast, a clear faradic current was observed starting at approximately 0.65 V (vs. RHE) when the electrolyte contained a mixture of a diol and 2M KOH (figure 3.3). The wide potential operating window (up to 1.2 V vs. RHE) shows the inherent stability of the anode electrocatalyst at high potentials. The specific activity (Sa mA μg_{Rh}^{-1} in figure 3.3), increases with increasing the chain length of the diol. A similar trend was observed by Lamy et al. for the electrooxidation of polyalcohols in half cells on polycrystalline Pt and Au electrodes in alkaline media [111]. Table 3.1 summarize the catalyst electrochemical performance: the complex has the best activity for

1,4-butanediol electrooxidation, performance both in terms of specific activity, Sa 2.3 mA μg_{Rh}^{-1}, and onset potential, 0.75 V vs RHE.

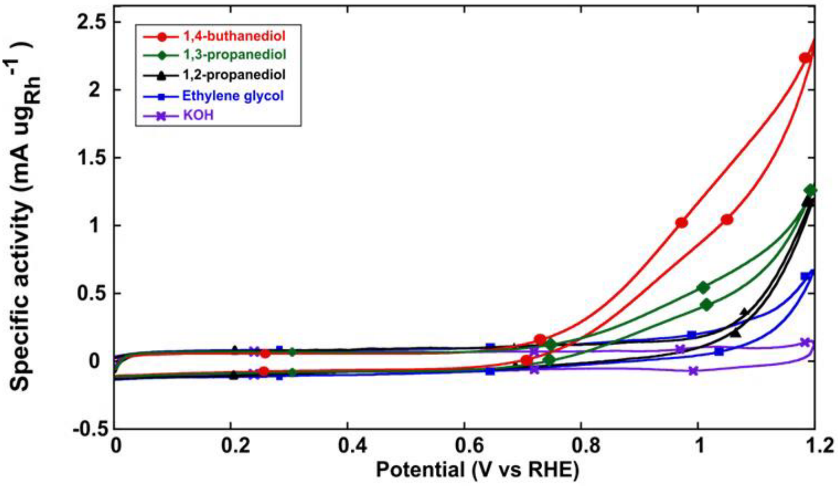

Figure 3.3: CV of the catalyst in (●) 1,4-B; (♦) 1,3-P; (▲) 1,2-P; (■) EG; (X) 2M KOH; aqueous solutions of 2M diols in 2M KOH.

Table 3.1: Rh[(trop$_2$NH)PPh$_3$]OTf/KtjBk electrooxidative activity in half cell measurememnts.

Fuel	**E$_{onset}$ (V vs RHE)**	**Maximum Sa (mA μg^{-1})**
EG	0.95	0.7
1,2-P	0.95	1.4
1,3-P	0.80	2.3
1,4-B	0.75	2.3

3.3.2. OMFCs fed with polyols

The Rh[(trop$_2$NH)PPh$_3$]OTf/KtjBk anode, the FeCo/C cathode and the Tokuyama® A-201 polymeric electrolyte were sandwiched into a Membrane Electrode Assembly (MEA) that was tested both in passive (room temperature) and active (80°C) fuel cells systems. The detailed experimental procedure is described in chapter 7, paragraph 7.7.

The potentiodynamic (●) and power density (○) curves shown in figure 3.4 were obtained with water solutions of 2M EG, 2M 1,2-P, 2M 1,3-P, and 2M 1,4-B in 2M KOH at room temperature (passive cell). The cell containing 1,4-B exhibits the highest peak power density (8.5 mWcm^{-2} at 0.14 V) compared to the other diols (figure 3.4-a and table 3.2). The power density supplied by the OMFC fed with EG (2.7 mWcm^{-2} at 1.4 V, figure 3.4-a and table 3.2) is lower than that observed with a traditional DAFC equipped with a palladium based anode [112]. No comparison can be made with DAFCs equipped with nanometer-sized metals as anodes fed with 1,2-P, 1,3-P, and 1,4-B simply because there are, at present, no data reported in the literature. In fact, the OMFCs described here are the first examples of direct alcohol fuel cells fed with these renewable diols. For a broader comparison, other fuel cells based on molecular-catalyst anodes have been reported to deliver 24 mWcm^{-2} for a direct CO polymer electrolyte membrane fuel cell (PEMFC), 26 mWcm^{-2} for a H_2 PEMFC at 60°C and 0.18 mWcm^{-2} for a direct glucose fuel cell, respectively [113–115]. The power density supplied by these OMFCs increases with cell temperature in active fuel cells (80 °C, fuel flow of 4 mL min^{-1} and an oxygen flow at the cathode of 0.2 L min^{-1}). Indeed, 12.4 mWcm^{-2}, 26.9 mWcm^{-2}, 24.3 mWcm^{-2}, and

42.2 mWcm^{-2}, were obtained with EG, 1,2-P, 1,3-P, and 1,4-B, respectively (figure 3.4-b, table 3.2).

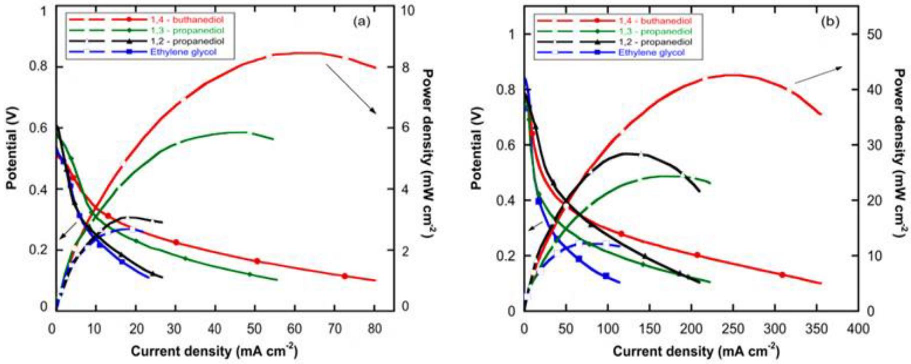

Figure 3.4: Polarization (●) and power density (○) curves of OMFCs fueled with: (●) 2M 1,4-B; (♦) 2M 1,3-P; (▲) 2M 1,2-P; (■) 2M EG aqueous solutions in 2M KOH. (a) Passive air-breathing OMFC at 20 °C and (b) active OMFC at 80 °C.

Table 3.2: OMFCs performances at room temperature and 80°C.

Fuel	**Max. OMFC power density at room temperature (mW cm^{-2})**	**Max. OMFC power desity at 80°C (mW cm^{-2})**
EG	2.7	12.4
1,2-P	3.1	26.9
1,3-P	5.9	24.3
1,4-B	8.5	42.2

3.3.3. Catalyst stability and oxidation reaction selectivity

Chronopotentiometric experiments were performed to probe the catalyst stability, measuring the cell potential over time when a constant current load is applied to the device. These chronopotentiometric experiments performed in passive devices were repeated three times. A polarization curve was also recorded between each galvanostatic experiment to monitor the cell activity. Fresh fuel was employed for every experiment and before each new galvanostatic cycle; the anode compartment of the fuel cell was washed with distilled water before each experiment. Figure 3.5 (a) and (b) describes respectively the first cycle of the chronopotentiometric experiments performed at room temperature and 80°C for each fuel (EG, ■; 1,2-P, ▲; 1,3-P, ♦; 1,4-B, ●). Table 3.3 summarizes the chronopotentiometric experimental results; the energy provided by the OMFCs was calculated integrating over the galvanostatic time, the instantaneous power extracted from the cell ($V*i^2$). The observed potential loss over time is due to the variation of fuel concentration during the experiments. Between the first and the second cycles there is a duration time drop (figure 3.6-b), due to the formation, in the first cycle, of the $Rh[(trop_2NH)PPh_3]OOCR$ species (**4@C** in figure 3.9; $RCOO^-$ indicates the carboxylic compounds obtained from diol electrooxidation): this form of the complex is less active than the OH form of $Rh[(trop_2NH)PPh_3]OH$ (**2@C**, figure 3.9) [102]. The galvanostatic duration time remains stable between the second and the third cycles (figure 3.6-b). As already reported in the literature, the $Rh[(trop_2NH)PPh_3]OOCR$ complex obtained during the first chronopotentiometric experiment is the complex active form that oxidises the alcohols in the second and in the third galvanostatic experiments [57,102].

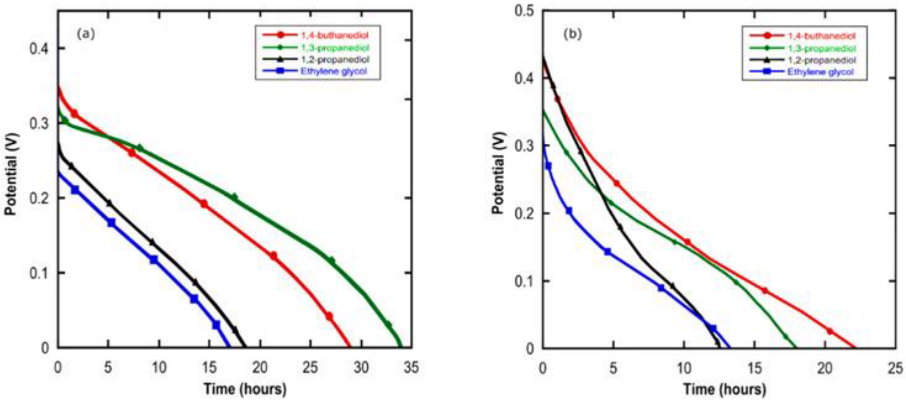

Figure 3.5: Galvanostatic curves of OMFCs at 20 mA, fueled with: (●) 2M 1,4-B; (♦) 2M 1,3-P; (▲) 2M 1,2-P; (■) 2M EG solutions in 2M KOH; (a) Air-breathing OMFC at 20 °C and (b) active OMFC at 80 °C.

The potentiodynamic experiments performed between each galvanostatic curve supports this hypothesis (figure 3.6-a): the power density delivered after the first galvanostatic cycle is about 50% lower than the power density delivered before the chronopotentiometric experiments. This value remains stable in the following cycles.

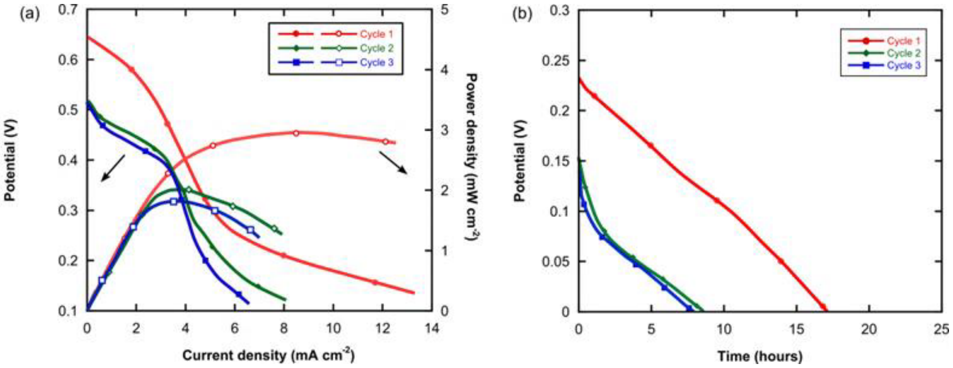

Figure 3.6: (a) Polarization and (b) galvanostatic curves at room temperature of OMFC fueled with 2M EG 2M KOH, cycle 1 (●), cycle 2 (♦) and cycle 3 (■).

Table 3.3: Chronopotentiometric experiments performed at room temperature and 80°C.

Fuel	**Cycle**	**Galvanostatic time at room temperature**	**Energy provided (J) at room temperature**	**Galvanostatic time at 80°C**	**Energy provided (J) at 80°C**
EG	I	17h:14m	142	12h:45m	587
	II	8h:53m	36	/	/
	III	8h:30m	36	/	/
1,2-P	I	18h:17m	154	12h:39m	826
	II	10h:05m	48	/	/
	III	8h:20m	33	/	/
1,3-P	I	34h:16m	472	17h:29m	1083
	II	24h:05m	238	/	/
	III	22h:24m	174	/	/
1,4-B	I	28h:38m	388	22h:11m	1317
	II	22h:27m	246	/	/
	III	20h:00m	184	/	/

3.4. Selectivity in the electrooxidation of the alcohols

Table 3.4 summarizes the EG, 1,2-P, 1,3-P and 1,4-B oxidation products determined after the first cycle of the chronopotentiometric experiments performed at room temperature and 80°C. No significant differences in the reaction product distribution were found after the second and the third set of galvanostatic experiments. The turn over number (T.O.N.) was calculated dividing the mmol of the obtained products of the first galvanostatic cycle with the Rh loading on the electrode expressed in mmol.

The OMFCs fed with EG and 1,2-P, yielded selectively glycolate and lactate, respectively. The galvanostatic experiments (20°C) with 1,3-P gave 3-hydroxy-propanoate (92%) and malonate (8%) with a total conversion of 83%. Using 1,4-B, 4-hydroxy-butanoate (79%) and succinate (21%) were obtained, with a total conversion of 79%.

Table 3.4: OMFCs oxidation products.

Fuel	Conversion [%] ([mmol])	Products	T.O.N.
Room temperature			
EG	38% (3.2)	100% glycolate	86
1,2-P	50% (3.4)	100% lactate	92
1,3-P	83% (6.1)	92% 3-hydroxypropanate 8% malonate	173
1,4-B	78% (5.3)	79% 4-hydroxybutanoate 21% succinate	114
80°C			
EG	28% (12.1)	100% glycolate	392
1,2-P	34% (12.0)	100% lactate	318
1,3-P	45% (16.3)	96% 3-hydroxypropanate 4% malonate	445
1,4-B	79% (18.4)	74% 4-hydroxybutanoate 26% succinate	486

The differences in activity and selectivity for the diol oxidation is due to both electronic and steric factors: EG and 1,2-P have primary and secondary vicinal hydroxyl groups that limit the diol electrooxidation to only one primary hydroxyl group. On the other hand, the longer aliphatic chain between the two OH groups in 1,3-P and 1,4-B makes possible the oxidation of both the alcoholic functionalities. This hypothesis was demonstrated by the testing of a passive OMFC fed with a 2M solution of 3-hydroxypropanoic acid (Sigma-Aldrich) and 2M KOH: the cell peak power density output was 0.7 mW cm^{-2}. A galvanostatic experiment (4 mA cm^{-2} constant current) was performed and showed a duration time of 11 hours, with a fuel conversion into products of about 30%. The quantitative and qualitative analysis of the fuel exhaust showed the formation of 100% malonate (figure 3.7). This result clearly indicates that 3-hydroxy-propanoate is easily oxidized by the Rh[(trop$_2$NH)PPh$_3$]OTf/KtjBk catalyst and the oxidation product is malonate.

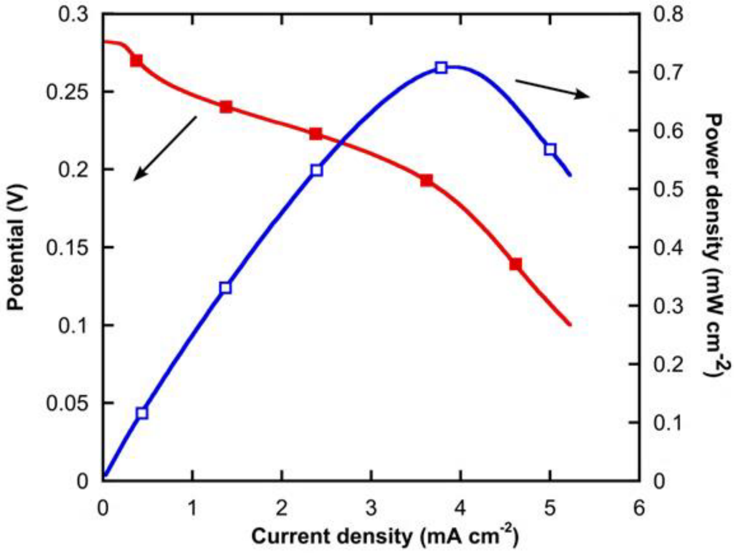

Figure 3.7: Polarization (■) and power density curve (□) of the OMFC fed with a 2M solution of 3-hydroxyporpanoic acid in 2M KOH.

Figure 3.8 summarizes the electrooxidation reaction pathways in alkaline solution of ethylene glycol, 1,2-propanediol, 1,3-propanediol and

1,4-butanediol. In OMFCs the reaction products are indicated by the circles [83]

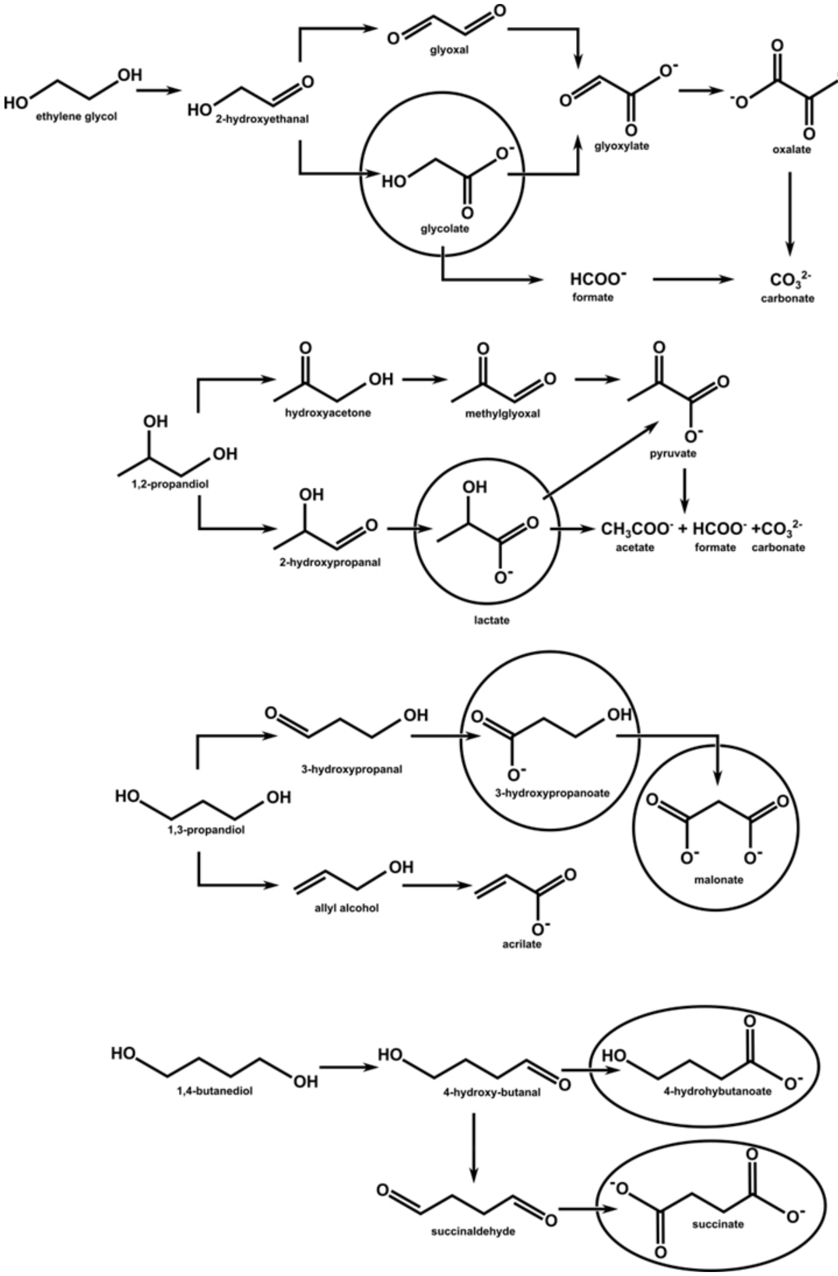

Figure 3.8: EG, 1,2-P, 1,3-P and 1,4-B electrooxidation pathways in alkaline environment. The circles indicate the chemical species obtained by OMFCs fed with these alcohols.

3.5. Reconstruction of the catalytic cycle

Following procedures reported in literature, model reactions in homogeneous solutions were performed to rationalize the alcohol oxidation mechanism in OMFCs [57,102].

All the solvents were used as purchased (Sigma-Aldrich, ACS purity grade) and were degassed prior to use. The glassware was dried at 120°C overnight. All the reactions were performed with a standard Shlenk-vacuum apparatus.

3.5.1. Model reactions

- 20 mg (0.022mmol) of $Rh[(trop_2NH)PPh_3]OTf$ were dissolved in an NMR tube with 1mL of THF-d_8. 250 µL of a 2M EG or 2M 1,2-P 2M KOH deareated solution were added to the starting mixture and a $^{31}P\text{-}\{^1H\}$-NMR spectrum was recorded. $Rh[(trop_2NH)PPh_3]OTf$ reacts immediately with the alcohol/KOH solutions to form the $Rh[(trop_2NH)PPh_3]H$ species, **5@C** in figure 3.9. $^{31}P\text{-}\{^1H\}$-NMR spectra were recorded each hour for five hours: the hydride form of the complex remains stable during this time, in fact this species doesn't reduce spontaneously to the amido form but needs an hydrogen acceptor.
- 500 µL of the previous solution were treated with 500µL of a 2M glycolic or 2M lactic acid 2M KOH deareated solution and a $^{31}P\text{-}\{^1H\}$-NMR spectrum was recorded: $Rh[(trop_2NH)PPh_3]H$ (**5@C**) reacts immediately with glycolic acid or lactic acid to form the η^1-O-glycolate, $Rh[(trop_2NH)PPh_3](OOCCH_2OH)$, and the

η^1-O-lactate, Rh[(trop$_2$NH)PPh$_3$](OOCCH(OH)CH$_3$), respectively (**4@C** in figure 3.9).

3.5.2. Proposed catalytic cycle

The model reactions gave the same results as reported in literature for ethanol electrooxidation with Rh[(trop$_2$NH)PPh$_3$]OTf/KtjBk [57,102]. Starting from this evidence and considering the composition of the OMFC fuel exhausts, it is possible to assume that Rh[(trop$_2$NH)PPh$_3$]OTf/KtjBk oxidizes polyols with the same process hypothesized for ethanol electrooxidation (figure 3.9) [57,102]:

- The Rh[(trop$_2$NH)PPh$_3$]OTf/KtjBk (**1@C**) is rapidly converted into Rh[(trop$_2$NH)PPh$_3$]OH/KtjBk (**2@C**) when the OMFC is fed with fuel. The hydroxylic form of the complex is in rapid equilibrium with the Rh[(trop$_2$N)PPh$_3$]/KtjBk (**3@C**); this is a rare example of the reversible addition of a water molecule to an amidic bond mediated by a transition metal center.
- The amide form of the complex, **3@C**, dehydrogenates the alcohol to the aldehyde (figure 3.10-A); The hydride form of the complex, Rh[(trop$_2$NH)PPh$_3$]H (**5@C**), is obtained.
- Under basic conditions, the aldehydes are quickly oxidized to carboxylic compounds by the **2@C** complex form (figure 3.10-B) and contemporaneously **5@C** is obtained. This reaction is so quick that it is impossible to isolate the aldehyde into the fuel.
- The hydride form **5@C** of the complex is regenerated to the amide form, **3@C**, releasing two electrons onto the anodic electrode and two H$^+$ into the solution.

- The **2@C** complex is in equilibrium with the Rh[(trop$_2$NH)PPh$_3$]OOCR form (**4@C**); this species is less but still active into the catalysis.

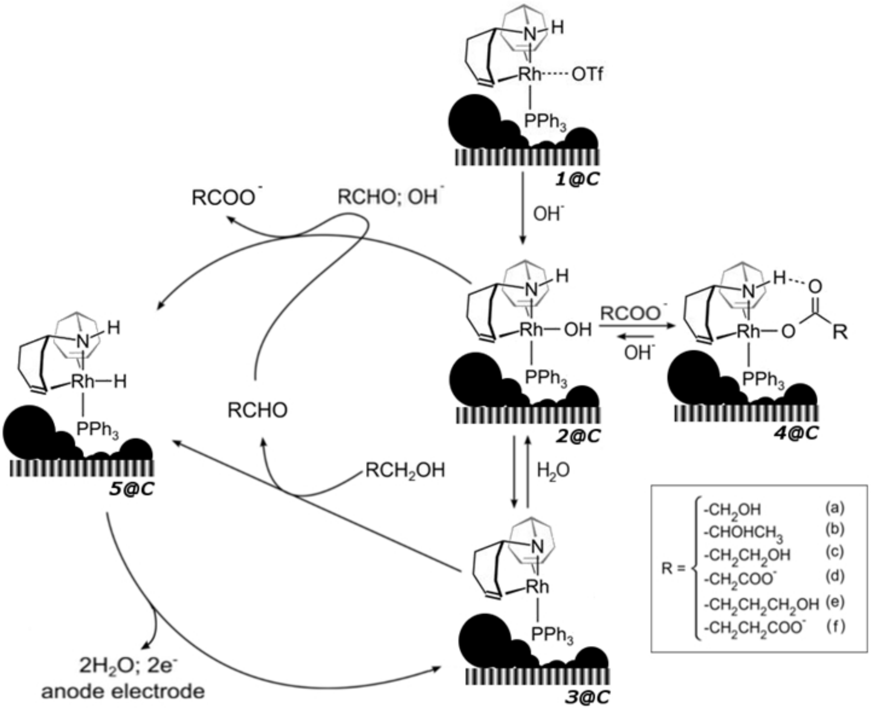

Figure 3.9: Supposed catalytic cycle for alcohols oxidation in OMFCs (EG (a), 1,2-P (b), 1,3-P (c), 3-hydroxypropanate (d), 1,4-B (e) and 4-hydroxybuthanoate (f)) [102].

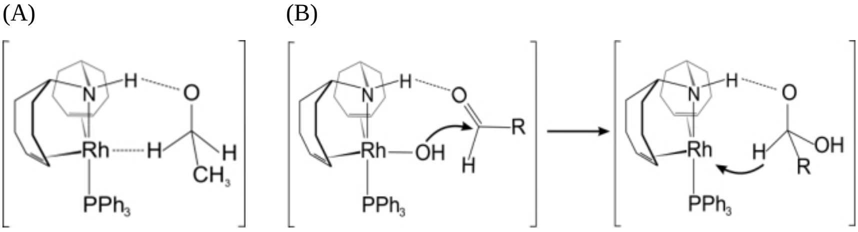

Figure 3.10: Transition state of the alcohol oxidation to aldehyde by ***3@C*** *(A), transition state of the aldehyde oxidation to carboxylate by* ***2@C*** *(B)* [57].

3.6. Investigation on complex degradation

In order to exclude that the Rh[(trop$_2$NH)PPh$_3$]OTf/KtjBk decomposes to Rh(0) nanoparticles during activity, the anodic catalyst of an active cell (80°C) fed with 1,2-P was recovered after several galvanostatic cycles. The sample was analysed by HAADF (High-Angle Annular Dark Feld detector)-STEM (Z contrast) microscopy. The micrograph in figure 3.11 shows the presence of single Rh atoms (of the complex) as bright spots (evidenced by white circles) and any traces of Rh nanoparticles or clusters. The exhausts catalyst was then treated with deuterated THF to extract the rhodium complex in solution. ^{1}H, ^{13}C and ^{31}P-NMR spectra of the extracted solution did not show any trace of complex degradation. An ICP-MS analysis of the anode exhausts after the galvanostatic experiments showed no rhodium leaching from the electrode into the solution.

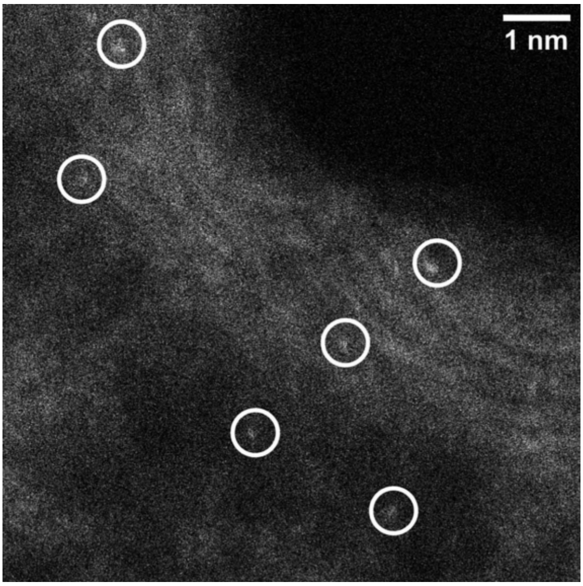

Figure 3.11: HAADF-STEM (Z contrast) image of the exhaust Rh[(trop$_2$NH)PPh$_3$]OTf/KtjBk anode. Circles evidence the Rh atoms. Scale bar: 1 nm.

3.7. Final overview

Alkaline DAFCs are one of the only devices that can exploit the chemical energy of a renewable source, a bio alcohol, transforming it in energy and chemical feedstocks working at low temperature and atmospheric pressure. The selectivity of the oxidation process is the key to match this goal as traditional palladium based anodic electrocatalysts fail in the selective oxidation of renewable polyols. Replacing such nanoparticle based catalysts with molecular complexes is the key to obtaining selective reactions. In this chapter, the molecular complex Rh[(trop$_2$NH)PPh$_3$]OTf/KtjBk was successfully employed for the selective oxidation of the renewable polyols; ethylene glycol, 1,2-propanediol, 1,3-propanediol and 1,4-butanediol. In particular EG and 1,2-P were oxidized to glycolate and lactate with 100% selectivity. In addition, this molecular complex produces the highest power density output amongst known anodic molecular catalysts: the OMFC fed with 1,4-B provided more than 40 mW cm^{-2} with only 1 mg$_{Rh}$ cm^{-2} of anodic Rh loading. The next challenge involves the reduction of the catalyst loading. Only a molecular catalyst, in fact, is able to match this goal, because, unlike nanoparticles, in an organometallic catalyst each metal site is active for the catalysis.

The concept of OMFCs represents a breakthrough in alkaline DAFC technology because this organometallic based device produces chemicals of industrial relevance with a contemporaneous release of energy at low temperature and atmospheric pressure. The alcohol oxidation selectivity of 100% for certain carboxylic compounds means less energy is spent in product separation systems. OMFCs match several principles of "green chemistry" [116] and are the "renaissance" of the concept of anodic catalysts for alcohol fuel cell. This concept was represented in a modified version of "Spring" of Botticelli, "The spring of OMFCs" (figure 3.12), in the cover picture of the journal "ChemSusChem"†.

The dance of the three graces is the fulcrum: they dance together forming a circle representing the three forms of the organometallic complex in the catalytic cycle for the selective electro-oxidation of diols obtained from renewable resources to the corresponding carboxylate compounds. Simultaneously, the electrons (Eros) move towards the cathode electrode (Flora and Zephyr), where oxygen is reduced to OH^- producing energy.

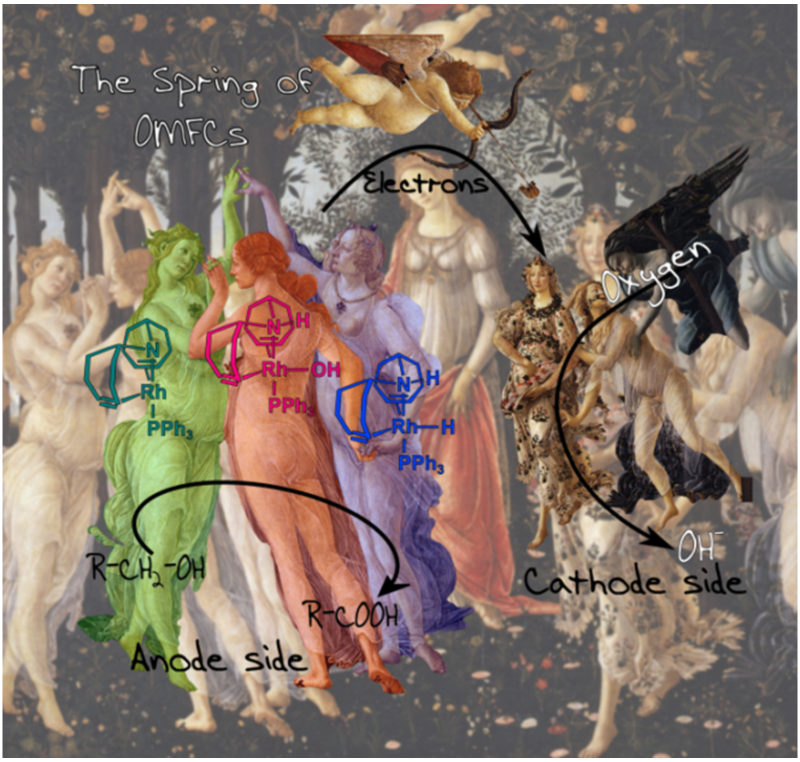

Figure 3.12: ChemSusChem cover picture, September 2014, vol 9.

---

† September 2014, volume 9. M. Bellini, M. Bevilacqua, J. Filippi, A. Lavacchi, A. Marchionni, H.A. Miller, W. Oberhauser, F. Vizza, S.P. Annen, H. Grützmacher

4. Platinum free H_2/O_2 anion exchange membrane fuel cells

4.1. Introduction

State of the art low temperature proton exchange membrane fuel cells (PEM-FCs) are compact, yet high power-density systems ideal for automotive applications [117]. Corrosion problems associated with the acidic nature of the proton exchange membrane (PEM) and the high cost of the platinum based anodic and cathodic electrocatalysts and of the Nafion® membrane, are the main limiting factor for these devices. Replacing the PEM with an alkaline anion exchange polymeric electrolyte (AEM) is one way to overcome these problems. H_2/O_2 fed anion exchange membrane fuel cells (AEM-FCs) are the most attractive alternative to traditional PEMFCs. In fact, the alkaline environment is less corrosive for FC components and allows in principle the use of non-noble metal based catalysts [75,76,118].

One of the first examples of a H_2/O_2 fed AEMFC equipped with non-Pt catalysts is described in this chapter. The cathodic catalyst used is based on heat treated iron and cobalt phthalocyanines impregnated on carbon black [71]. The anodic catalyst consists of Pd nanoparticles (10 wt.%) supported on a carbon/ceria ($C:CeO_2$) mixed support ($C:CeO_2$ = 50:50 wt.%). The membrane used is the Tokuyama® A-201 anion exchange membrane. The fuel cell provided a power density of ca. 200 mW cm^{-2} at 50°C. By comparison the best performing AEM-FCs equipped with Pt based electrocatalysts provide power densities of ca. 500 mW cm^{-2} [119–122]. The performance of the $Pd/C:CeO_2$ fuel cell was also compared with an AMFC equipped with an homemade standard Pd (10 wt.%)/C anodic catalyst.

4.1.1. The choice of the catalysts

In the AEM-FC cathode, Pt can be readily replaced by palladium or by non-noble metals [69–74,123]. The range of materials used include transition metal phthalocyanines, [70,124] heat treated (600-1000 °C) carbon supported metal phthalocyanines, [70–72,124] materials derived from carbon supported metal and nitrogen precursors heat treated under inert atmosphere (600-1000 °C) [125,126] and nitrogen doped carbon materials that may or may not contain transition metals [127,128]. Widely used in liquid electrolyte Alkaline Fuel Cells (AFCs), nanostructured Ag catalysts have also been extensively investigated [74,129,130]. A proprietary cathode catalyst (FeCo/C) was used in the current study. The synthesis of this material is fully described elsewhere [71].

Relatively less attention has been paid to the anode catalyst for the hydrogen oxidation reaction (HOR) [66,131–134]. In stark contrast to PEM-FCs, the HOR kinetics are quite slow in alkaline media even on Pt. Indeed, the HOR activity on carbon-supported noble metals (Pt, Pd and Ir) decreases by a factor of ca. 100 when switching from low to high pHs [135]. Sluggish HOR kinetics has been the main obstacle preventing the realization of a Pt free AEM-FC with useful power output. Little progress has been made since Lu and co-workers first demonstrated in 2008 a noble-metal-free H_2/O_2 AEM-FC generating 50 mW cm^{-2} at 60 °C [136][137].

Recently, Markovic et al. demonstrated that the HOR rate can be improved dramatically by optimizing the balance between the Pt or Pd active sites for H_2 adsorption and dissociation and the adsorption of hydroxyl species (OH_{ads}) on the catalyst surface, RuO_2 [138]. In this work a catalyst based on Pd nanoparticles (10 wt.%) supported on a blend of carbon black (Vulcan XC-72) and CeO_2 (50:50 wt.%) was investigated. Ceria is an oxygen deficient compound, whose surface is quickly saturated by OH^- species in alkaline conditions, so an intimate contact between CeO_2, carbon and Pd can enhance HOR kinetics [139,140]. In addition, Pd/C:CeO_2 (50:50 wt.%) has already shown an excellent activity for ethanol oxidation in DAFCs [58]. A mixed ceria-carbon support enhanced the activity of Pd anodes in Direct Ethanol Fuel Cells (DEFCs) by promoting the formation at low potentials of the $Pd^{(I)}OH_{ads}$ species that are responsible for ethanol electrooxidation.

4.2. Synthesis

The Pd (10 wt.%)/C:CeO_2 (50:50 wt.%) catalyst was synthesized according to procedures reported in the literature [119]. All solvents and the reactants were used as purchased (Sigma-Aldrich, ACS purity grade). The carbon support is Vulcan-XC72 purchased from Cabot. Corporation (USA). The synthesis was performed with the standard Shlenk-vacuum glassware under nitrogen atmosphere.

4.2.1. C:CeO_2 support

In a round bottom flask, 5.31g of $Ce(NO_3)_3*6H_2O$ (12.2 mmol) were dissolved in 250 mL of bidistilled water under magnetic stirring. Vulcan XC-72 (4g) was added to the solution and the mixture was kept under stirring for 30 minutes. Subsequently, the suspension was homogenized for 30 minutes by ultrasonic treatment at 20 kHz, 60 W

(Bandelin SONORPULSE UW2200 SERIES). An aqueous 2M KOH solution was added dropwise (ca. one drop every 3 seconds) until pH 12 was obtained. The resulting suspension was stirred vigorously for 2 hours. The solid product was then separated by filtration and washed with H_2O until neutral pH. The product was dried under air at 65°C. The solid thus obtained was heated under air for 2 hours, in a quartz-tube oven heated at 250°C. The solid was cooled down to room temperature under Ar flow. The C:CeO_2 yield was 6.24 g.

4.2.2. Pd/C:CeO_2

In a 1L beaker, 6.2 g of C:CeO_2 were suspended in 500 mL of bidistilled water for 30 minutes by vigorous magnetic stirring. The suspension was then homogenized for 10 minutes with ultrasound treatment at 20 kHz, 60W. A solution of K_2PdCl_4 (0.93 g, 2.84 mmol) in water (250 mL) was slowly added (ca. 3 hours) using a peristaltic pump (Gilson, minipulse). The solution was kept under vigorous stirring during addition. Thirty minutes after the addition, 14.5 mL of an aqueous solution of 1M KOH were added to the solution (under stirring). 100 mL of Ethanol were then added, and the mixture was heated at 80 °C for 30 minutes. The resulting solid (Pd/C:CeO_2) was filtered off, washed several times with distilled water to neutrality and finally dried under vacuum at 40° C until a constant weight of 6.46 g. ICP-MS analysis revealed a Pd content of 11.1 wt.%.

4.2.3. Pd/C

The Pd(10wt.%)/C benchmark catalyst was synthesized as described elsewhere [141].

In a 500 mL three-necked round-bottomed flask, Vulcan XC-72 (5.94 g) was suspended in 250 mL of ethylene glycol by one hour of mechanical stirring and then by 20 min of ultrasound treatment (20 kHz, 60W). A palladium (II) aqueous solution was obtained dissolving 1,2 g of $PdCl_2$ (6.20 mmol) in 6 mL HCl (37 %) and 44 mL of bidistilled water. The solution was added drop wise (3 second per drop ca.) to the carbon dispersion under vigorous stirring. After the addition, the palladium salt was impregnated on the carbon by keeping the suspension under one hour of mechanical stirring. A solution of 5.1 g of NaOH (127.5 mmol) in 10 mL of bidistilled water was added dropwise (3 seconds per drop) and the mixture was heated to 140°C (reflux conditions) under an inert N_2 atmosphere. After 3 hours, the reaction mixture was cooled to room temperature and the solid product was filtered and washed with bidistilled water to neutral pH. The final product was dried at 40 °C under vacuum to constant weight. The reaction yield is 4.47g. The ICP-MS analysis revealed a real Pd loading of 9.6 wt.%.

Prior to use, the catalytic powder was milled in a planetary steel ball mill (30 min, 250 rpm).

4.3. Morphological Characterization

4.3.1. Chemisorption measurements

The BET data reported in table 4.1 show that the addition of ceria CeO_2 to the Vulcan XC-72 carbon reduces significantly the surface area of the mixed support, from 222 to 140 m^2g^{-1}. On the contrary, the deposition of Pd NPs onto the $C:CeO_2$ support does not affect the overall surface area. The active metal surface area of the palladium nanoparticles was measured by chemisorption experiments (table 4.1): Pd NPs have a high metal dispersion specific surface area of 236 $m^2g_{Pd}^{-1}$ with a calculated mean particle diameter size of 2.1 nm.

Table 4.1: Chemisorption physical data.

Sample	BET (m^2g^{-1})	Specific surface area ($m^2g_{Pd}^{-1}$)	NPs size (nm)
C	222	/	/
$C:CeO_2$	140	/	/
$Pd/C:CeO_2$	145	236	2.1

4.3.2. Transmission electron microscopy

TEM images of $Pd/C:CeO_2$ show the Pd NP dispersion on the $C:CeO_2$ catalyst support (figure 4.1). The high-resolution HR-TEM image, reported in figure 4.1-b, shows in detail a Pd nanoparticle, deposited next to a ceria nanoparticle; the Pd particle and the CeO_2 particle have respectively the typical lattice spacings of Pd (111) and Ce (002). The average Pd/C:CeO_2 nanoparticle diameter determined from HR-TEM images is 2.1 ± 0.53 nm (figure 4.2).

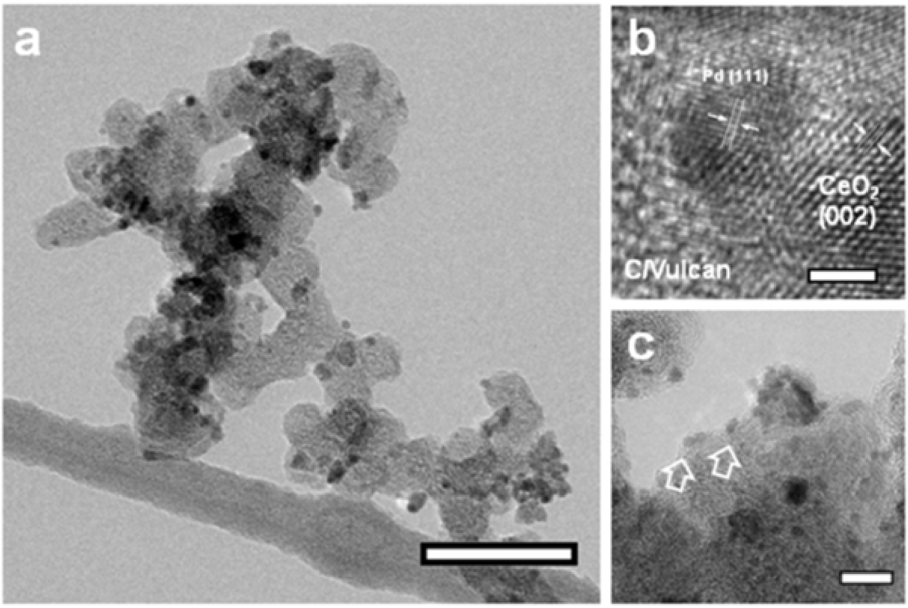

Figure 4.1: TEM images at (a) low magnification (scale bar 50 nm) and (b, c) high magnification of the Pd/C:CeO_2 catalyst (scale bars 2 and 5 nm respectively). The white arrows in (c) point out the Pd nanoparticles.

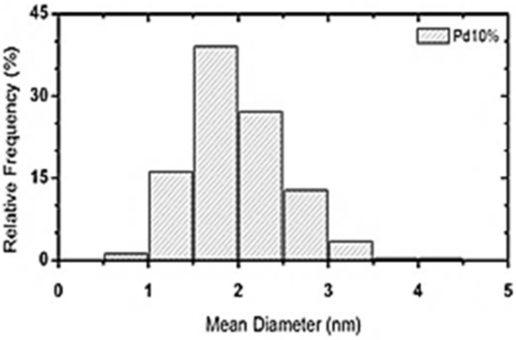

Figure 4.2: Histogram diagram of the Pd/C:CeO_2 nanoparticles diameters.

Z-contrast STEM images (figure 4.3) help to elucidate the structure of the ceria portion of the sample. These images show a non-uniform distribution of the CeO_2 aggregates on the carbon surface. In the micrographs, ceria appears brighter with respect to the carbon black. It is difficult to individualize isolated Pd nanoparticles deposited on the ceria part of the support due to poor resolution between CeO_2 and Pd nanoparticles. Consequently, the average Pd particle size distribution (above) represents only the visible carbon supported particles.

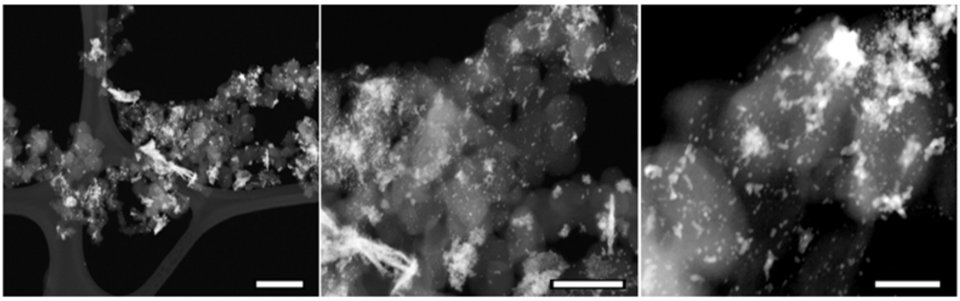

Figure 4.3: STEM images of Pd /C:CeO_2. Scale bars from left to right: 200 nm, 100 nm and 50 nm respectively.

STEM-EDX elemental map analysis of the Pd/C:CeO_2 catalyst (figure 4.4) confirm a marked accumulation of Pd on the ceria phase of the catalyst. This affinity can be justified by the fact that the conditions of high pH during synthesis gives rise to strong ionic interactions between the charged ceria surface and the Pd precursor cations in solution [142,143]. Combined with the lipophilicity of the carbon part of the support these factors ultimately lead to the deposition of Pd nanoparticles on or near the ceria regions.

This unusual catalyst architecture is the source of the HOR enhancement.

This is because CeO_2 can improve OH^- transfer from the membrane (and the ionomer) to the Pd NP surface, where they are involved in the HOR (figure 4.15). Further ESI analysis performed on the HR-TEM micrographs show the CeO_2 distribution on the carbon portion of the support (figure 4.5).

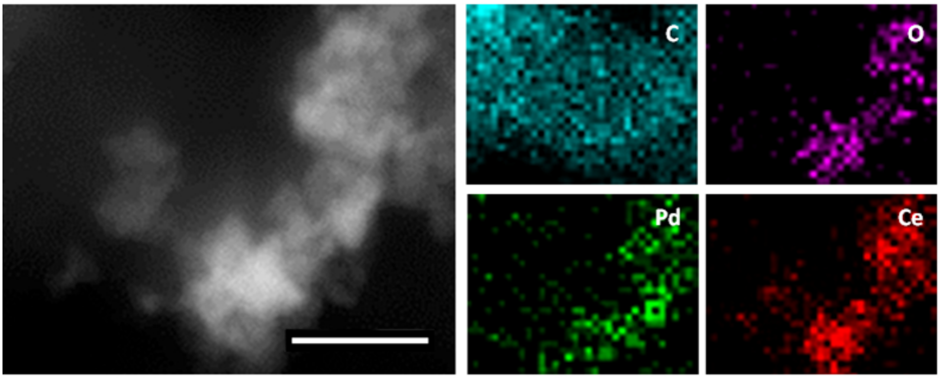

Figure 4.4: STEM image of Pd/C:CeO_2 (scale bars: 20 nm). The respective EDX map for C, O, Pd and Ce is reported next the STEM image.

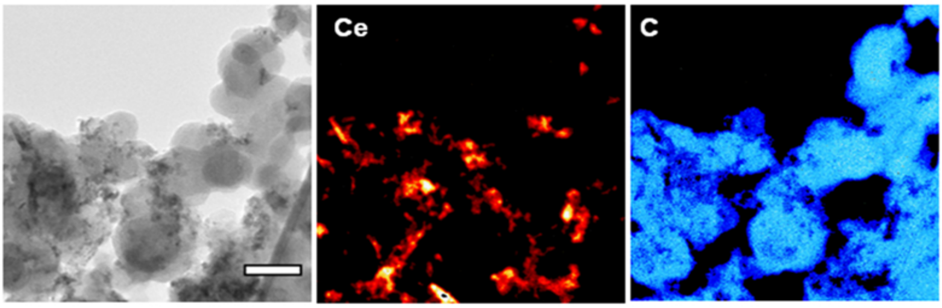

Figure 4.5: TEM micrograph of Pd/C:CeO_2 and related ESI map for Cerium and Carbon. Scale Bar is 50 nm

TEM micrographs were recorded also of the Pd/C sample (figure 4.6). The Pd nanoparticles are well dispersed over the carbon support and have a mean diameter of ca. 2-4 nm.

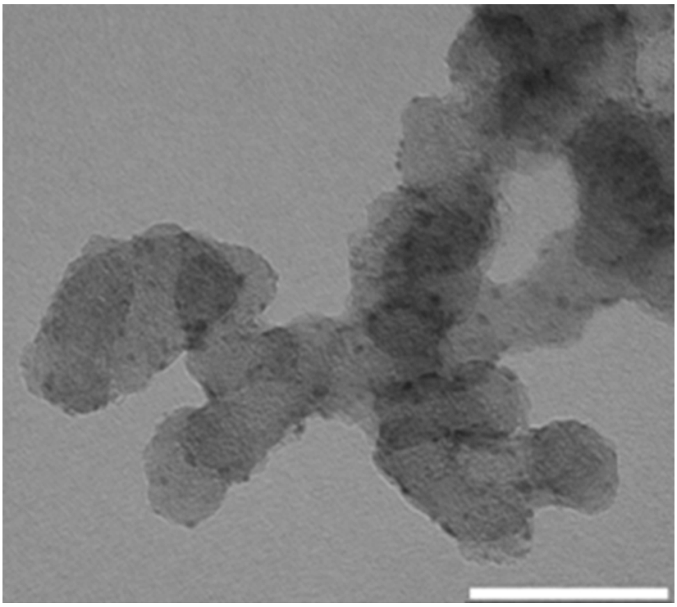

Figure 4.6: TEM micrograph (scale bar 20 nm) of the Pd/C catalyst.

4.3.3. X-rays absorption spectroscopy

The Pd oxidation state in the Pd/C and Pd/C:CeO_2 catalysts was investigated by X-ray Absorption Spectroscopy (XAS). Spectra were also collected on PdO and on a foil of metallic Pd as standard materials for the valence state as in our previous investigations [144].

In figure 4.7, a comparison of the XANES (X-ray Absorption Near Edge Structure) spectra clearly shows that Pd in Pd/C:CeO_2 is mostly oxidized, while in Pd/C the palladium is prevalently in its metallic state. EXAFS (Extended X-ray Absorption Fine Structure) analysis was carried out modeling the data with two components, i.e. metallic Pd and PdO. The metal was introduced with the first coordination shell whereas for the oxide two shells (Pd-O and second Pd-Pd) were considered. The raw EXAFS data and related Fourier Transforms are shown in figure 4.8.

The EXAFS analysis shows Pd$^{(II)}$ accounts for 87 wt.% of the total palladium content in Pd/C:CeO_2 (figure 4.8 and

table 4.2), which is unusual as carbon supported Pd NPs of small dimensions (e.g. 2 nm) that usually have at least 50 wt.% in the metallic state [145].

As expected only 17 wt.% of PdO was found in the Pd/C system. The considered coordination shell distances R (Å) of Pd and the relative Debye Waller Factors (DWF) s2 (Å^2) are shown in table 4.3. The bond distances and DWF data of the samples closely reproduce the values of the Pd standards confirming that the Pd$^{(II)}$ present is effectively PdO (and not some other species of divalent Pd). The XAS data therefore shows for the C:CeO_2 supported catalyst that the Pd exists primarily as oxide. This confirms that Pd is preferentially supported on the ceria regions of the catalyst as Pd NPs supported on CeO_2 are generally found in the oxidized form [146]. Strong interactions between Pd and CeO_2 lead to charge transfer from Pd to Ce-O [147].

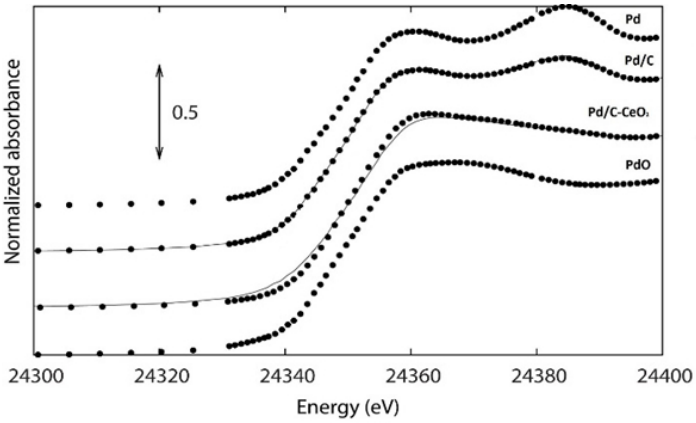

Figure 4.7: XANES at the Pd-K edge of Pd/C:CeO_2, Pd/C and model compounds Pd metal and PdO (dots). The spectra of the samples are reproduced as linear combinations of the model compounds (thin line).

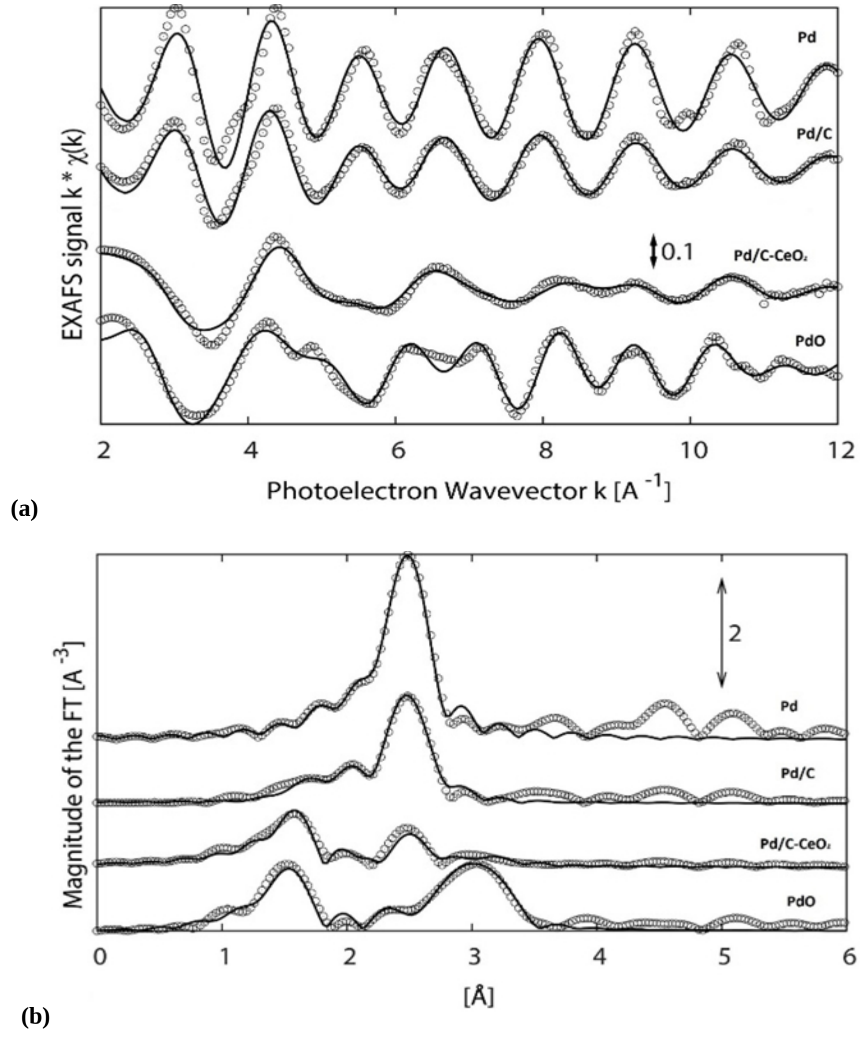

Figure 4.8: (a) EXAFS data and the related (b) Fourier transforms at the Pd Kα edge (transformation range 2.8-13.5 Å-1, k2 weight). Dots represent the experimental data while the continuous lines represent the best fits.

Table 4.2: Pd speciation from EXAFS and XANES analysis. Relative uncertainties are listed in brackets.

Sample	Pd metal (wt.%)	Pd oxide (wt.%)
Pd/C	82 (±6)	18 (±6)
Pd/C:CeO_2	13 (±5)	87 (±5)

Table 4.3: Best fit EXAFS parameters for the analysed samples. Bond distance R (Å), relative to both the first and the further shells, when present, are listed. The first shell DWF parameter, s2 (Å^2), are provided. Relative uncertainties in brackets.

Metallic phase				Oxide phase			
Sample	**Metal Fraction (%)**	**R Pd-Pd (Å)**	**s2 Pd-Pd (Å^2)**	**R PdO (Å)**	**s2 PdO (Å^2)**	**R Pd-Pd (Å)**	**s2 Pd-Pd (Å^2)**
Pd metal	/	2.74 (±1)	0.0054 (±3)	/	/	/	/
Pd/C	82 (±6)	2.73 (±2)	0.0076 (±6)	2.03 (±2)	0.0006	/	/
Pd/ C:CeO_2	13 (±5)	2.77 (±2)	0.004 (±2)	2.00 (±2)	0.0006	2.98 (±3) 3.36 (±3)	0.015 (±4)
PdO	/	/	/	2.01 (±2)	0.0006 (±5)	3.04 (±3) 3.43 (±3)	0.0026 (±8)

4.3.1. X-rays powder diffraction

The XRPD pattern of Pd/C (figure 4.9-A) shows the typical diffraction peaks of Pd face centered cubic structure: the peaks at 2θ = 40°, 46°, 68°, 82° and 84° are the reflections of the (111), (200), (220), (311) and (222) planes of the palladium fcc; carbon (002) has a signal at 2θ = 25° [58]. The Pd (111) fcc reflection is present even in the Pd/C:CeO_2 diffractogram (figure 4.9-B). The peaks at 2θ = 29°, 32°, 47°, 69°, 77°, 79°, 88° and 95° are the $Ce^{(IV)}$ oxides signals [58].

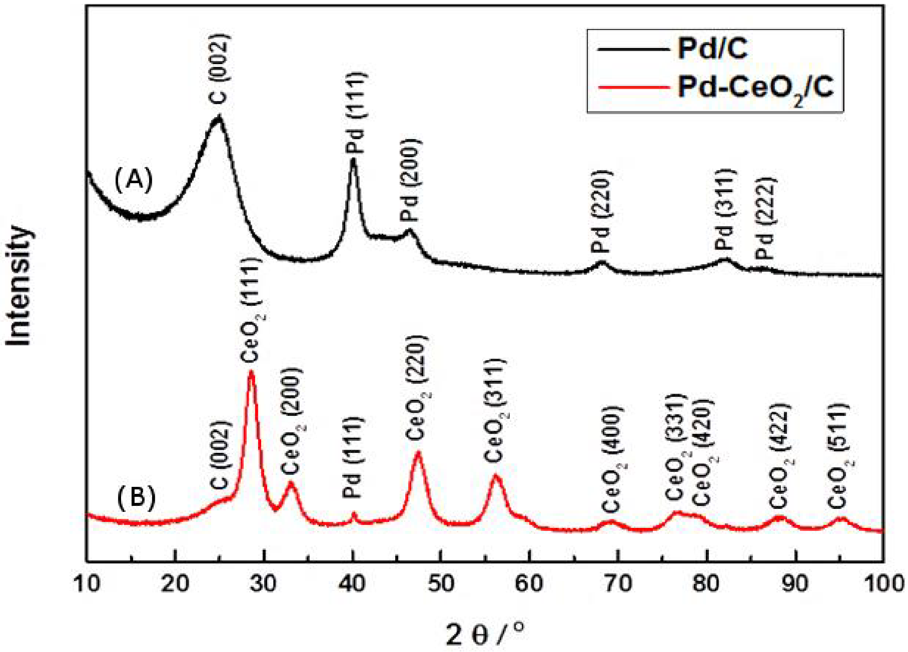

Figure 4.9:X-ray powder diffraction spectra of (A) Pd/C and (B) Pd/C:CeO_2.

4.3.1.1. In situ X-rays powder diffraction

Pd/C:CeO_2 has an enhanced electrochemical activity for the HOR (see next paragraph). The XAS measurements however show that this catalyst is mainly composed of Pd oxides. PdO species are inactive in the hydrogen oxidation reaction. To justify the catalyst electrochemical activity, it is reasonable to assume that the PdO species are easily reduced to metallic Pd during electrocatalysis, so Pd/C:CeO_2 is just a catalyst precursor: the active phase is generated in situ in the MEA by the reducing anodic environment (H_2 flow at 55°C). In-situ XRPD under flowing H_2 gas at room temperature was used to simulate the conditions at the anode electrode in the complete anion exchange membrane fuel cell. These experiments easily demonstrate the hypothesis of the PdO unactive species reduction to the active Pd metallic one.

In the fresh catalyst diffractogram (figure 4.10-a), the metallic Pd (111) reflection (●) is a low intensity broad peak; this shape is typical of a Pd nanoparticle based catalyst with a very low nanoparticles loading. When the XRPD experimental chamber is saturated by flowing a mixture of 5% H_2 and Helium gas (figure 4.10-b), the Pd (111) peak grows in intensity because the palladium oxides are reduced to metallic Pd. Upon further contact with H_2 gas (figure 4.10-c), this reflection shifts to the position representative of H_2 loaded Pd (■) [148]. Purging the cell with Helium flow to remove H_2, the signal for Pd shifts again to the position of Pd (111) fcc (figure 4.10-d).

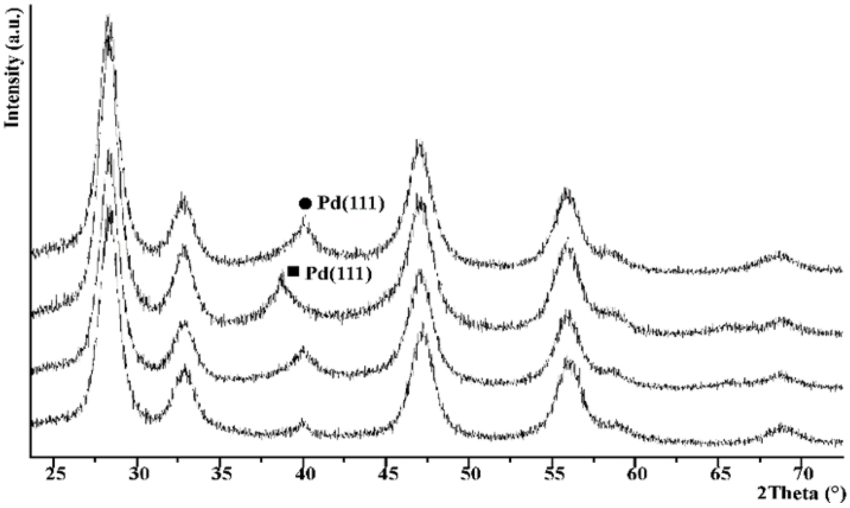

Figure 4.10: In-situ XRPD spectra of (a) Pd/C:CeO_2 fresh catalyst, (b) Pd/C:CeO_2 catalyst under a flow of H_2 (5 %) in He, (c) Pd/C:CeO_2 after a long period of contact with H_2 and (d) Pd/C:CeO_2 spectra after switch to 100 % Helium. (●) is the Pd (111) reflection and (■) is the H_2 loaded Pd (111) signal. The other peaks in the XRPD traces are the CeO_2 reflections.

4.4. Electrochemical characterization

The Pd/C:CeO_2 catalyst was electrochemically characterized first by half cell measurements: cyclic voltammetric experiments and polarization curves were performed with a rotating disk electrode. The HOR on the Pd/C:CeO_2 catalyst was also investigated using Tafel plots from the polarization curves. The Pd/C:CeO_2 catalyst activity was compared with the standard Pd/C and with a commercial Pt (40 wt.%)/C catalyst. All the experimental details are described in chapter 7, paragraph 7.6.

These catalysts were also tested in complete fuel cells. First a FC equipped with both anodic and cathodic Pt/C based catalysts was realized as benchmark. Subsequently, the anodic Pt/C electrotatalyst was replaced with the Pd/C:CeO_2 one. Finally a totally platinum free FC was set-up (Pd/C:CeO_2 as anode and FeCo/C as cathode). Its activity was compared with the device equipped with the Pd/C anode and the FeCo/C cathode, in order to demonstrate the ameliorative effect of the support ceria:carbon (50:50 wt.%) in the Pd/C:CeO_2 anode activity, compared to the carbon only supported Pd catalyst. The procedures for the Membrane Electrode Assemby (MEA) fabrication and for the fuel cell assembly are fully described in chapter 7, paragraph 7.7.

4.4.1. Half cell measurements

Figure 4.11compares the cyclic voltammograms in 0.1 M KOH of Pd/C (●) and Pd/C:CeO_2 (■). The two voltammograms have the typical shape of Pd based electrocatalysts, in alkaline environment [149]:

- Forward scan.
  - The anodic peak A′ between 0.2 and 0.45 V vs RHE describes hydrogen under potential oxidative desorption.
  - The anodic peak A″ at 0.5 V vs RHE describes the formation of $PdOH_{ads}$ on the Pd nanoparticle surface.
  - After 0.6 V vs RHE there is an anodic current increase A‴ due to the formation of the PdO_{ads} species.
- Reverse scan.
  - The cathodic C′ peak between 0.8 and 0.4 V vs RHE defines the reduction of the PdO_{ads} species.
  - The peak C″ under 0.3 V vs RHE corresponds to hydrogen underpotential deposition (HUPD).

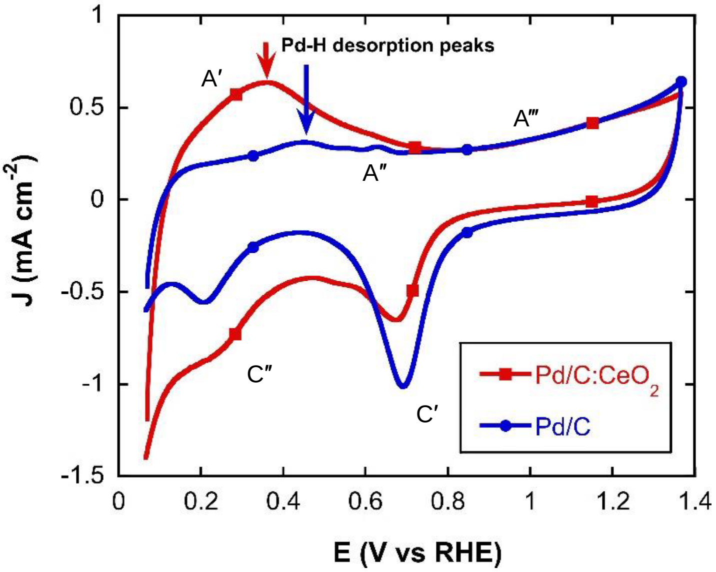

Figure 4.11: Cyclic voltammetry of Pd/C (●) and Pd/C:CeO2 (■) in 2 M KOH solution.

The Pd supported onto ceria-carbon blend catalyst has an HUPD desorption peak with higher current density compared to Pd/C. In addition, this peak has a negative shift of about 90 mV respect to the carbon supported catalyst. This shows that hydrogen is bound less strongly on the C:CeO_2 supported Pd surface. A weakening of the metal-hydrogen (M-H) binding energy leads to enhancements in HOR kinetics under alkaline conditions because the oxidative desorption of hydrogen is the rate determining step of this reaction [150]. The electrochemical active surface area (EASA) was calculated integrating the PdO_{ads} reduction peak at ca. 0.7 V vs RHE in the reverse scan; the data are reported in table 4.4 [149]. The two catalysts have a comparable EASA.

Table 4.4: half cell electrochemical data.

Catalys	**EASA** ($m^2g^{-1}_{Pd}$)	i_0 (mA cm_{Pd}^{-2})	$E_{plateau}$ (V vs RHE)	**Tafel slope** (mV dec^{-1})
Pd/C	45	2.7	/	68
Pd/C:CeO_2	43	54.5	0.25	66

This hypothesis is endorsed by the polarization experiments (figure 4.12), that show an increase in the HOR activity of Pd/C:CeO_2 compared to Pd/C. Pd/C:CeO_2 reaches the diffusion limiting current plateau at 0.25V vs RHE. On the contrary, the Pd/C catalyst does not reach the limiting current plateau at potentials below 0.5 V.

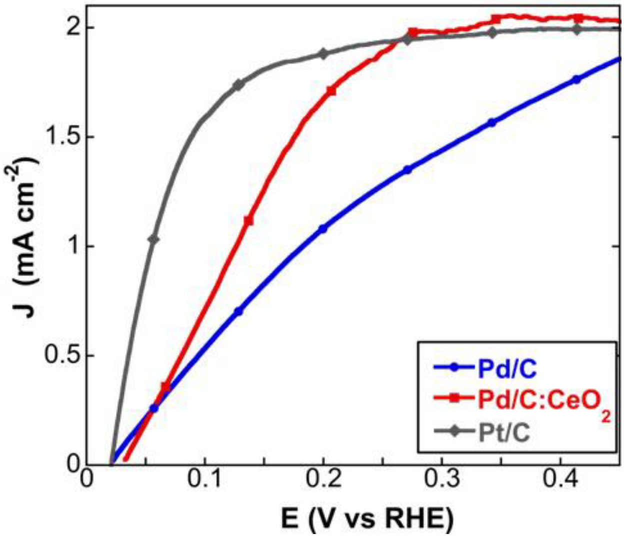

Figure 4.12: Steady state polarization curves at 1600 RPM of HOR in H_2 saturated 0.1 M KOH with Pd/C (●), Pd/C:CeO_2 (■) and Pt/C (♦).

Tafel slopes were determined from linear fits of the kinetic currents at high current density (figure 4.13). The exchange current densities for the HOR, calculated from the Tafel slopes, are ca. 20 times higher for the C:CeO_2 supported Pd catalyst respect to the Pd/C one (table 4.4).

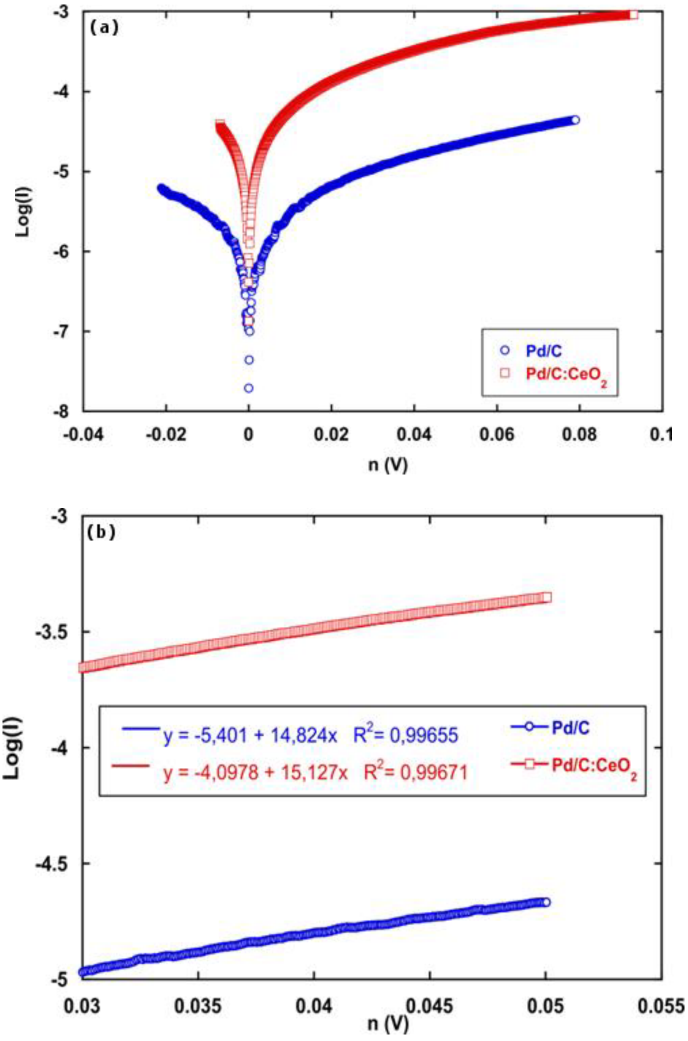

Figure 4.13: (a) Tafel slope analysis for Pd/C (●) and Pd/C:CeO_2 (■) in H_2-saturated, and (b) their linear fits of the kinetic current at high current density.

4.4.2. H_2/O_2 fed AMFCs

The Pt free FC equipped with the Pd/C:CeO_2 (0.3 mg_{Pd} cm^{-2}) anode provided a power density of 207 mW cm^{-2}, a result more than two times higher compared to the Pd/C fuel cell (0.3 mg_{Pd} cm^{-2}), that supplies a maximum power density of 74 mW cm^{-2}. In agreement with the half-cell measurements, the presence of ceria with the carbon support enhances the HOR on Pd.

Table 4.5 and figure 4.14, summarize the experimental results obtained from the complete cell electrochemical characterization.

Table 4.5: AMFCs performances.

FC (anode//cathode)	**OCV (V)**	**Max power density (mW cm^{-2})**
Pt/C//Pt/C	0.850	398 (@1095 mA cm^{-2})
Pd/C:CeO_2//Pt/C	1.060	302 (@760 mA cm^{-2})
Pd/C:CeO_2//FeCo/C	0.875	207 (@540 mA cm^{-2})
Pd/C//FeCo/C	0.695	74 (@ 240 mA cm^{-2})

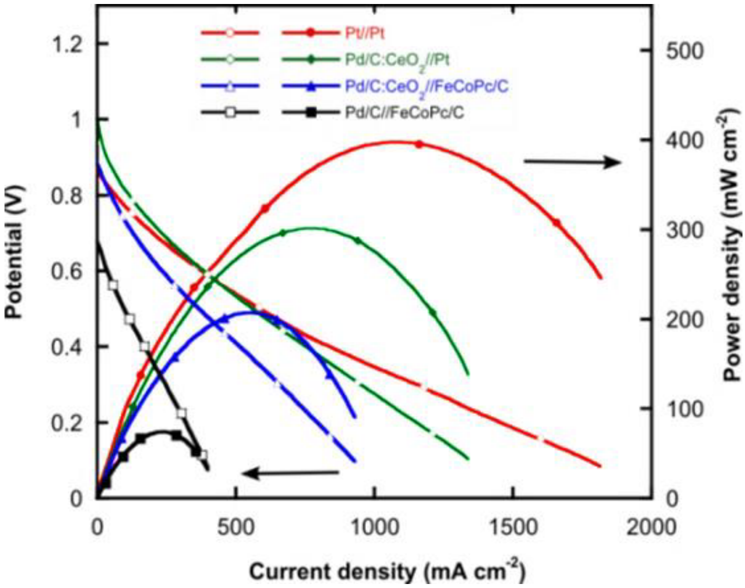

Figure 4.14: Polarization and power density curves for the (●,○) Pt/C//Pt/C, (♦,◊) Pd/C:CeO_2//Pt/C, (▲,Δ) Pd/C:CeO_2//FeCoPc/C and (■,□) Pd/C//FeCoPc/C.

The AMFC equipped with the Pd/C:CeO_2 anode and the FeCo/C cathode produced a maximum power density of ca. 200 mW cm^{-2} less than the standard Pt based device used as benchmark (0.44 mg_{Pt} cm^{-2} for each electrode). The difference may in part be due to the lower metal loading on the anode. In addition, the FeCo/C cathode performs poorly for the ORR in these operating conditions. Indeed, after replacing the FeCo based cathode with Pt/C, the AMFC equipped with Pd/C:CeO_2 provided a maximum power density of about 300 mW cm^{-2}. The gas fed AMFC operates without the liquid KOH electrolyte used in alkaline DAFCs where the FeCo/C cathode performs well, relying on the ionomer within the catalyst layer for ionic conductivity.

All the tested cells showed a similar maximum power density loss of about 15% during the ten polarization experiments performed in sequence. More investigation must be performed to understand the cell durability during long working time.

4.5. Mechanism of HOR and origin of enhanced activity with ceria

This unusual catalyst architecture is the source of the HOR enhancement.

This is mostly because CeO_2 can improve OH^- transfer from the membrane (and the ionomer) to the Pd NP surface, where they are involved in the HOR (figure 4.15). Such a structure also leads to a weakening of the Pd-H binding energy, which is considered the rate-determining step of the HOR in alkaline media. The enhancement of the catalyst activity towards the HOR therefore requires finely dispersed and small Pd and CeO_2 nanoparticles in contact with each other. Indeed, we have seen that Pd preferentially accumulates on the ceria regions. The adsorbed OH species that accumulate on the CeO_2 particles are in close proximity to the Pd NPs thus allowing fast transfer to form Pd-OH_{ads} sites, which then react with the hydrogen intermediates (Pd-H_{ads}) adsorbed on the Pd surface.

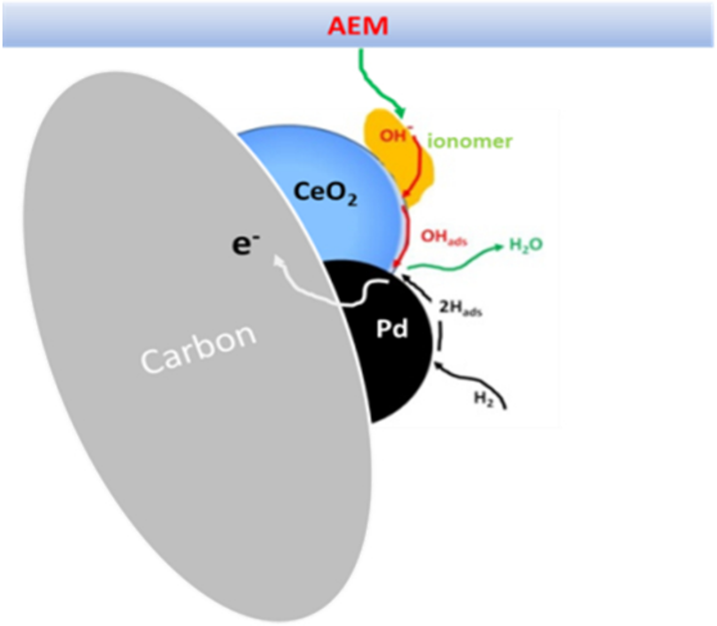

Figure 4.15: Schematic description of the mechanism of hydrogen oxidation onto the Pd/C:CeO_2 *anodic catalyst.*

4.6. Final overview

Replacing Nafion® with anion exchange membranes is a possible way to realize affordable and sustainable H_2/O_2 fed fuel cells. This is because in alkaline environment, Pt based catalysts can be replaced with non-noble metals on the cathode electrode and with Pd based catalysts at the anode. Palladium is still a noble metal but it has a higher natural abundance and a lower cost compared to Pt. The sluggish kinetics for the HOR in alkaline media is the main limitation of traditional anodic catalysts. In this chapter, it has been demonstrated that changing the architecture of the anodic support from carbon to a blend of carbon and ceria is the key to increasing anodic electrooxidative performance for the HOR. A complete Pt free H_2/O_2 AMFC was realized with a Pd/C:CeO_2 anodic catalyst and a FeCo/C cathode catalyst. The fuel cell provides a maximum power density of ca. 200 mW cm^{-2}, two times higher than the power density delivered from the analogous cell (100 mW cm^{-2}), equipped with a traditional Pd/C anodic catalyst. HR-TEM and STEM analysis, combined with half cell measurements, demonstrate that a strong Pd-ceria interaction is responsible for the improved HOR: in strong alkaline media, the CeO_2 surface is covered by OH_{ads} ions that transfer rapidly to the Pd nanoparticles in close proximity resulting in improved hydrogen oxidation kinetics.

5. Anion exchange membrane alcohol electroreformer

5.1. Introduction

Hydrogen production from electrolytic water splitting in polymer exchange membrane electrolysers (PEME) is an energy intensive process. In fact, 1.23 V is the minimum potential required (the equilibrium potential) for the water electrolysis process. This value increases to ca. 2.0 V to overcome kinetics factors and to speed up the reactions in order to evolve a reasonable hydrogen volume. Consequently, the lowest PEME electrical energy consumption is about 50-55 kWh $kg_{H_2}^{-1}$. Such high potentials applied to the device combined with the strong acidic environment of the membrane limit the choice of electrocatalytic materials to rare and expensive metals: Ir, Ta or Ru for the anodic electrocatalyst and Pt for the cathodic one [27,89].

Hydrogen production from alkaline electrochemical reforming of an alcohol lowers the energy consumption to about 26 kWh $kg_{H_2}^{-1}$ because the equilibrium potential of the process is lowered to 0.106 V by replacing the thermodynamically unfavorable oxygen evolution reaction (OER) with the easier partial oxidation to carboxylic compounds of biomass-derived alcohols at pH = 13 [27,89]. At the anode, Pd may be used for the alcohol oxidation reaction [27,89].

As already demonstrated for organometallic fuel cells, the selective and simultaneous production of energy, stored in the hydrogen chemical bond, and industrially relevant chemicals, the carboxylic compounds, allows to completely exploit the starting resource, a renewable alcohol, without the generation of byproducts [83,86].

The efficiency of the process will of course depend upon how selective the process is for the production of any desired compound. At the state of the art, Pd based anodic electrocatalysts employed in alcohol electroreformers show a 100% selectivity for ethanol oxidation to acetate but they fail in the selective oxidation to carboxylic compounds of renewable and industrial relevant polyols like ethylene glycol, 1,2-propanediol and glycerol [27,42,89,92].

In this chapter, the electrochemical activity for electroreforming of an anodic electrocatalyst based on Au-Pd core-shell nanoparticles (Au@Pd) supported onto carbon black (C) Vulcan XC-72 is described. The unique structure of these catalysts confers high electrooxidative activity for the oxidation of small organic molecules, like ethanol and formate [151–154]. An electroreformer has been realized with the Au@Pd/C anodic catalyst, a commercial (E-tek) Pt/C cathodic electrocatalyst and a Tokuyama® A-201 anion exchange membrane. The device was fed with small aliphatic renewable alcohols: ethanol (EtOH), ethylene glycol (EG), 1,2-propanediol (1,2-P), 1,3-propanediol (1,3-P), 1,4-butanediol (1,4-B) and glycerol (G). The Au@Pd/C catalyst is shown to have an high selectivity for ethylene glycol and 1,2-propanediol oxidation to glycolate (86%) and lactate (87%) respectively. In addition, the energy consumption of about 20 kWh $kg_{H_2}^{-1}$ is in line with the best electroreformers yet reported in the literature [27,89].

5.1.1. The choice of the catalyst

Bimetallic nanoparticles composed of a gold core and thin palladium shell have unique optical, catalytic and electronic properties compared to the monometallic one [154]. In particular, the synergistic effect between the two metals increases the catalyst activity, selectivity and stability with respect the corresponding pure Pd based system [155]. In fact, the alloying effect of Au and Pd has been shown to enhance the performance in the electrooxidation of small organic molecules like formate, methanol and ethanol in alkaline direct alcohol fuel cells and direct formate fuel cells [151,153,154,156]. The electronic effect of such a structure shifts the d-band centre of palladium to the Fermi level, enhancing Pd electrocatalytic performances [152]. In addition, the synergistic effects between gold and palladium accelerate the removal of the poisoning intermediates during the alcohol oxidation reaction and suppresses Pd oxidation [152,153,157]. The shape control of the nanoparticles is one of the best methods for improving catalytic performance, which are highly dependent on the crystallographic planes that terminate the NPs surface. High index faceted NPs with sizes below 15 nm can exhibit much improved catalytic performance, however, they have also proved challenging to synthesize [158,159].

Finally, the use of a cheaper and more available metal (Au) in the nanoparticle core allows to reduce the loading in the catalyst of the more expensive palladium [160].

5.2. Synthesis

The synthesis was performed by Dr. Christoph Hasenöehrl of the Victoria University of Wellington and it consists in three main steps: the synthesis of the Au seeds, the Pd shell growth onto the seeds and the Au@Pd NP deposition onto carbon black. As shown by Henning et al., the palladium thickness can be easily tuned by adjusting the reaction time [158]. Palladium was grown onto the gold seeds for two hours, as previous studies showed that this yields the optimal bimetallic composition for catalysis [158,159]. Thicker layers of palladium reduced the synergistic effects and lowered the efficiency of catalytic reactions.

All the reactants were used as purchased (Sigma-Aldrich, ACS purity grade). The synthesis was performed with standard Shlenk-vacuum techniques, under nitrogen atmosphere.

5.2.1. Au seeds

In an 11 mL vial, 17.8 mg (0.05 mmol) of gold chloride trihydrate were dissolved in 1 mL of toluene with 185.3 mg (1 mmol) of dodecylamine (Aldrich, 98%), which has the role of stabilizing agent for the NPs growth. The vial was then suspended in a 300 mL Fischer-Porter reaction vessel, containing 10 mL toluene. The vessel was fitted with a valve and purged three times with vacuum and 1 bar hydrogen gas. The vessel was then filled with 3 bar hydrogen gas and heated in oven at 60°C. The reaction was left to proceed for 24 hours, until a purple solution was obtained in the sample vial. After, the vessel was removed from the oven, it was cooled and the gas was released. The nanoparticle solution was washed once in a macrocentrifuge for 15 minutes at 4000 rpm using a 1:1

mixture of toluene:methanol. The particles were redispersed in 2 mL toluene.

5.2.2. Palladium shell growth

In an 11 mL vial, 15.2 mg (0.05 mmol) of palladium acetylacetonate and 120.7 mg (0.5 mmol) of the stabilizing agent hexadecylamine were dissolved in 1 mL of the Au NPs solution. The vessel was fitted with a valve and purged three times with vacuum and 1 bar hydrogen gas. The vessel was then filled with 1 bar hydrogen gas and it was heated at 60°C in oven. After 2 hours the vessel was removed from the oven and cooled to give a brown-black solution. The gas was released and the solution was washed twice in a microcentrifuge for 10 mins at 14000 rpm using a 1:1 mixture of toluene:ethanol. The particles were redispersed in 1 mL toluene and characterized by TEM microscopy (figure 5.1).

5.2.3. Nanoparticles deposition onto carbon black

In a 500 mL Shlenk tube, 950 mg of milled Vulcan XC-72 powder (Cabot Corp.) was stirred in 200 mL of toluene for 2 hours to gain carbon dispersion. 50 mg of Au-Pd core-shell particles were dispersed in 20 mL toluene and added drop-wise (1 drop per second ca.) to the stirring solution of carbon powder over 30 minutes, in order to obtain a theoretical 5 wt.% metal (Pd+Au) loading. The resulting mixture was stirred for 20 hours. The powder was separated via filtration under inert atmosphere and dried under vacuum for 24 hours. The resulting catalyst was characterized by TEM imaging (figure 5.3). An ICP-MS analysis stated the real metal loading on the carbon: 4.87 wt.% (2.46 wt.% Pd and 2.40 wt.% Au).

5.3. Morphological characterization

The catalyst morphological characterization by transmission electron microscopy consists in two steps: the preliminary characterization of the fresh synthetized nanoparticles, to investigate their shape and dimensional dispersion, and the characterization of the nanoparticles supported on carbon black, to understand if the NPs deposit homogeneously onto the support and if they modify their shape and dimensions.

Finally, the catalyst morphological characterization was completed with X-ray powder diffraction experiments.

5.3.1. Transmission electron micrscopy

TEM images of the Au@Pd nanoparticles are reported in figure 5.1; in particular it is evidenced the (111) plane of the Pd fcc surface (figure 5.1-B). The NPs have icosahedral shape and the mean diameter is 11.1 ± 1.2 nm (figure 5.2).

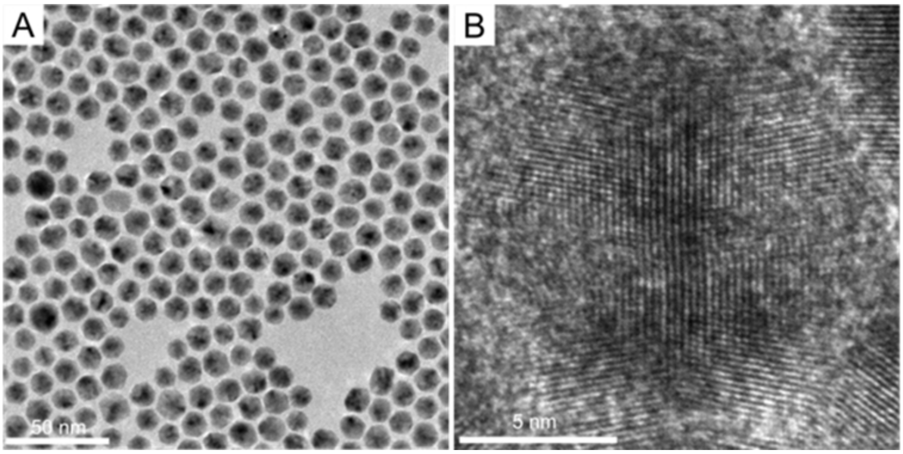

Figure 5.1: TEM images at (A) low magnification (50 nm scale bar) and (B) high magnification (5 nm scale bar) of the Au@Pd nanoparticles suspended in THF.

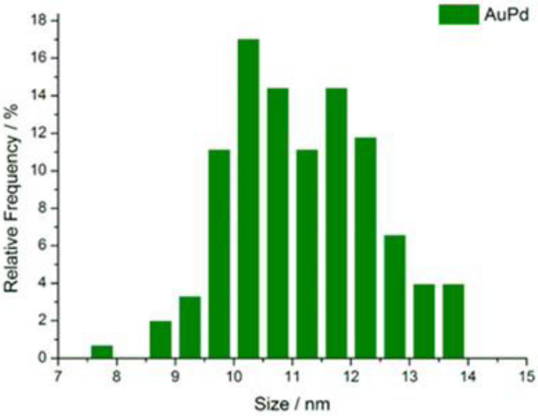

Figure 5.2: HRTEM histograms of particle distribution versus diameter for Au@Pd.

The Au@Pd nanoparticles dispersed onto Vulcan XC-72 are uniformly distributed over the carbon. The NPs maintain their icosahedral shape and composition (figure 5.3).

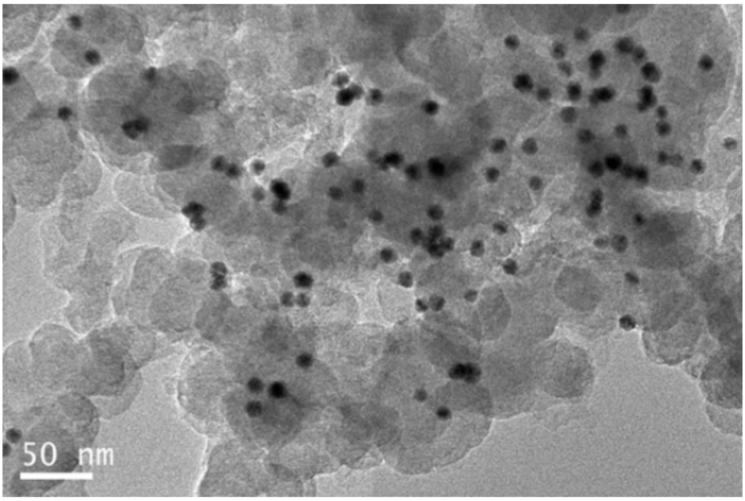

Figure 5.3: TEM image of Au@Pd nanoparticles supported onto carbon black Vulcan XC-72. (Scale bar: 50 nm).

5.3.1.1. X-ray powder diffraction analysis

The catalyst XRPD patterns (figure 5.4) show the typical diffraction peaks of gold and palladium face centered cubic structure. The signals have a low intensity due to the low metal loading onto the carbon support. The peaks at 2θ = 40°, 46° and 68° are the reflections of the (111), (200) and (220) planes of the palladium fcc. These signals are partially overlapped to the diffraction peaks of the (111), (200) and (220) planes of the Au fcc structure, that respectively fall at 2θ = 38°, 45°, and 65° [157]. The broad diffraction peaks at 2θ = 25°, 44° and 80° are the signals of the (002), (010) and (110) planes of the graphitic carbon support [101]. The diffraction peak at 2θ = 80° masks the reflections of the Au (311) and (222) planes and of the Pd (311) plane, that respectively should fall at 2θ = 78°, 82° and 82° [157].

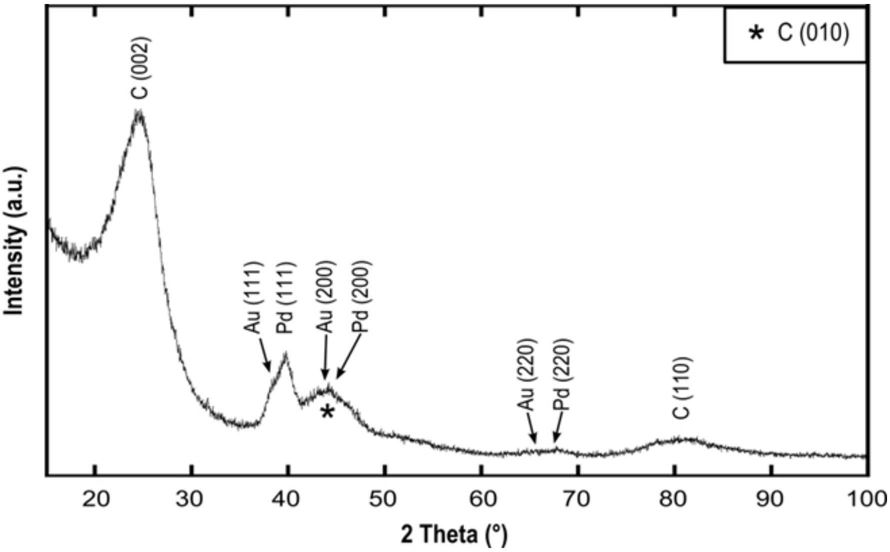

Figure 5.4: XRPD pattern of Au@Pd/C.

5.4. Electrochemical characterization

First, the catalyst was characterized by half-cell measurements, in particular by cyclic voltammetry performed in 2M KOH buffer solution and in 2M alcohol, 2M KOH aqueous solutions (see chapter 7, paragraph 7.6 for the experimental details). Subsequently, the catalyst electrooxidative activity was tested in a complete electroreformer cell, fed with 30 mL of 2M alcohol 2 M KOH aqueous solutions. The procedure for the realization of the MEAs and for the assembly of the electroreforming cell are described in chapter 7, paragraph 7.7.

5.4.1. Cyclic voltammetries in alkaline media

According with the literature, gold is not electrochemically active in the 0-1.4 V vs RHE range, so, at these potentials, the electrochemical reactions occur on the Pd shell [155,157]. In fact, the Au@Pd/C voltammetries in 2M KOH have the typical shape of nanostructured Pd/C catalysts (figure 5.5) [149]. The peak A_1 (0.3-0.45V vs RHE) is related to the hydrogen under potential oxidative desorption. This peak is partially overlapped with A_2 (0.5-0.6 V vs RHE): the signal related with the formation of the $PdOH_{ads}$ species, active for alcohol electrooxidation [55,149]. After this peak, there is an anodic current increase, A_3, due to the $PdOH_{ads}$ species oxidation to PdO_{ads} that passivates the electrocatalyst [55,149]. These palladium oxides are reduced in the backward scan (peak C_1, 0.7 V vs RHE ca.). Hydrogen under potential deposition occurs at 0.2 V vs RHE, peak C_2 [55,149].

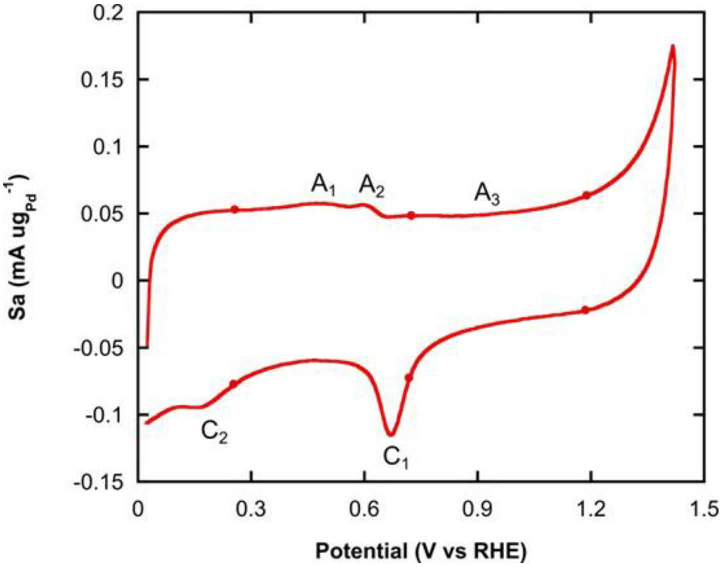

Figure 5.5: Cyclic voltammogram of Au@Pd/C in aqueous 2M KOH. Scan rate: 50 mVs^{-1} at room temperature.

The electrochemically active surface area (EASA) of the Pd shell was evaluated from the integration of the reduction peak of the first monolayer of PdO_{ads} on the NPs surface (peak C_1 in the reverse scan) [149,151]; the EASA was evaluated from the average of five measurements performed on fresh catalyst working electrodes. The Au@Pd/C catalyst has an EASA of 35.42 m^2 g^{-1}_{Pd}, this value is comparable with the results reported in literature for similar Au@Pd/C catalysts (Zhou et al. report a EASA value of 55.8 $m^2 g_{Pd}^{-1}$ [156] and Xiaoyu reported a value of 14.8 $m^2 g_{Pd}^{-1}$ [154]).

On the same catalyst, a set of seven CVs in 2M KOH were executed increasing the inversion potential value of 0.1 V vs RHE for each experiment. Figure 5.6 reports the 0.9-0.4 V vs RHE region of the reverse scan of these CVs. According to the literature, the amount of the PdO_{ads} species generated in the forward scan increases with higher inversion potentials, so the PdO_{ads} reduction peak increases its area and the peak potential shifts from 0.7 V vs RHE to 0.6 V vs RHE [161]. At high inversion potentials, 1.6 and 1.7 V vs RHE, the PdO_{ads} reduction signal splits in two peaks, at 0.8 V vs RHE (C_1'') and 0.6 V vs RHE (C_1') respectively. Birss and co-workers described the peak C_1'' as the reduction of superior Pd oxides obtained at high anodic potentials (V >1.5 V vs RHE) to PdO_{ads} species. The peak C_1' is related to the reduction of PdO_{ads} species to metallic palladium [161].

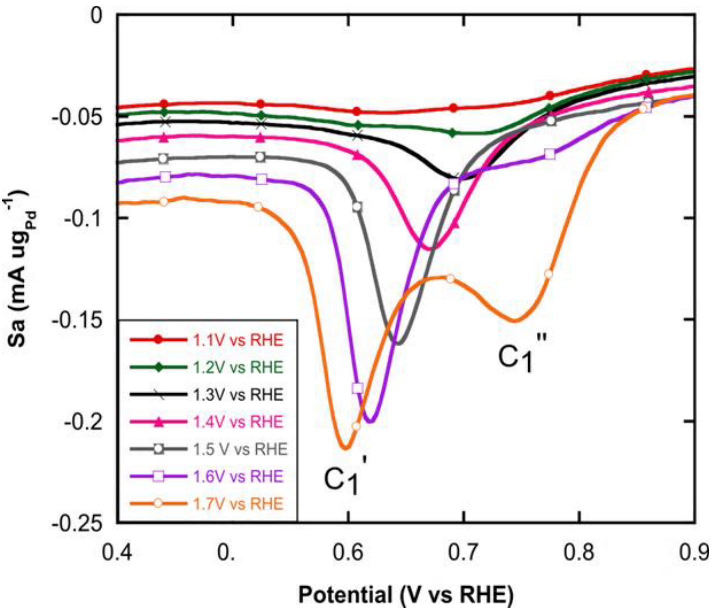

Figure 5.6: Cyclic voltammograms of Au@Pd/C in aqueous 2M KOH at the inversion potential of 1.1 (●), 1.2 (♦), 1.3 (X), 1.4 (▲), 1.5 (◘), 1.6 (□) and 1.7 (○) V vs RHE. Scan rate: 50 mVs^{-1}.

5.4.2. Cyclic voltammetries in 2M alcohol 2M KOH

The Au@Pd/C catalyst activity was studied by cyclic voltammetry experiments, performed in 2M alcohol (ethanol, ethylene glycol, 1,2-propanediol, 1,3-propanediol, 1,4-butanediol or glycerol) 2M KOH aqueous solution. Since the ethanol oxidation reaction happen on the palladium shell surface, the voltammograms have the typical shape of the CVs reported in the literature for a standard Pd/C catalyst [55]. Half-cell measurements in 2M KOH show that the NPs surface oxidation to palladium oxides occurs at high anodic potentials (figure 5.6) [161]; these species are inactive for alcohol electrooxidation [55]. For this reason, the formation of poisoning PdO species was limited by performing the CVs at low anodic potentials, in the 0-1.2 V vs RHE window. The voltammogram performed in the 2M EtOH 2M KOH (figure 5.7) solution is now analytically described [55]:

- Forward scan.
    - 0.4 V vs RHE is the onset potential for the anodic peak of the alcohol electrooxidation reaction. As investigated in the voltammograms in 2M KOH, at this potential value the Pd nanoparticles are oxidized to $PdOH_{ads}$ species, so it is reasonable to suppose that these palladium hydroxides are the species involved in the alcohol electrooxidation mechanisms.
    - The anodic current reaches the maximum value at 0.7-0.8 V vs RHE, after this, the current decreases due to the formation of PdO_{ads} species, inactive for the electrocatalysis.
    - After 1.0 V vs RHE there is no more catalyst electrooxidative activity due to the saturation of the nanoparticle surface with palladium oxides species.
- Reverse scan.
    - 0.6 V vs RHE is the onset potential for the anodic peak in the reverse scan: at this value the PdO_{ads} species are reduced to the

PdOH$_{ads}$ species, which again oxidize the alcohol adsorbed onto the catalyst.

- This anodic current reaches the maximum value at ca. 0.5 V vs RHE.

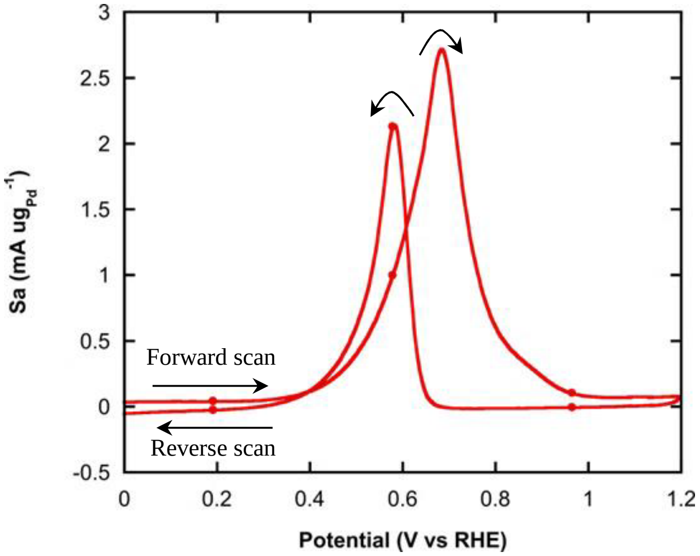

Figure 5.7: Cyclic voltammetry of Au@Pd/C in 2M EtOH 2M KOH. Scan rate: 50 mVs^{-1} at room temperature.

Table 5.1 summarizes the Au@Pd electrooxidative activity in half cell for all the alcohols tested and figure 5.8 describes the onset potential region (between 0.3 and 0.8 V vs RHE) of the direct scan of the CVs. The catalyst easily oxidizes ethanol: the onset potential is 350 mV, about 200 mV lower than the value for the other alcohols but in terms of specific activity, the best catalyst performance was recorded for 1,3-propanediol. The catalyst has a similar electrochemical activity for the oxidation of ethylene glycol and 1,2-propanediol, due to the similar structure of the two molecules.

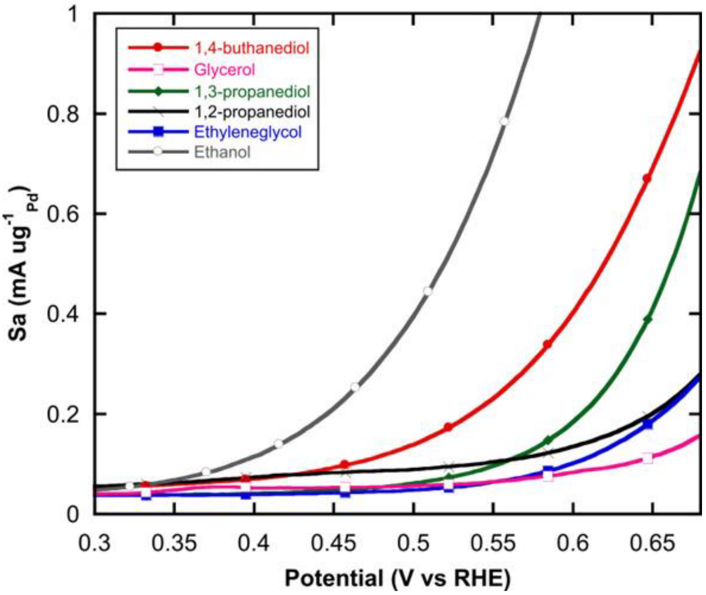

Figure 5.8: Cyclic voltammograms of Au@Pd/C in 2M ethanol (○), 2M ethylene glycol (■), 2M 1,2-propanediol (X), 2M 1,3-propanediol (♦), 2M glycerol (□) and 2M 1,4-butanediol (●) 2M KOH solutions. Scan rate: 50 mVs^{-1} at room temperature.

Table 5.1: Au@Pd/C electrooxidative performances in half cell tests.

Fuel	**E_{onset} (V vs RHE)**	**Sa peak forward scan (mA µg^{-1}$_{Pd}$)**	**E peak forward scan (V vs RHE)**
EtOH	0.35	2.71	0.68
EG	0.55	3.73	0.84
1,2-P	0.55	3.29	0.84
1,3-P	0.50	5.04	0.84
1,4-B	0.45	1.65	0.79
G	0.60	2.09	0.87

5.4.3. Electrochemical-reforming experiments

Tests were run at a cell temperature of 60°C [27]. Figure 5.9 describes the polarization curves in the 0.4 – 0.9 V region of the first catalytic cycle, performed on the electroreformer fed with a 2M aqueous solution of 2M ethanol (EtOH, □), 2M ethylene glycol (EG, ○), 2M 1,2-propanediol (1,2-P, ×), 2M 1,3-propanediol (1,3-P, ♦), 2M 1,4-butanediol (1,4-B, ■) or 2M glycerol (G, ●). Potentiodynamic experiments were performed another two times, before each chronopotentiometric run; all the experiments are reported in figure 5.10 (●, experiment or cycle 1, ■ cycle 2 and ♦ cycle 3). In the potentiodynamic tests, no mass transport limitation can be seen even at the highest current densities and there is no trace of the oxygen evolution reaction in the cell working potential window (0.2-1.0 V). Table 5.2 summarizes the device electrochemical activity, in terms of onset potential values and maximum current densities J (mA cm^{-2}) at 0.9 V. It is important to notice that the current density values of 200-400 mA cm^{-2} were recorded at a potential 1 V lower respect the voltage applied in a traditional PEME or in a traditional alkaline water electrolyzer to obtain the same current densities [27].

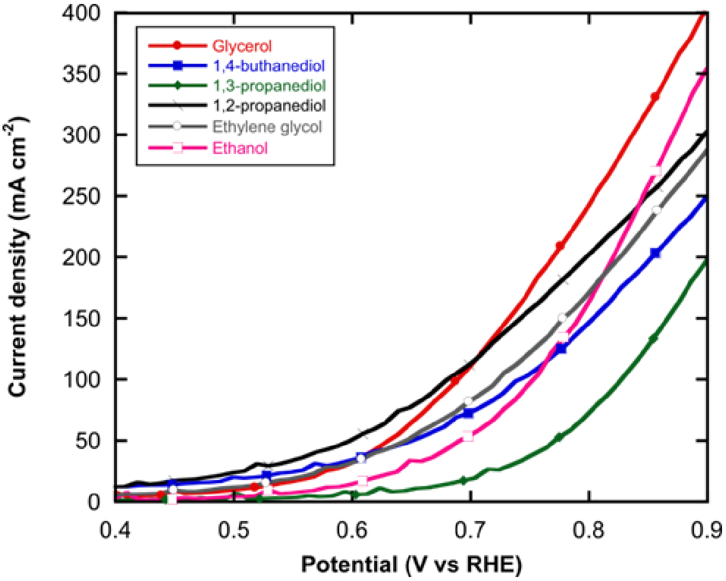

Figure 5.9: Electrochemical reforming of alcohols with Au@Pd/C. Polarization curves for 2M KOH water solutions of : 2M EtOH (□); 2M EG (○); 2M 1,2-P (×); 2M 1,3-P (♦); 2M 1,4-B (■) and 2M G (●). Linear potential ramp, 10 mVs^{-1} scan rate.

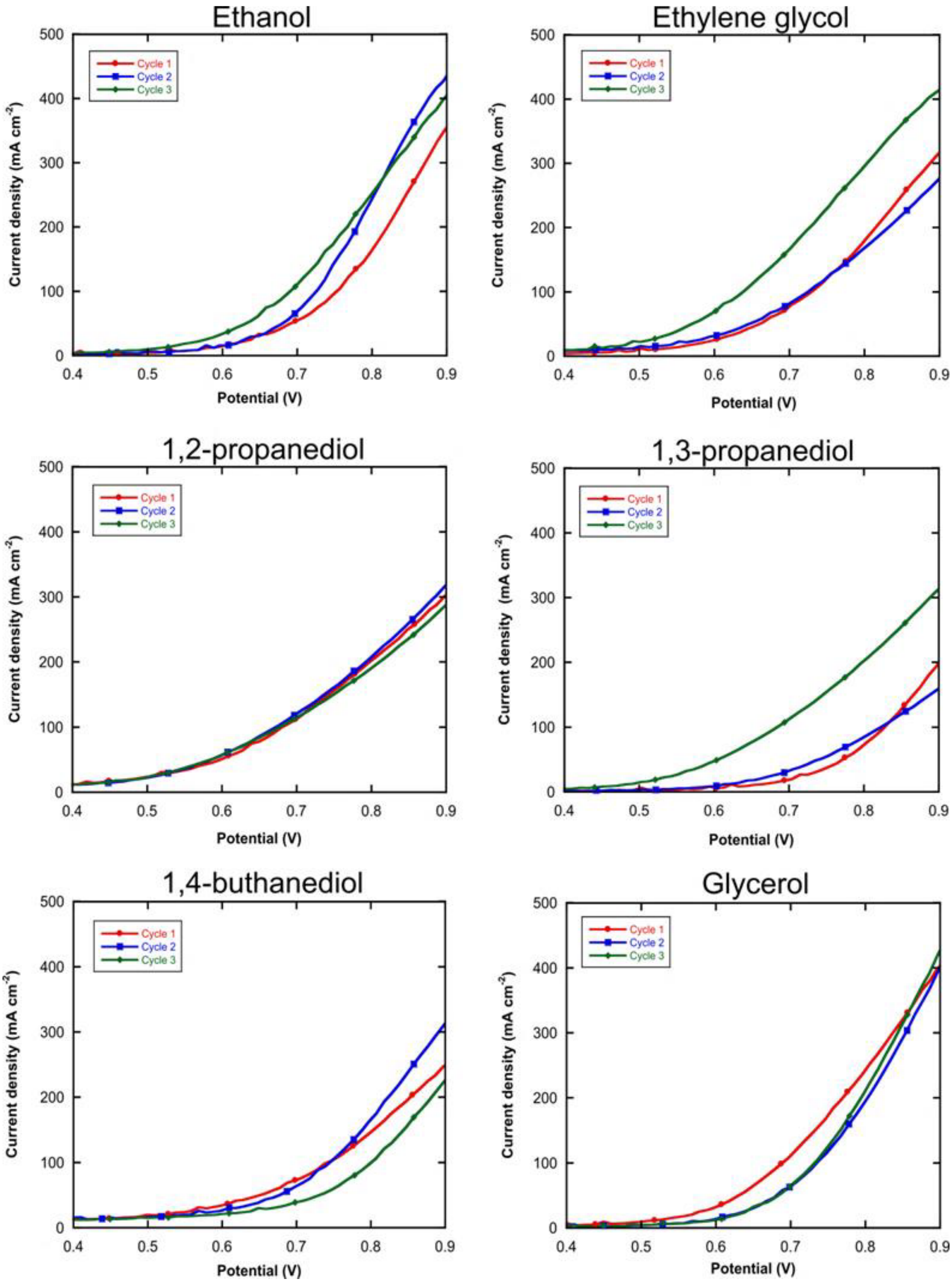

Figure 5.10: Three potentiodynamic cycles of the electroreformer fueled with: 2M EtOH, 2M EG, 2M 1,2-P, 2M 1,3-P, 2M 1,4-B and 2M G aqueous solutions in 2M KOH. ●, cycle1, ♦, cycle 2, ■, cycle 3. Linear potential ramp, 10 mVs^{-1} scan rate; cell temperature: 60°C.

Table 5.2: Electroreformers electrochemical activity in the polarization experiments.

Fuel	Cycle	E_{onset} (V)	J_{max} (mA cm^{-2}) at 0.9 V
EtOH	I	0.55	364.9
	II	0.55	483.7
	III	0.40	482.9
EG	I	0.50	297.4
	II	0.40	391.7
	III	0.40	434.0
1,2-P	I	0.45	310.8
	II	0.45	449.3
	III	0.45	408.7
1,3-P	I	0.65	207.2
	II	0.60	236.7
	III	0.45	421.6
1,4-B	I	0.50	252.8
	II	0.50	423.6
	III	0.65	344.2
G	I	0.50	410.8
	II	0.60	642.5
	III	0.60	650.7

The first set of chronopotentiometric curves (37.5 mA cm^{-2}) are reported in figure 5.11 (EtOH □, EG ○, 1,2-P ×, 1,3-P ♦ 1,4-B ■ or G ●, the duration time was limited at 30 hours). At 800 mV there is a dramatic voltage increase up to the 1.0 V potential cut off value, due to palladium oxidation to inactive species.

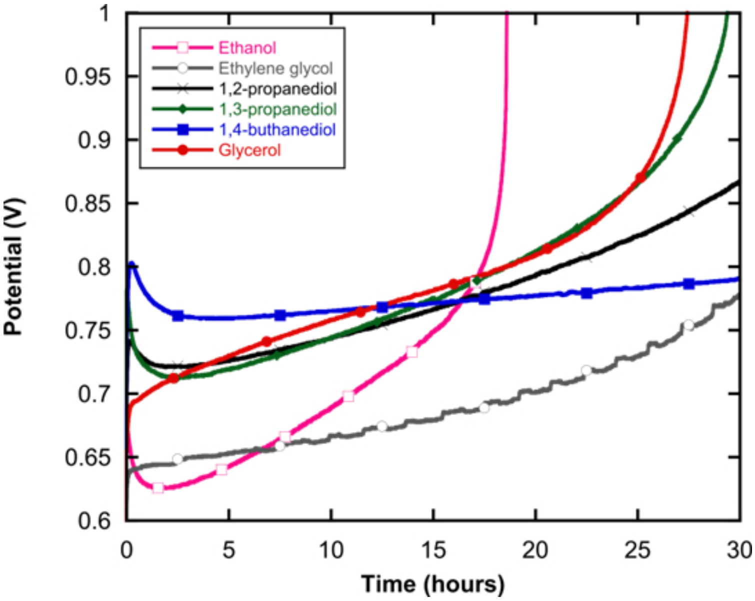

Figure 5.11: Chronopotentiometric curve of the electroreformer fueled with 2M EtOH (□), 2M EG (○), 2M 1,2-P (X), 2M 1,3-P (♦), 2M 1,4-B (■) or 2M G (●) aqueous 2M KOH solutions. Current load of 37.5 mA cm^{-2}.

The data obtained from the three chronopotentiometric experiments are summarized in table 5.3. The cell was washed and fed with fresh fuel before each experiment. The amount of hydrogen evolved was calculated from the moles of the electrons exchanged in the cell, as described in eq. 5.1.

$$mol_{H_2} = \frac{Q}{nF} = \frac{it}{2F} \qquad \textit{Eq. 5.1}$$

Q is the total charge (i*t) exchanged in the cell, expressed in Coulomb; *n* is the number of the electrons involved in the hydrogen evolution reaction and *F* is the Faraday constant.

The energy consumption for each chronopotentiometric experiment was evaluated from the integration of the instantaneous charging power ($V*i^2$) over the experimental duration time. This value, expressed in kWh, is reported per kilogram of H_2 produced. The Au@Pd/C based electroreformer has a mean energy consumption over all the tests of 20 kWh $kg_{H_2}^{-1}$ (table 5.3), a result in line with the energy consumption of the best alkaline alcohol electroreformer reported in literature [27].

The electroreformers fed with EtOH, EG, 1,2-P, 1,4-B and G generally increase their activity passing from the first to the second set of experiments: both in the polarization and chronopotentiometric curves there is a lowering of the onset potential. In addition, there is an increase of the chronopotentiometric duration time and of the maximum current density exchanged in the cell during the potentiodynamic experiment. The device fed with 1,3-P, on the contrary, shows a small activity drop passing from the first to the following catalytic cycles.

Table 5.3: Electrochemical activity from chronopotentiometric experiments.

Fuel	Cycle	Duration time	Conversion (%) (mmol products)	Hydrogen (mmol)	Energy (kWh kg $_{H_2}^{-1}$)
EtOH	I	18h:36m	43% (26.0)	52.0	18.64
	II	18h:56m	44% (26.5)	53.0	19.43
	III	19h:22m	45% (27.1)	54.2	19.79
EG	I	35h:19m	75% (45.2)	99.0	19.10
	II	37h:20m	75% (47.8)	104.5	18.01
	III	38h:07m	81% (49.0)	107	18.62
1,2-P	I	36h:15m	82% (48.4)	101.6	21.39
	II	37h:01m	77% (46.3)	103.5	21.62
	III	35h:13m	74% (44.2)	99.0	21.43
1,3-P	I	29h:20m	52% (31.0)	82.2	21.13
	II	26h:58m	47% (28.4)	75.7	22.01
	III	26h:47m	49% (29.2)	77.9	21.78
1,4-B	I	59h:03m	98% (58.8)	165.4	21.52
	II	60h:31m	99% (59.3)	169.6	21.97
	III	61h:11m	99% (59.7)	174.2	22.15
G	I	27h:27m	44% (26.6)	76.7	21.00
	II	30h:44m	50% (29.9)	86.2	20.20
	III	30h:11m	49% (29.4)	84.6	20.11

5.5. Investigation on catalyst stability

High resolution TEM was performed on the Au@Pd/C catalysts recovered from the cell fed with 1,2-propanediol after testing (figure 5.12 and figure 5.13-A). There is a marked aggregation of nanoparticles in small aggregates throughout the samples after use. This phenomena is typical of the nanoparticles deposited onto carbon based supports [162,163].

Figure 5.13-B shows a high magnification micrograph of one Au@Pd nanoparticle, which appears crystalline, showing epitaxial growth of Pd onto the Au core; gold appears darker due to a higher electron density. The fast Fourier transform (FFT) of the selected area shows spots which can be assigned to (1-11), (-111) and (002) reflections; indicating face-centred cubic crystal structure of Pd viewed down a ⟨110⟩ zone axis. The Dark-Field TEM (DF) of a single core-shell particle (figure 5.13-C) confirms that the particles maintain their Au core-Pd shell morphology (gold appears brighter in this imaging mode due to the higher density).

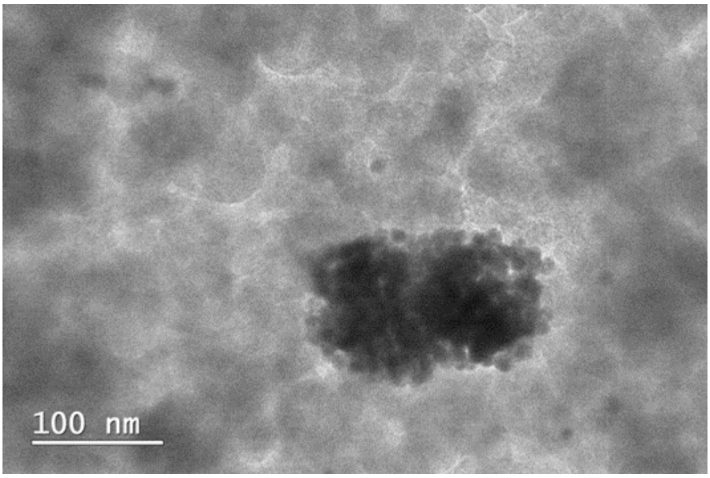

Figure 5.12: HR-TEM image of catalyst after electroreforming experiments. Clustering of Gold-Palladium particles on carbon is evidenced.

STEM-EDX maps were obtained to investigate how the electrochemical oxidation of alcohols influences the nanoparticle morphology. Figure 5.13 D and E show respectively the exact elemental composition of gold and palladium within the formed bimetallic nanoparticle. Figure 5.13-F shows the overlay of the two EDAX maps. At the gold-palladium interface, there seems to take place alloy formation because the gold signal rather fades out rather than possessing sharp borders. This is likely to be due to mediation of strain arising from a lattice mismatch of 4.08% [164]. The gold core seems to remain unchanged and spherical, while the palladium shell appears elongated indicating dissolution or migration of palladium from the particle surface.

Figure 5.14 shows a comparison of the XRPD patterns of the fresh catalyst (b) and of the catalyst (a) recovered after three catalytic cycles with 1,2-propandiol. The XRPD patterns do not show any structural change in the catalyst recovered after its employment in the cell. In fact, the two diffraction patterns (a) and (b) are perfectly superimposable and show the typical reflections of the planes (111), (200) and (220) of Pd fcc, which respectively fall at 2θ = 40°, 46° and 68°. These signals are partially overlapped to the diffraction peaks of the (111), (200) and (220) planes of the Au fcc structure at 2θ = 38°, 45°, and 65° [157]. The reflection at 2θ = 17° in the pattern (a) is attributed to the PTFE binder, employed to paste the anodic catalyst powder in the “ink” that was spread onto the nickel conductive support to realize the electrode (as completely described in chapter 7, paragraph 7.7.3.3).

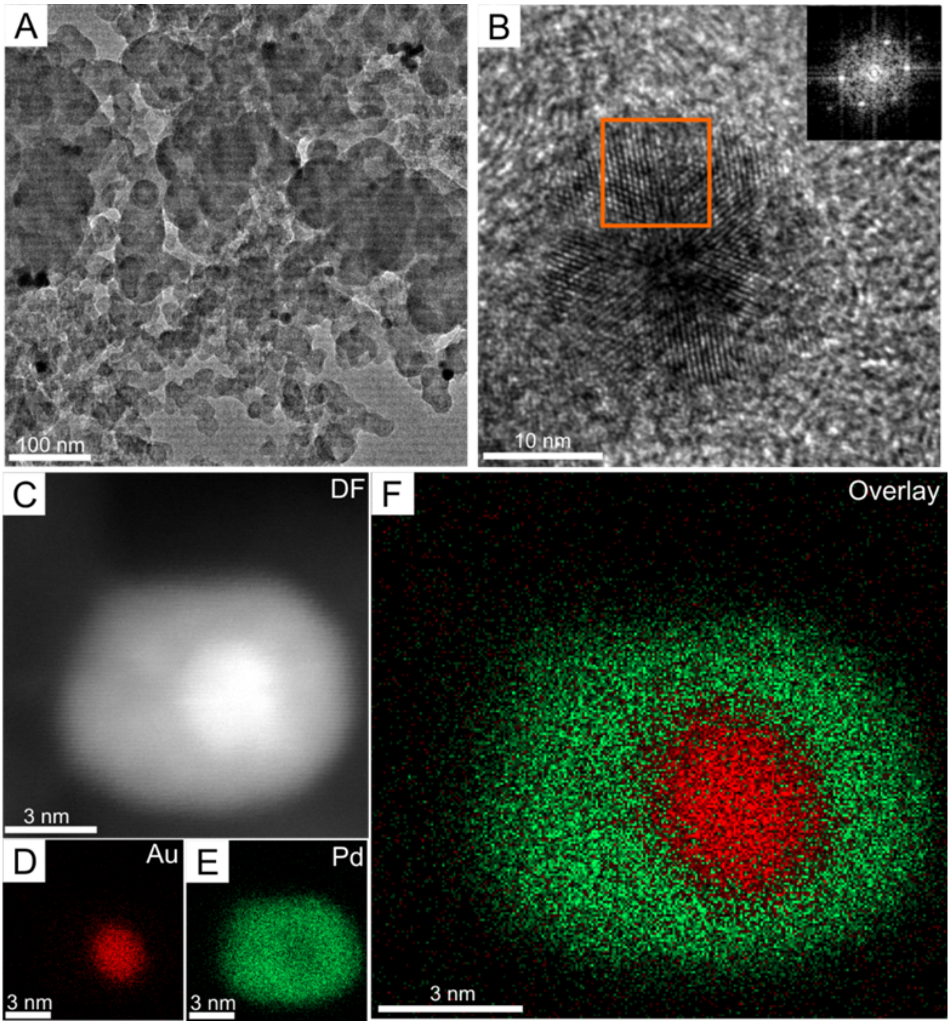

Figure 5.13: (A) Clustering of Gold-Palladium particles on carbon after electrocatalytical reactions. (B) HR- TEM image of Au-Pd particles showing an icosahedral morphology. The insert shows a FFT of the selected area, corresponding to Pd (111) facets viewed along a ⟨110⟩ zone axis. (C) Dark-field TEM image of a single core-shell particle showing a higher contrast for the denser gold core. (D) STEM-EDX map showing the signals corresponding to gold. (E) STEM-EDX map showing the signals corresponding to palladium. (F) STEM-EDX map shown as an overlay of both gold and palladium signals.

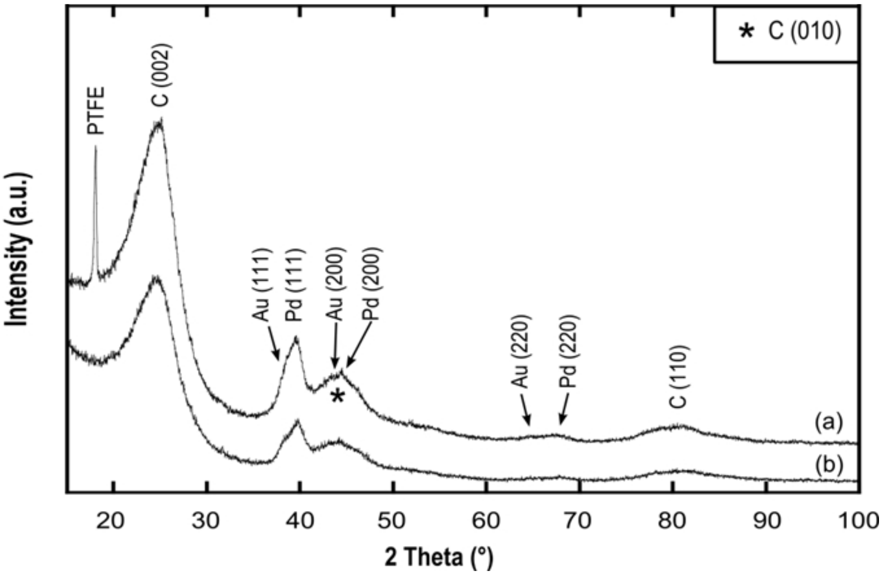

Figure 5.14: X-ray powder diffraction patterns of the exhausts catalyst recovered after three catalytic cycles (a) and of the fresh catalyst (b).

5.6. Selectivity of alcohols electrooxidation

Fuel exhausts were recovered after each chronopotentiometric experiment; they were quantitatively analysed by HPLC liquid chromatography and qualitatively, and semiquantitavely characterized by ^{1}H and ^{13}C NMR spectroscopy. Table 5.4 summarizes this data, that were compared with the results obtained from the best alcohol electroreformer reported in literature, which employs a Pd/TNTA (Titania Nanotube Arrays) anodic electrocatalyst [27].

Both Au@Pd/C and Pd/TNTA have the typical behaviour of Pd based electrocatalysts: ethanol electrooxidation is 100% selective towards acetate. On the contrary, the core-shell system has an ameliorative effect in the selective oxidation of the diols EG and 1,2-P: glycolate was obtained with a 86 % selectivity and lactate with a 87% selectivity, while the Pd/TNTA has respectively 33% and 80% selectivity towards these carboxylic compounds.

Concerning 1,3-propanediol and the 1,4-butanediol there are no data in literature available for a direct comparison. As reported for the OMFCs in chapter 3, paragraph 3.4, the longer aliphatic chain of these molecules, allow the further oxidation of the monocarboxylic compound to the bicarboxylic compound: about 35% of malonate and the 18% of succinate were obtained from the oxidation of 1,3-P and 1,4-B respectively. No significant selectivity change was observed in the second and in the third chronopotentiometric experiments for each alcohol.

Table 5.4:Selectivity of the alcohols electrooxidation reactions performed in the electroreformer equipped with the Au@Pd/C anode and in the electroreformer reported in literature, which employs a Pd/TNTA anode.

Fuel	Au@Pd/C	Pd/TNTA[27]
EtOH	100% acetate	100% acetate
EG	86% glycolate 9% oxalate 2% formate 3% carbonate	33% glycolate 37% oxalate 26% carbonate 4% formate
1,2-P	87% lactate 5% acetate 8% carbonate	80% lactate 10% acetate 5% carbonate 5% formate
1,3-P	56% 3-hydroxy-propanate 35% malonate 3% formate 6% carbonate	/
1,4-B	82% 4-hydroxy-butanoate 18% succinate Carbonate and formate in trace	/
G	48% glycerate 26% tartronate 7% glycolate 4% oxalate 6% formate 9% carbonate	55% glycerate 25% tartronate 10% carbonate 10% formate

5.7. Final overview

Alkaline alcohol electroreformers provide a net energy saving for hydrogen production compared to traditional water electrolysis. In addition, hydrogen production is coupled with the contemporaneous conversion of a bioalcohol into valuable chemicals, for example lactate and glycolate, which are industrially relevant feedstock. Traditional nanostructured palladium based anodic electrocatalysts are not selective in the oxidation of renewable polyols to carboxylic compounds. Modifying the nanoparticle architecture is a way to increase this selectivity.

Icosahedral Au@Pd nanoparticles with a mean diameter of 11 nm were supported on carbon black Vulcan XC-72 to obtain an anodic electrocatalyst for alcohol electroreforming. This catalyst is able to oxidize 1,2-propanediol and ethylene glycol with high selectivity towards lactate (87%) and glycolate (80%) respectively, with a net increase in the oxidation reaction selectivity compared to the values obtained with traditional palladium nanostructured anodic electrocatalysts (80% of lactate and 33% of glycolate). In addition, the energy consumption for hydrogen production by electrolysis was lowered from 50-60 kWh $kg_{H_2}^{-1}$ to ca. 20 kWh $kg_{H_2}^{-1}$.

6. Conclusions

Innovative anodic electrocatalysts for energy-related applications are developed and described in this thesis. In particular, three catalysts were prepared, morphologically and electrochemically characterized and successfully employed as anodes in three devices: a) Organometallic fuel cells; b) H_2/O_2 Platinum Free anion exchange membrane fuel cells and c) alkaline membrane electroreformer.

Direct alcohol fuel cells (DAFCs) are the only devices where the free energy of an alcohol can be converted into electrical energy with contemporaneous release of higher added-value products. A crucial role for achieving this goal is played by the anode electrocatalyst that must promote the partial oxidation of the alcohols to carboxylic compounds, preferentially in a selective way and with fast kinetics. This paradigmatic piece of chemical sustainability has been attempted for many years, with limited success and no practical application. Such a target can be achieved for a variety of renewable alcohols such as ethanol, glycerol and ethylene glycol by means of innovative direct fuel cells, operating in an alkaline environment. In such devices, the most important role is played by the anode electrocatalyst where alcohol oxidation occurs.

Chapter 3 discusses OrganoMetallic Fuel Cells (OMFC). For the first time an organometallic complex has been employed as anode electrocatalyst in a direct fuel cell. This development is a breakthrough in fuel cell technology and, in general, in electrocatalysis for a number of reasons. From a practical perspective, a molecular metal complex, soluble in different solvents and hence easily dispersible on very small surfaces, but capable of delivering high power densities upon oxidation of alcohols, paves the way to the further miniaturization of fuel cells. Indeed, the established methods of organometallic synthesis leading to well-defined molecular metal complexes offer enormous advantages in the rational design and optimization of fuel cell catalysts, including a reduced metal loading due to the fact that all metal sites are active (unlike catalysts based on metal nanoparticles). In this chapter, the molecular complex $Rh[(trop_2NH)PPh_3]OTf$ supported onto carbon black (KtjBk) was successfully employed as anode in a direct alcohol fuel cell. The device allows the selective oxidation of renewable polyols such as ethylene glycol and 1,2-propanediol to 100% of glycolate and lactate respectively (both at room temperature and 80°C). Longer chain alcohols 1,3-propanediol and 1,4-buthanediol were oxidized at 80°C to 96% of 3-hydroxypropanate and 4% of malonate and to 74% of 4-hydroxypropanate and 26% of succinate respectively.

Fuel cells are the best devices for converting the chemical energy of hydrogen cleanly into electricity on demand with the only byproducts water and heat. State of the art low temperature proton exchange membrane fuel cells (PEM-FCs) are compact systems with high power densities, which make them ideal for automotive applications. Recent analyses have shown that among PEM-FC components around 45% of the cost comes from the platinum electrocatalysts. Therefore, a complete removal of platinum in fuel cell stacks and replacement with metals that are less expensive and more abundant in nature is crucial to make this technology an affordable solution for automotive as well as other large scale applications.

As an alternative to PEM-FCs, that work under highly corrosive acidic conditions and require high loadings of Pt catalysts, the alkaline anion exchange membrane fuel cell (AEM-FC) has been proposed as a solution to reduce costs by avoiding the use of platinum.

In Chapter 4 a nanoparticle Pd anode catalyst with a composite Vulcan XC-72 carbon-CeO_2 support is shown to exhibit enhanced kinetics for the HOR in alkaline media. The mixed CeO_2-carbon support was prepared by depositing 50 wt.% CeO_2 onto Vulcan XC-72 carbon. The desired amount of Pd (10 wt.%) was deposited by the addition of a $Pd^{(II)}$ precursor to a suspension of this support under aqueous alkaline conditions followed by reduction with ethanol at 80 °C.

The Pd/C:CeO_2 catalyst and a reference Pd/C catalyst were incorporated into anodic catalyst layers. Membrane electrode assemblies (MEAs) were prepared for testing in AEM-FC single cells, employing the obtained anodic catalyst together with a FeCo/C cathodic catalyst and anion exchange membrane and ionomer.

The AEM-FC that employs Pd/C:CeO_2 exhibits enhanced power output. The ameliorative effect is due to a Pd/C:CeO_2 interaction through a combination of weakening of Pd-H binding and OH_{ads} spillover from CeO_2. AEM-FC tests show peak power densities of more than 200 mW cm^{-2}. This is a milestone achievement that will stimulate new research in AEM-FCs. This performance is achieved using partially filtered ambient air (<10ppm CO_2) (cathode), and dry hydrogen (anode), making this technology suitable for multiple applications.

Chapter 5 describes the development of an alternative to traditional water electrolyzers for hydrogen production. This device called alkaline membrane alcohol electroreformer replaces the oxygen evolution reaction with alcohol oxidation at the anode, thus reducing significantly the energy cost of hydrogen evolution. A membrane-electrode assembly (MEA) for this device was developed consisting of a Au@Pd/C core-shell nanoparticles supported onto carbon black (C) anode, a commercial (E-Tek) Pt/C cathode and an anion-exchange membrane (Tokuyama® A-201).

The device was fed with small aliphatic renewable alcohols: ethanol (EtOH), ethylene glycol (EG), 1,2-propanediol (1,2-P), 1,3-propanediol (1,3-P), 1,4-butanediol (1,4-B) and glycerol (G). The Au@Pd/C catalyst is shown to have an high selectivity for ethylene glycol and 1,2-propanediol oxidation to glycolate (86%) and lactate (87%) respectively. The energy consumption of about 20 kWh $kg_{H_2}^{-1}$ is in line with the best electroreformers yet reported in the literature, providing a net energy saving for hydrogen production compared to traditional water electrolysis.

In conclusion, this thesis demonstrates that a suitable architecture of the anodic electrocatalysts have a crucial role in the development of DAFCs, AMFCs and alkaline alcohol electroreformers, in terms of electrochemical performance, cost reduction by removal of precious metals and selectivity for the oxidation of renewable alcohols to industrially relevant feedstocks.

7. Experimental section

7.1. Electron microscopy

Catalysts morphology was studied using transmission electron microscopy (TEM). TEM micrographs were also used to calculate the mean nanoparticle sizes. For some catalysts, the morphological characterization was performed with high resolution transmission electron microscopy (HR-TEM) and scanning transmission electron microscopy (STEM).

7.1.1. Transmission electron microscopy

Standard catalyst morphological characterization was performed by transmission electron microscopy (TEM), with a Philips CM12 microscope at an accelerating voltage of 100 kV. The microscope was equipped with an EDAX energy dispersive microanalysis system.

7.1.2. High resolution transmission electron microscopy and scanning transmission electron microscopy

HR-TEM images and scanning transmission electron micrographs (STEM) were recorded with a Zeiss Libra 200 FE transmission electron microscope equipped with a double tilt goniometer at 200 kV and an EDAX microanalysis system.

The microscope was equipped with an in column-omega filter spectrometer to obtain elemental mapping by Electron Spectroscopic Imaging (ESI). A three-window method was used.

ESI images of the Pd/C:CeO_2 catalyst described in Chapter 4 were obtained filtering electrons by their energy at proper EEL (Electron Energy Loss) edges. Cerium was energy filtered at the N45-edge, C at K-edge and Pd at M45-edge

7.2. X-ray powder diffraction

X-ray powder diffraction (XRPD) measurements were acquired at room temperature with a PANalytical X'PERT PRO diffractometer, employing Cu Kα radiation (λ = 1.54187 Å) and a parabolic MPD-mirror. The diffraction patterns were acquired at room temperature in the 2θ range from 5.0 to 120.0°, using a continuous scan mode with an acquisition step size of 0.0263° and a counting time of 49.5 s.

7.3. X-rays absorption spectroscopy

X-ray Absorption Spectroscopy (XAS) measurements were carried out at the GILDA-CRG beamline of the European Synchrotron Radiation Facility (ESRF, Grenoble, France). Both Extended X-ray Absorption Fine Structure (EXAFS) and X-rays Absorption Near Edge Structure (XANES) experiments were performed.

The monochromator was equipped with a pair of Si (311) crystals and was run in dynamical focusing mode. Harmonic rejection was achieved by using two Pt-coated mirrors with cutoff energy of 32 keV. Data were collected in fluorescence mode using an energy-resolving High Purity Germanium detector array containing 12 elements. A Pd reference foil was measured at the same time as the samples in order to obtain an internal standard for the energy calibration.

Extended X-ray Absorption Fine Structure (EXAFS) data were extracted from the raw absorption coefficient spectrum with the ATHENA code. Data were analyzed in the k-range, k = [2.8–13.5] $Å^{-1}$, and, after Fourier transformation, in the R interval, R = [0.8–6] Å.

7.4. Chemisorption

Catalyst metal active surface area was determined by a CO chemisorption method [165], adapted to carbon supported materials. Experiments were performed at 70 °C by the use of an ASAP 2020C Instrument (Micromeritics Corp.). Before the measurements, the samples were reduced at 210 °C with H_2 and treated in vacuum at the same temperature for 15 hours.

7.5. Inductively coupled plasma

Catalyst metal loading was measured by Inductively Coupled Plasma Mass Spectrometry (ICP-MS). A quadrupole ELAN DRC-e spectrometer was used (PerkinElmer SCIEX, Concord, Ontario, Canada). Each sample (50 mg) was treated in a microwave heated digestion bomb in sealed PTFE vessels with concentrated HNO_3 (2.0 mL) and 98% H_2SO_4 (2 mL). The heating program comprised some preheating steps and a final 10 min digestion step at 220°C. The resulting residual solutions were diluted with water to constant volume. The solutions were then analyzed for the metal content.

7.6. Hal cell experiments

Half-cell electrochemical measurements were performed with a Princeton 2273A potentiostat/galvanostat, using a three-electrode arrangement with a platinum foil (25mm x 25mm x 0.1mm) counter electrode (CE) and a Princeton Applied Research $Ag/AgCl_{sat}$ reference electrode (RE) at the potential of +197 mV vs RHE. The working electrode (WE) is a glassy carbon rotating disk electrode (RDE) of 0.1963 cm^{-2} geometric area (Pine). The glassy carbon is embedded in a Teflon® jacket and it is coated with the catalyst by dropping a catalyst suspension, named “ink”. Steady state measurements were performed with the 616 Rotating Disk Electrode (PAR/Ametek) apparatus.

All the solutions used in half cell characterization techniques were prepared with Millipore water (18 MΩcm) provided by a Milli-Q labo apparatus (Nihon Millipore Ltd.). The chemicals and the solvents were used as purchased (Sigma-Aldrich, ACS purity grade). Solutions were degassed by bubbling high-purity N_2 for 60 minutes before measurements.

All electrical potentials are referred to the Reversible Hydrogen Electrode (RHE) and no iR compensation was applied to the measurements. The measured currents are reported as current density J (mA cm^{-2}) or as specific activity Sa (mA $\mu g_{\text{active phase}}^{-1}$)

7.6.1. Catalyst Ink preparation

Catalyst “inks” were prepared in a 5 mL high-density polyethylene vial mixing 22 mg of the catalyst with 1.2 g of milli-Q water, 0.7 g of iso-propanol and 3.2 mg of the Tokuyama AS-4® (OH^-) ionomer (5 wt.% in iso-propanol). The mixture was suspended by one hour of ultrasound treatment at 59 Hz, 100% power (Branson 3200 ultrasonic bath). A suitable ink amount was dropped onto the glassy carbon electrode (GCE) until the 22-27 μg_{metal} cm^{-2} loading was obtained; the deposit was dried at the air before the use.

7.6.2. Cyclic voltammetries for alcohol electrooxidation

Cyclic voltammetry was performed in 2M KOH aqueous solution, in order to understand the catalyst behavior in the working potential range. Then the voltammograms were carried out in a 2M KOH – 2M alcohol (ethanol or ethylene glycol, 1,2-propanediol, 1,3-propanediol, 1,4-butanediol or glycerol) solutions, in order to understand the catalyst electrochemical activity towards the oxidation of these alcohols. The alcohols and KOH concentrations are 2M because this is the best fuel formulation for the complete cells: it keeps constant the solution conductibility and the OH^- ion concentration (pH = 13); in addition the 2M alcohol concentration minimizes the cross-over phenomena in the complete cell [141]. The voltammograms were recorded with a 50 mV s^{-1} scan rate in the 0-1.2 V vs RHE potential window, applying a linear potential ramp.

7.6.3. Electrochemical active surface area

The Electrochemically Active Surface Area (EASA) of Pd was calculated from voltammetric experiments that were performed in the 0-1.4 V vs RHE potential window with a 50 mV s^{-1} scan rate. These experiments were carried out in a 2M aqueous KOH solution at room temperature. The EASA was calculated from the integration of the reduction peak of the first monolayer of PdO_{ads} on the NPs surface (ca. 0.7V vs RHE in the reverse scan) [149].

7.6.4. Polarization experiments for the HOR

Polarization curves were performed in a 0.1 M KOH solution saturated by bubbling H_2 for 30 minutes. The measurements were carried out in steady state regime, rotating the RDE at 1600 rpm and keeping H_2 saturated the solution by continuous hydrogen bubbling. The measurements were performed at 10 mV s^{-1} scan rate in the 0-0.5 V vs RHE potential window, applying a linear potential ramp.

Tafel analysis was used to study the HOR reaction promoted by the Pd/C:CeO_2 and the Pd/C catalysts described in Chapter 4. These plots were obtained from polarization curves performed in 0.1M KOH, saturated with H_2, at 10 mV s^{-1} scan rate at 1600 rpm, applying a linear potential ramp. Tafel diagrams were obtained by correcting the HOR branch of the polarization curves by subtracting the diffusion overpotential and determining the kinetically limited HOR currents.

7.7. Complete electrochemical cells

Electrochemical cell performance was measured with an Arbin BT 2000-5A 4 channels potentiostat-galvanostat with polarization and chronopotentiometric experiments. All the fuels delivered to the cells were prepared with bidistilled water and with chemicals used as purchased (Sigma.Aldrich, ACS purity grade).

7.7.1. Monoplanar passive fuel cells

The passive cell is a Plexiglas® homemade fuel cell with gold plated collector electrodes and a fuel tank that contains 12 mL of fuel. The cell works at room temperature and the cathodic compartment is fed by an air breathing system (figure 7.1). The MEAs were fabricated by mechanically pressing the anode, the Tokuyama A-201 anion exchange membrane and the cathode FeCo/C within the fuel cell hardware (6 Nm torque). Potentiodynamic experiments were recorded at room temperature applying a linear voltage ramp with a 10 mV s^{-1} scan rate. Chronopotentiometries were performed at room temperature, applying a constant current load of 20.4 mA cm^{-2} until the cell potential reaches the zero value.

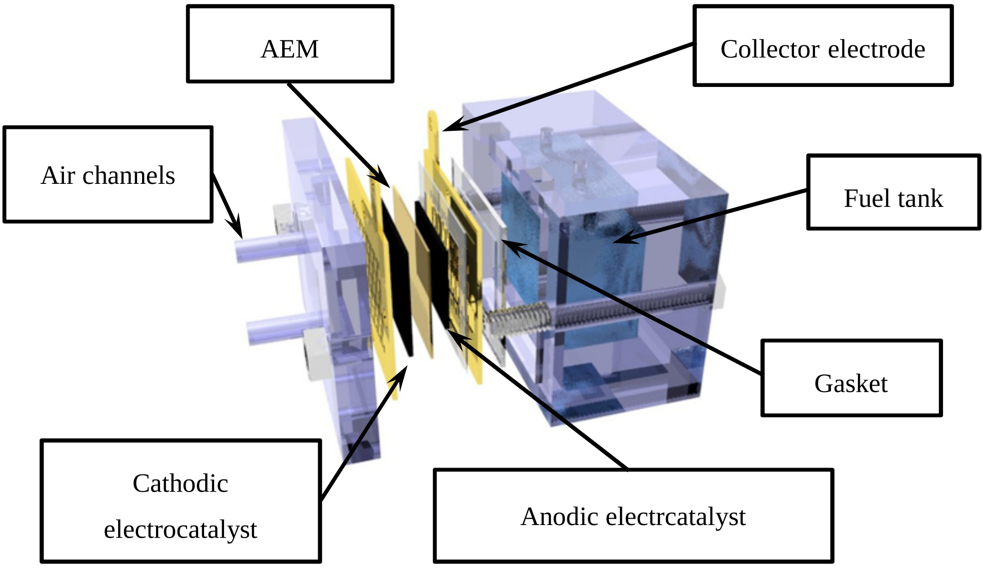

Figure 7.1: Schematic representation of a passive monoplanar cell.

7.7.2. Monoplanar active fuel cells and electroreformers

The active fuel cell system was purchased from Scribner-Associates (USA) and was modified in our laboratory with titanium end plates to tolerate the alkaline conditions (figure 7.2). This system was used also for the electroreforming cell. The MEAs were fabricated by mechanically pressing the anode, the Tokuyama A-201 anion exchange membrane and the cathode within the cell hardware (6 Nm torque). The Scribner 850c or 850e fuel cell test station was used to control the cell temperature and to control the eventual H_2 and O_2 humidification, temperature and flux to the anodic and the cathodic compartments of the cell.

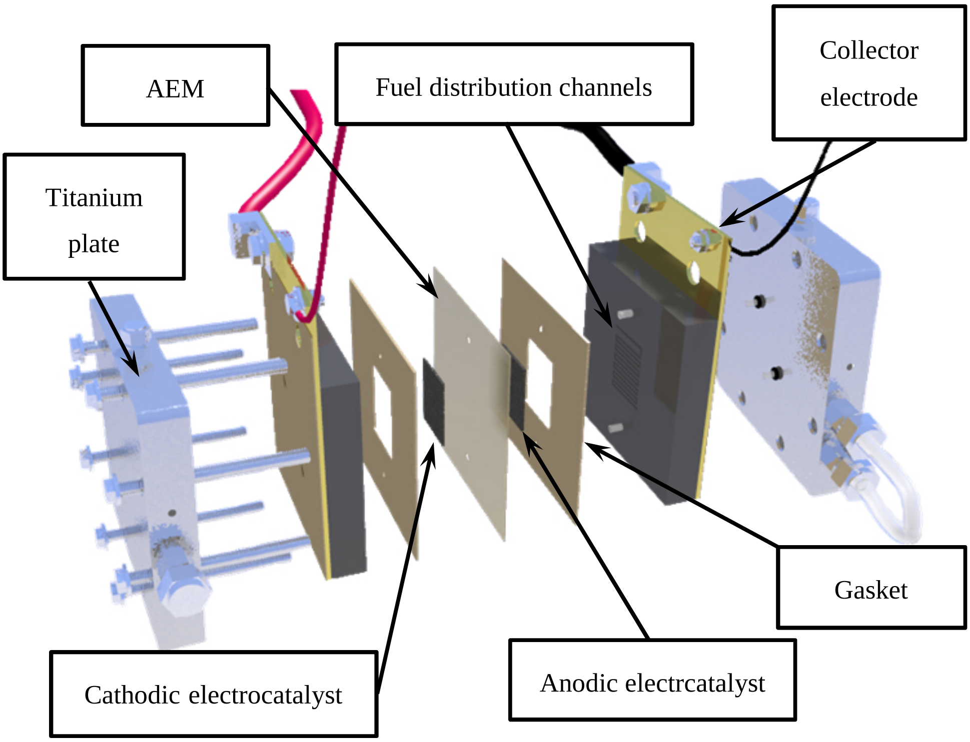

Figure 7.2: Schematic representation of the Scribner Associates cell.

7.7.2.1. Organometallic fuel cells

The anodic compartment of the cell was fed with 30 mL of a 2M alcohol (60 mmol) 2M aqueous KOH fuel, which was delivered with a 7 mL min^{-1} flux by a micro-pump (Gilson Minipulse). The fuel was recirculated to the cell. The cathode was fed with an oxygen flow of 0.1 L min^{-1} (figure 7.3). The temperature of the cell and the oxygen humidification was set at 25°C for low temperature tests and at 80 and 60°C respectively for the high temperature experiments. Potentiodynamic experiments were recorded at 25 and 80°C and were obtained applying a linear voltage ramp with a

10 mV s^{-1} scan rate. Chronopotentiometries were performed at 80°C, applying a constant current load of 20.4 mA cm^{-2} until the cell potential reached the zero value.

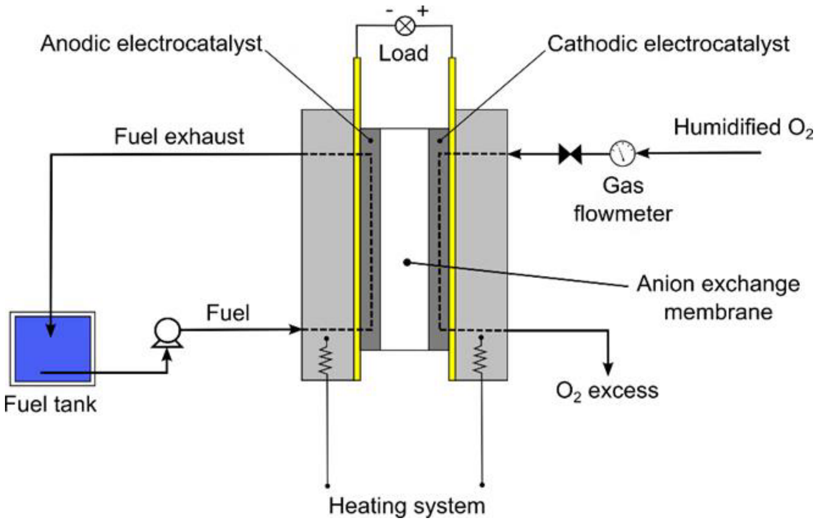

Figure 7.3: Active monoplanar OMFC experimental set-up.

7.7.2.2. Alkaline H_2/O_2 fed fuel cells

The anode was fed with pure humidified hydrogen, with a 0.1 L min^{-1} flux; humidified pure oxygen was delivered to the cathode with a 0.2 L min^{-1} flux. A back-pressure module was used to set the H_2 and O_2 pressure in the cell at 2 atm. The fuel cell was heated to 55°C and the gases were humidified (50°C).

Before assembly of the cell, the membrane was washed in distilled water prior to use. The assembled cell was activated, applying a constant current load of 500 mA for one hour, in order to saturate the membrane with the OH^- anions, reaching the working pH of 13-14 inside the MEA.

The Scribner 850e potentiostat was used to record the polarization and power density curves: a linear current ramp was applied with a 25 mA s^{-1} scan rate from OCV to 0.1 V. In order to have approximate information of the FC stability the polarization experiments were repeated ten times in sequence.

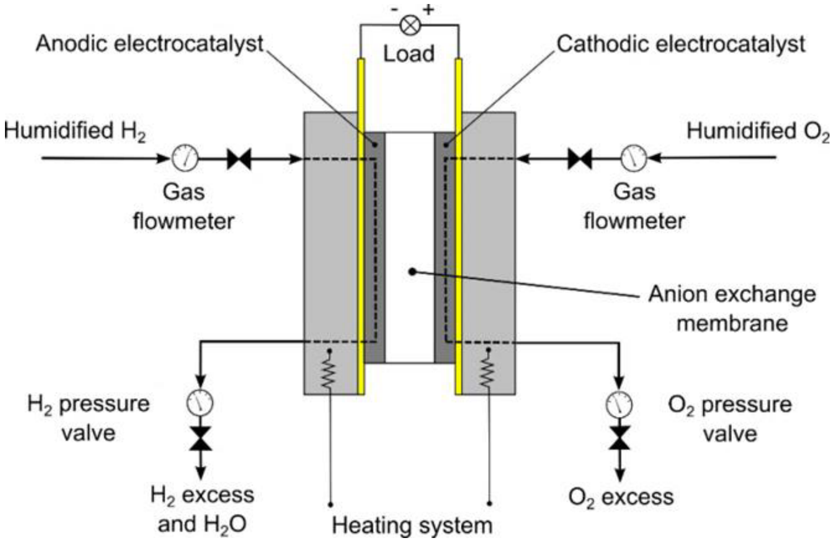

Figure 7.4: Schematic representation of the fuel cell test system.

7.7.2.3. Electroreformer

The anodic side used the same set-up as the active OMFC: the anode is fed with a fuel flux of 4 mL min^{-1}. The reservoir contained 30 mL of 2M alcohol (60 mmol) in 2M aqueous KOH solution. The cathode is supplied with water for the hydrogen evolution reaction by permeation through the membrane from the anodic side (figure 7.5). The electroreformer performance was tested by running both potentiodynamic and galvanostatic curves. Polarization experiments were recorded at 60°C and were obtained applying a linear voltage ramp with a 10 mV s^{-1} scan rate between 0.2 to 1.0 V. Chronopotentiometry experiments were performed at 60°C, applying a constant current load of 37.5 mA cm^{-2} until the cell voltage reached the value of 1.0V.

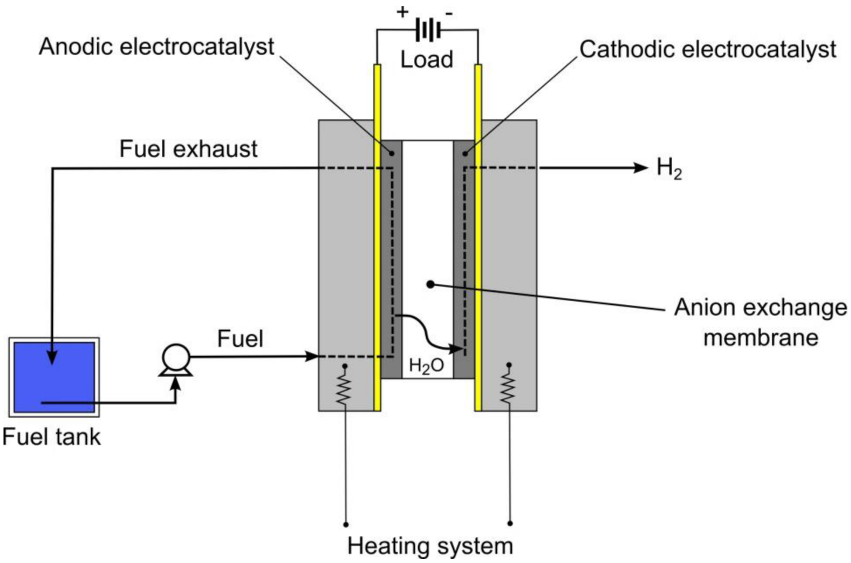

Figure 7.5: Schematic representation of the electroreformer test system.

7.7.3. Membranes Electrode Assembly

All the chemicals and solvents were used as purchased (Sigma-Aldrich).

7.7.3.1. OMFCs

The anodes for both active and passive cells were obtained preparing a dense paste ink by mixing 110 mg of the powdered catalyst with few drops of distilled water and 50 mg of a 10 wt% aqueous dispersion of PTFE (dry electrode content 10 wt.% PTFE). The catalyst paste was applied uniformly to a porous nickel foam support of 5 cm^2 geometric area (110 PPI HZTYKJ from Heze Tianyu Technology Development Co); the final Rh loading onto the electrode is 0.7-1.0 mg$_{Rh}$ cm^{-2}.

The cathode electrode (5 cm^2) was fabricated brushing an ink of the proprietary FeCo/C catalyst onto a carbon cloth W1S1005 (CeTech Co. Ltd.), in order to obtain a 2 mg cm^{-2} catalyst loading [71]. The ink was prepared by mixing in ethanol the required amount of FeCo/C with an aqueous dispersion of PTFE (10 wt% in distilled water). The ink was suspended by sonication (1 hour at 59 Hz and 100% power in a Branson 3200 unltrasonic bath). After drying under air, the cathode was sintered by heating to 340 °C for 20 minutes under a flow of argon. (Dry electrode content 10 wt.% PTFE).

7.7.3.2. AMFCs

The anodic and the cathodic electrodes (5 cm^{-2}) were obtained by spreading with a Meyer rod (table 7.1) an ink of the catalytic powder onto carbon cloth W1S1005 (CeTech Co. Ltd.). The inks were prepared in a 5 mL high density polyethylene vial, mixing the catalytic powder with bidistilled water,1-propanol and the ionomer AS-4® (Tokuyama corp, 5 wt.% in 2-propanol). The amounts of the reactants used are reported in table 7.1. The mixture was suspended with three pulses of ultrasound, 20 W power at the frequency of 20 kHz (Bandelin Sonor pulse UW 2200 SERIES).

Table 7.1: reactants employed in the inks formulation.

Catalys	catalytic powder (mg)	water (mg)	1-propanol (mg)	Ionomer (mg)	meyer rod (µm)	metal loading (mg_{metal} cm^{-2})
Pt/C	100	180	680	240	150	0.44
Pd/C	100	270	710	720	350	0.30
Pd/ C:CeO_2	200	270	610	720	200	0.30
FeCo/C	100	0	1190	1190	300	0.10

7.7.3.3. Electroreformer

The Au@Pd/C anode was obtained preparing a dens paste ink by mixing the 40 mg of the powdered catalyst (23.4 μmol_{Pd} and 23.4 μmol_{Au}) with few drops of distilled water and 50 mg of aqueous 10 wt.% dispersion of PTFE. The catalyst paste was applied uniformly to a porous nickel foam support of 4 cm^2 geometric area (110 PPI HZTYKJ from Heze Tianyu Technology Development Co). The Au@Pd/C electrode metal loading is about 0.25 mg_{Pd} cm^{-2}. (Dry electrode content 10 wt.% PTFE).

The cathode electrode was fabricated spreading the cathodic ink with a Meyer rod (150 µm) onto the carbon cloth W1S1005 (CeTech Co. Ltd.) gas diffusion layer, in order to obtain a 0.4 mg cm^{-2} platinum loading. The deposit was dried under air.

The cathodic ink was prepared in a 5 mL high density polyethylene vial, mixing 200 mg (0.41 mmol) of the commercial Pt (40 wt.%) /C (E-Tek) in 450 mg of distilled water, 790 mg of 1-propanol and 1.56 g of the ionomer Nafion® (5 wt.% in 2-propanol). The mixture was suspended with three pulses of ultrasound, 20 W power at the frequency of 20 kHz (Bandelin Sonor pulse UW 2200 SERIES).

7.7.4. Recovery of used catalysts

The MEAs after testing were disassembled from the cell and the anodic electrocatalyst was recovered and washed with water until neutrality and dried under vacuum at room temperature.

7.8. High performance liquid chromatography

The quantitative analysis of the exhausts recovered from the cells was performed by HPLC. A UFLC Shimadzu Cromatograph equipped with refraction index detector (RID) was used; the column is a GRACE-Alltech OA-1000 Organic Acids (300mm x 6.5 mm), thermostated at 35°C. The eluent is 0.01 N H_2SO_4; and the eluent flow is 0.8 mL min^{-1}. Fuel exhausts (5 mL) were acidified with a H_2SO_4 1M solution to constant volume (15 mL).

7.9. Nuclear magnetic resonance spectroscopy

^{1}H, ^{13}C and ^{31}P-NMR spectra were acquired with a with a Bruker Avance DRX 400 spectrometer. Chemical shifts (δ) are reported in ppm relative to TMS (^{1}H and ^{13}C NMR spectra) or 85% H_3PO_4. Deuterated solvents (Sigma-Aldrich) used for NMR measurements were dried with activated molecular sieves.

8. References

[1] O. C. Onar, *Alternative Energy in Power Electronics*, Elsevier Inc., **2015**.

[2] G. Dutton, M. Page, *Prospect. Electr. Transp. Fuels to 2050* **2008**, 347–370.

[3] A. Lavacchi, H. Miller, F. Vizza, *Nanotechnology in Electrocatalysis for Energy*, **2013**.

[4] I. Dincer, C. Zamfirescu, *Adv. Power Gener. Syst.* **2014**, 369–453.

[5] R. L. Orbach, *Energy Production: A Global Perspective*, Elsevier Ltd., **2012**.

[6] P. Breeze, *An Introduction to Electricity*, Elsevier Ltd., **2014**.

[7] U. Bardi, *Energy Policy* **2005**, *33*, 53–61.

[8] C. Karakosta, H. Doukas, J. Psarras, *Renew. Sustain. Energy Rev.* **2010**, *14*, 1546–1557.

[9] H. Lund, *Energy* **2006**, *31*, 1989–1996.

[10] C. J. Campbell, J. H. Laherrere, *Sceintific Am.* **1998**, 60–65.

[11] L. Chester, *Energy Policy* **2010**, *38*, 887–895.

[12] A. Cherp, J. Jewell, *Energy Policy* **2014**, *75*, 415–421.

[13] I. Dincer, *Energy Policy* **1999**, *27*, 845–854.

[14] Y. H. Cheng, H. P. Chang, C. J. Hsieh, *Atmos. Environ.* **2011**, *45*, 2034–2042.

[15] R. Korhonen, I. Savolainen, *Environ. Sci. Policy* **1999**, *2*, 381–388.

[16] J. Corfee, M. Noreen Beg, O. Davidson, Y. Afrane-Okesse, F. Denton, L. Tyani, Y. Sokona, J. P. Thomas, *Clim. Policy* **2002**, *2*, 1873–1884.

[17] G. Boyle, B. Everett, J. Ramage, *Energy Systems and Sustainability. Power for a Sustainable Future.*, Oxford University Press, **2003**.

[18] R. U. Ayres, H. Turton, T. Casten, *Energy* **2007**, *32*, 634–648.

[19] C. Bright, L. Starke, G. Gardner, *State of the world* **2003**, 85–109.

[20] Z. Glasnovic, J. Margeta, *Renew. Sustain. Energy Rev.* **2011**, *15*, 1873–1884.

[21] J. O. M. Bockris, *Int. J. Hydrogen Energy* **2002**, *27*, 731–740.

[22] M. G. Walter, E. L. Warren, J. R. McKone, S. W. Boettcher, Q. Mi, E. A. Santori, N. S. Lewis, *Chem. Rev.* **2010**, *110*, 6446–6473.

[23] S. Sharma, S. Krishna, *Renew. Sustain. Energy Rev.* **2015**, *43*, 1151–1158.

[24] H. Ito, T. Maeda, A. Nakano, H. Takenaka, *Int. J. Hydrogen Energy* **2011**, *36*, 10527–10540.

[25] U. B. Demirci, P. Miele, *J. Clean. Prod.* **2013**, *52*, 1–10.

[26] R. S. Cherry, *Int. J. Hydrog. Econ.* **2004**, *29*, 125–129.

[27] Y. X. Chen, a Lavacchi, H. a Miller, M. Bevilacqua, J. Filippi, M. Innocenti, a Marchionni, W. Oberhauser, L. Wang, F. Vizza, *Nat. Commun.* **2014**, *5*, 4036.

[28] T. Smolinka, E. T. Ojong, *Hydrogen Production from Renewable Energies - Electrolyzer Technologies* **2015**, 103–128.

[29] F. Mueller-Langer, E. Tzimas, M. Kaltschmitt, S. Peteves, *Int. J. Hydrogen Energy* **2007**, *32*, 3797–3810.

[30] F. Barbir, *PEM Fuel Cells*, Elsevier B.V, **2005**.

[31] Verdantix, *The Future of Energy Management*, **2012**.

[32] C. J. Cleveland, C. Morris, *Handbook of Energy: Volume II*, Elsevier B.V, **2014**.

[33] D. Pimentel, *Encycl. Phys. Sci. Technol.* **2001**, 159–171.

[34] P. McKendry, *Bioresour. Technol.* **2002**, *83*, 37–46.

[35] N. B. Board, *Bioenergy*, Elsevier Inc., **2015**.

[36] S. Tojo, T. Hirasawa, T. Chosa, T. Matsumoto, M. Iwaoka, *Research Approaches to Sustainable Biomass Systems*, Elsevier, **2014**.

[37] R. Chen, T. S. Zao, *Fuel Cells - Direct Alcohol Fuel Cells - Experimental System*, Elsevier Inc., **2009**.

[38] K. L. Kadam, J. D. McMillan, *Bioresour. Technol.* **2003**, *88*, 17–25.

[39] M. R. L. V Leal, M. V. Galdos, F. V. Scarpare, J. E. a Seabra, A. Walter, C. O. F. Oliveira, *Biomass and Bioenergy* **2013**, *53*, 11–19.

[40] C. M. Hoffmann, *Sugar Tech.* **2010**, *12*, 276–287.

[41] Y. Sun, J. Cheng, *Bioresour. Technol.* **2002**, *83*, 1–11.

[42] M. Simões, S. Baranton, C. Coutanceau, *ChemSusChem* **2012**, *5*, 2106–2124.

[43] M. K. Heun, M. de Wit, *Energy Policy* **2012**, *40*, 147.

[44] D. Pimentel, T. W. Patzek, *Nat. Resour. Res.* **2005**, *14*, 65.

[45] V. S. Bagotsky, *Fuel Cells, Problems and Solutions*, **2009**.

[46] G. Hoogers, *Fuel Cell Technology Handbook*, CRC Press, **2003**.

[47] Y. X. Chen, Nanostructured TiO2 Based Materials for Electrocatalysis and Photoelectrocatalysis, PhD Thesis, Università degli Studi di Trieste, **2013.**

[48] W. Associates, G. Weaver, *World Fuel Cells. An Industry Profile with Market Prospects to 2010*, Elsevier Inc., **2002**.

[49] M. M. Mench, *Fuel Cells Engines*, Whiley, **2008**.

[50] E. T. Service, Ed. , *Fuel Cell Handbook*, **2004**.

[51] S. M. Haile, *Acta Mater.* **2003**, *51*, 5981–6000.

[52] S. W. Cha, R. O'hayre, W. Colella, F. B. Prinz, *Fuel Cells Fundamentals*, Wiley, **2006**.

[53] P. K. Shen, C. Bianchini, *Chem. Rev.* **2009**, *109*, 4183.

[54] M. Bevilacqua, V. Bamabagioni, C. Bianchini, J. Filippi, A. Marchionni, F. Vizza, P. K. Shen, L. Wang, *Fuel Cells* **2009**, *10*, 2203–2208.

[55] T. S. Zhao, Z. X. Liang, J. B. Xu, L. D. Zhu, *Electrochim. Acta* **2009**, *10*, 582–590.

[56] L. O. Vasquez, *Fuel Cells Research Trends,* **2007**.

[57] S. P. Annen, V. Bambagioni, M. Bevilacqua, J. Filippi, A. Marchionni, W. Oberhauser, H. Schönberg, F. Vizza, C. Bianchini, H. Grützmacher, *Angew. Chemie - Int. Ed.* **2010**, *49*, 7229–7233.

[58] V. Bambagioni, C. Bianchini, Y. Chen, J. Filippi, P. Fornasiero, M. Innocenti, A. Lavacchi, A. Marchionni, W. Oberhauser, F. Vizza, **2012**, 1266–1273.

[59] Y. Chen, M. Bellini, M. Bevilacqua, P. Fornasiero, A. Lavacchi, H. A. Miller, L. Wang, F. Vizza, *ChemSusChem* **2015**, *8*, 524–533.

[60] Y.J. Wang, J. Qiao, R. Baker, J. Zhang, *Chem Soc Rev* **2013**, *42*, 5768.

[61] T. Fujigaya, C. Kim, K. Matsumoto, N. Nakashima, *ChemplusChem* **2014**, *79*, 400–405.

[62] S. F. Lu, J. Pan, B. Huang, L. Zhuang, J. T. Lu, *Proc. Natl. Acad. Sci. U. S. A.* **2008**, *105*, 20611–20614.

[63] Y. S. Li, T. S. Zhao, Z. X. Liang, *J. Power Sources* **2009**, *187,* 387–392.

[64] J. Xu, P. Gao, T. S. Zhao, *Energy Environ. Sci.* **2012**, *5*, 5333.

[65] X. Wang, J. P. McClure, P. S. Fedkiw, *Electrochim. Acta* **2012**, *79*, 126–132.

[66] D. Dekel, *Encyclopedia of Applied Electrochemistry*, Springer New York, **2014**.

[67] J. Lee, B. Ocon, J. D. Jeong, *Curr. Appl. Phy.* **2013**, *13*.

[68] R. Othman, A. L. Zhu, H. Z. Dicks, *Int. J. Hydrog. Energ* **2012**, *37*, 357–372.

[69] J. S. Guo, J. Zhou, D. Chu, R. R. Chen, *J. Phys. Chem. C* **2013**, *117*, 4006–4017.

[70] L. Ding, Q. Xin, X. J. Zhou, J. L. Qiao, H. Li, H. J. Wang, *J. Appl. Electrochem.* **2013**, *43*, 43–51.

[71] V. Bambagioni, C. Bianchini, J. Filippi, A. Lavacchi, W. Oberhauser, A. Marchionni, S. Moneti, F. Vizza, R. Psaro, V. D. Santo, et al., *J. Power Sources* **2011**, *196*, 2519–2529.

[72] H. A. Miller, M. Bevilacqua, J. Filippi, A. Lavacchi, A. Marchionni, M. Marelli, S. Moneti, W. Oberhauser, E. Vesselli, M. Innocenti, et al., *J. Mater. Chem. A* **2013**, *1*, 13337–13347.

[73] Z. Yang, H. G. Nie, X. Chen, X. H. C. Hua, S. M. Huang, *J. Power Sources* **2013**, *236*, 238–249.

[74] K. P. Gong, F. Du, Z. H. Xia, M. Durstock, L. M. Dai, *Science.* **2009**, *323*, 760–764.

[75] J. Ohyama, T. Sato, A. Satsum, *J. Power Sources* **2013**, *225*, 311–315.

[76] D. J. Ham, C. Pak, G. H. Bae, S. Han, K. Kwon, S. A. Jin, H. Chang, S. H. Choi, J. S. Lee, *ChemComm.* **2011**, *47*, 5792–5794.

[77] K. Kwon, S. A. Jin, K. H. Lee, D. J. You, C. Pak, *Catal. Today* **2014**, *232*, 175–178.

[78] S. Izhar, M. Nagai, *J. Power Sources* **2008**, *182*, 52–60.

[79] J. Durst, A. Siebel, C. Simon, F. Hasche, J. Herranz, H. A. Gasteiger, *Energy Environ. Sci.* **2014**, *7*, 2255–2260.

[80] Q. P. Hu, G. W. Li, J. Pan, L. S. Tan, J. T. Lu, L. Zhuang, *Int. J. Hydrogen Energy* **2013**, *38*, 16264–16268.

[81] V. Bambagioni, M. Bevilacqua, J. Filippi, A. Marchionni, S. Moneti, F. Vizza, C. Bianchini, *Chimica Oggi-Chemistry Today* **2010**, *28*, 7–10.

[82] C. Bianchini, V. Bambagioni, J. Filippi, A. Marchionni, F. Vizza, P. Bert, A. Tampucci, *Electrochem. commun.* **2009**, *11*, 1077–1080.

[83] M. Bellini, M. Bevilacqua, M. Innocenti, M. Lavacchi, H. A. Miller, J. Filippi, A. Marchionni, W. Oberhauser, L. Wang, F. Vizza, *J. Electrochem. Soc.* **2014**, *161*, D3032–D3043.

[84] “Cativa Process,” can be found under: https://it.wikipedia.org/wiki/Processo_Cativa.

[85] “Monsanto Process,” can be found under: https://it.wikipedia.org/wiki/Processo_Monsanto.

[86] M. Bellini, M. Bevilacqua, J. Filippi, A. Lavacchi, A. Marchionni, H. a. Miller, W. Oberhauser, F. Vizza, S. P. Annen, H. Grützmacher, *ChemSusChem* **2014**, 2432–2435.

[87] G. Squadrito, L. Andaloro, M. Ferraro, V. Antonucci, *Advances in Hydrogen Production, Storage and Distribution*, Woodhead Publishing Limited, **2014**.

[88] T. Smolinka, E. Systems, *Water Electrolysis* **2009**, 394–413.

[89] V. Bambagioni, M. Bevilacqua, C. Bianchini, J. Filippi, A. Lavacchi, A.

Marchionni, F. Vizza, P. K. Shen, *ChemSusChem* **2010**, *3*, 851–855.

[90] P. a. Stuart, T. Unno, J. a. Kilner, S. J. Skinner, *Solid State Ionics* **2008**, *179*, 1120–1124.

[91] P. Millet, *Compendium of Hydrogen Energy*, Elsevier, **2015**.

[92] A. T. Marshall, R. G. Haverkamp, *Int. J. Hydrogen Energy* **2008**, *33*, 4649–4654.

[93] P. Millet, S. Grigoriev, *Renew. Hydrog. Technol. Prod. Purification, Storage, Appl. Saf.* **2013**, 19–41.

[94] S. Marini, P. Salvi, P. Nelli, R. Pesenti, M. Villa, M. Berrettoni, G. Zangari, Y. Kiros, *Electrochim. Acta* **2012**, *82*, 384–391.

[95] G. G. Botte, M. Cooper, *J. Electrochem. Soc.* **2006**, *153*, A1894.

[96] F. Vitse, G. G. Botte, M. Cooper, *J. Power Sources* **2005**, *142*, 18.

[97] S. Uhm, H. Jeon, T. J. Kim, J. Lee, *J. Power Sources* **2012**, *198*, 218–222.

[98] G. Sasikumar, A. Muthumeenal, S. S. Pethaiah, N. Nachiappan, R. Balaji, *Int. J. Hydrogen Energy* **2008**, *33*, 5905–5910.

[99] Y. X. Chen, A. Lavacchi, H. a Miller, M. Bevilacqua, J. Filippi, M. Innocenti, A. Marchionni, W. Oberhauser, L. Wang, F. Vizza, *Nat. Commun.* **2014**, *5*, 4036.

[100] S. P. Annen, V. Bambagioni, M. Bevilacqua, J. Filippi, A. Marchionni, W. Oberhauser, H. Schönberg, F. Vizza, C. Bianchini, H. Grützmacher, *Angewandte Chemie - International Edition* **2010**, 7229–7233.

[101] B. F. Machado, A. Marchionni, R. R. Bacsa, M. Bellini, J. Beausoleil, W. Oberhauser, F. Vizza, P. Serp, *J. Energy Chem.* **2013**, *22*, 296–304.

[102] M. Bevilacqua, C. Bianchini, A. Marchionni, J. Filippi, A. Lavacchi, H. Miller, W. Oberhauser, F. Vizza, G. Granozzi, L. Artiglia, et al., *Energy Environ. Sci.* **2012**, *5*, 8608.

[103] K. Elouarzaki, A. Le Gof, M. Holzinger, J. Thery, S. Cosnier, *J. Am. Chem. Soc.* **2012**, *134*, 14078−14085.

[104] K. R. Brownell, C. C. L. McCrory, C. E. D. Chidsey, R. H. Perry, R. N. Zare, R. M. Waymouth, *J. Am. Chem. Soc.* **2013**, *135*, 14299−14305.

[105] S. i. Yamazaki, M. Yao, N. Fujiwara, Z. Siroma, K. Yasuda, T. Ioroi, *ChemComm.* **2012**, *48*, 4353–4355.

[106] M. Trincado, H. Grützmacher, F. Vizza, C. Bianchini, *Chem. - A Eur. J.* **2010**, *16*, 2751–2757.

[107] T. Zweifel, J. V. Naubron, H. Grützmacher, *Angew. Chemie - Int. Ed.* **2009**, *48*, 559–563.

[108] T. Buttner, *RHODIUM A MINE -DIOLEFIN C OMPLEXE*S, Doctarate Thesis, ETH **2004**.

[109] S. P. Annen, *Catalytic Alcohol Dehydrogenations with Rhodium (I) Amino Olefin Complexes Using* O_2 *,* N_2O *and Nitrosoarenes as Hydrogen Acceptors* Doctorate Thesis, ETH **2012**.

[110] T. Zweifel, *Transferhydrogenation with Amino- Olefin Complexes*, Doctorate Thesis, ETH **2008**.

[111] A. Hilmi, E. M. Belgsir, J. M. Léger, C. Lamy, *Journal Electroanal. Chem.* **1995**, *380*, 177–184.

[112] A. Marchionni, M. Bevilacqua, C. Bianchini, Y.-X. Chen, J. Filippi, P. Fornasiero, A. Lavacchi, H. Miller, L. Wang, F. Vizza, *ChemSusChem* **2013**, *6*, 391–399.

[113] K. Elouarzaki, A. Le Gof, M. Holzinger, J. Thery, S. Cosnier, *J. Am. Chem. Soc.* **2012**, *134*, 14078−14085.

[114] T. Matsumoto, K. Kim, S. Ogo, *Angew. Chemie - Int. Ed.* **2011**, *50*, 11202 – 11205.

[115] T. Matsumoto, K. Kim, H. Nakai, T. Hibino, S. Ogo, *ChemCatChem* **2013**, *5*, 1368–1373.

[116] P. Anastas, N. Eghbali, *Chem. Soc. Rev.* **2010**, *39*, 301–312.

[117] M. K. Debe, *Nature* **2012**, *486*, 43–51.

[118] M. Piana, M. Boccia, A. Filpi, E. Flammia, H. a. Miller, M. Orsini, F. Salusti, S. Santiccioli, F. Ciardelli, A. Pucci, *J. Power Sources* **2010**, *195*, 5875–5881.

[119] M. Piana, M. Boccia, A. Filpi, E. Flammia, H. a. Miller, M. Orsini, F. Salusti, S. Santiccioli, F. Ciardelli, A. Pucci, *J. Power Sources* **2010**, *195*, 5875–5881.

[120] M. Mamlouk, J. A. Horsfall, C. Williams, K. Scott, *Int. J. Hydrogen Energy* **2012**, *32*, 11912–11920.

[121] D. Yang, H. Yu, G. Li, Y. Zhao, Y. Liu, C. Zhang, W. Song, Z. Shao, *J. Power Sources* **2014**, *267*, 39–47.

[122] M. Mamlouk, K. Scott, *J. Power Sources* **2012**, *211*, 140–146.

[123] L. Jiang, A. Hsu, D. Chu, R. Chen, *Electrochim. Acta* **2010**, *55*, 4506–4511.

[124] J. S. Guo, J. Zhou, D. Chu, R. R. Chen, *J. Phys. Chem. C* **2013**, *117*, 4006–4017.

[125] M. Lefevre, E. Proietti, F. Jaouen, J. P. Dodelet, *Science* **2009**, *324*, 71–74.

[126] E. Proietti, F. Jaouen, M. Lefevre, N. Larouche, J. Tian, J. Herranz, J. P. Dodele, *Nat. Commun.* **2011**, *2*.

[127] P. Trogadas, T. F. Fuller, P. Strasser, *Carbon N. Y.* **2014**, *75*, 5–42.

[128] Z. Yang, H. G. Nie, X. Chen, X. H. Chen, S. M. Huang, *J. Power Sources* **2013**, *236*, 238–249.

[129] Z. C. Wang, L. Xin, X. S. Zhao, Y. Qiu, Z. Y. Zhang, O. A. Baturina, W. Z. Li, *Renew. Energ.* **2014**, *62*, 556–562.

[130] S. Maheswari, P. Sridhar, S. Pitchumani, *Electrocatalysis* **2012**, *3*, 13–21.

[131] E. Gulzow, N. Wagner, M. Schulze, *Fuel Cells* **2003**, *3*, 67–72.

[132] A. Serov, C. Kwak, *Appl. Catal. B Environ.* **2009**, *90*, 313–320.

[133] J. Zhang, S. H. Tang, L. Y. Liao, W. F. Yu, *Chinese J. Catal.* **2013**, *34*, 1051–1065.

[134] N. Danilovic, R. Subbaraman, D. Strmcnik, A. P. Paulikas, D. Myers, V. R. Stamenkovic, N. M. Markovic, *Electrocatalysis* **2012**, *3*, 221–229.

[135] W. C. Sheng, H. A. Gasteiger, Y. Shao-Horn, *J. Electrochem. Soc.* **2010**, *157*, B1529–B1536.

[136] M. K. Debe, *2009-2011 Annual Merit Reviews DOE Hydrogen and Fuel Cells and Vehicle Technologies Programs: Advanced Cathode Catalysts and Supports for PEM Fuel Cells* **2011**.

[137] N. I. Andersen, A. Serov, P. Atanassov, *Appl. Catal. B Environ.* **2015**, *163*, 623–627.

[138] D. Strmcnik, M. Uchimura, C. Wang, R. Subbaraman, N. Danilovic, D. van der Vliet, A. P. Paulikas, V. R. Stamenkovic, N. M. Markovic, *Nat. Chem.* **2013**, *5*, 300–306.

[139] T. Skála, F. Šutara, M. Škoda, K. C. Prince, V. Matolín, *J. Phys. Condens. Matter* **2009**, *21*, 055005.

[140] Z. a. Feng, F. El Gabaly, X. Ye, Z.-X. Shen, W. C. Chueh, *Nat. Commun.* **2014**, *5*, 1–9.

[141] V. Bambagioni, C. Bianchini, J. Filippi, W. Oberhauser, A. Marchionni, F. Vizza, R. Psaro, L. Sordelli, M. L. Foresti, M. Innocenti, *ChemSusChem* **2009**, *2*, 99–112.

[142] M. L. Toebes, J. A. van Dillen, Y. P. de Jong, *J. Mol. Catal. A- Chem.* **2001**, *173*, 75–98.

[143] W. J. Shen, Y. Matsumura, *J. Mol. Catal. A- Chem.* **2000**, *153*, 165–168.

[144] M. L. Toebes, J. A. van Dillen, Y. P. de Jong, *J. Mol. Catal. A- Chem.* **2001**, *173*, 75–98.

[145] L. Wang, A. Lavacchi, M. Bellini, F. D'Acapito, F. D. Benedetto, M. Innocenti, H. A. Miller, G. Montegrossi, C. Zafferoni, F. Vizza, *Electrochim. Acta* **2015**, *177*, 100–106.

[146] D. Strmcnik, M. Uchimura, C. Wang, R. Subbaraman, N. Danilovic, D. van der Vliet, A. P. Paulikas, V. R. Stamenkovic, N. M. Markovic, *Nat. Chem.* **2013**, *5*, 300–306.

[147] W. J. Zhou, M. Li, O. L. Ding, S. H. Chan, L. Zhang, Y. H. Xue, *Int. J. Hydrogen Energy* **2014**, *39*, 6433–6442.

[148] M. Suleiman, N. M. Jisrawi, O. Dankert, M. T. Reetz, C. Bahtz, R. Kirchheim, A. Pundt, *J. Alloys Compd.* **2003**, *356*, 644–648.

[149] M. Grden, M. Lukaszewski, G. Jerkiewicz, A. Czerwinski, *Electrochim. Acta* **2008**, *53*, 7583–7598.

[150] W. Sheng, Z. Zhuang, M. Gao, J. Zheng, J. G. Chen, Y. Yan, *Nat. Commun.* **2015**, *6*, 5848.

[151] W. Wang, J. Zhang, S. Yang, B. Ding, X. Song, *ChemSusChem* **2013**, *6*, 1945–1951.

[152] C. Hsu, C. Huang, Y. Hao, F. Liu, *Electrochem. commun.* **2012**, *23*, 133–136.

[153] C. Li, Y. Su, X. Lv, Y. Zuo, X. Yang, Y. Wang, *Sensors Actuators B Chem.* **2012**, *171-172*, 1192–1198.

[154] X. Qiu, Y. Dai, Y. Tang, T. Lu, S. Wei, Y. Chen, *J. Power Sources* **2015**, *278*, 430–435.

[155] H. Wang, Z. Sun, Y. Yang, D. Su, *Nanoscale* **2013**, *5*, 139–142.

[156] W. Zhou, J. Y. Lee, *Electrochem. commun.* **2007**, *9*, 1725–1729.

[157] A. Napoleão, D. Furtunato, E. Segura, J. César, R. Fernando, B. De Souza, P. Hammer, E. Vitório, A. Oliveira, M. Linardi, et al., *Electrochim. Acta* **2013**, *111*, 455–465.

[158] A. M. Henning, J. Watt, P. J. Miedziak, S. Cheong, M. Santonastaso, M. Song, Y. Takeda, A. I. Kirkland, S. H. Taylor, R. D. Tilley, *Angew. Chemie - Int. Ed.* **2013**, *52*, 1477–1480.

[159] S. Cheong, L. Graham, G. L. Brett, A. M. Henning, J. Watt, P. J. Miedziak, M. Song, T. Y.;, S. H. Taylor, R. D. Tilley, *ChemSusChem* **2013**, *6*, 1858–1862.

[160] L. D. Zhu, T. S. Zhao, J. B. Xu, Z. X. Liang, *J. Power Sources* **2009**, *187*, 80–84.

[161] A. J. Zhang, M. Gaur, V. I. Birss, *J. Electroanal. Chem.* **1995**, *389*, 149–159.

[162] Y. J. Wang, D. P. Wilkinson, J. J. Zhang, *Chem Rew* **2011**, *111*, 7625–7651.

[163] Y. Shao-Horn, W. C. Sheng, S. Chen, P. J. Ferreira, E. F. Holby, D. Morgan, *Top Catal.* **2007**, *46285-305*.

[164] F. R. Fan, D. Y. Liu, Y. F. Wu, S. Duan, Z. X. Xie, Z. Y. Jiang, Z. Q. Tian, *J. Am. Chem. Soc.* **2008**, *130*, 6949–6951.

[165] F. D'Acapito, A. Trapanati, S. Torrengo, S. Mobilio, *Not. Neutroni e Luce di Sincrotrone* **2014**, *19*, 14–23.

9. Pubblications during the PhD period

9.1. Pubblications on journals:

L.Q. Wang, A. Lavacchi, **M. Bellini**, F. D'Acapito, F. Di Benedetto, M. Innocenti, H.A. Miller, G. Montegrossi, C. Zafferoni, F. Vizza. *"Deactivation of Palladium Electrocatalysts for Alcohols Oxidation in Basic Electrolytes"*; **Electrochimica Acta**, 177 (2015), p. 100-106.

L.Q. Wang, A. Lavacchi, M. Bevilacqua, **M. Bellini**, P. Fornasiero, J. Filippi, M. Innocenti, A. Marchionni, H.A. Miller, F. Vizza. *"Energy Efficiency of Alkaline Direct Ethanol Fuel Cells Employing Nanostructured Palladium Electrocatalysts"*; **ChemCatChem**, 7 (2015), p. 2214-2221.

Y.X. Chen, **M. Bellini**, M. Bevilacqua, P. Fornasiero, A. Lavacchi, H.A. Miller, L.Q. Wang, F. Vizza, F. *"Direct Alcohol Fuel Cells: Toward the Power Densities of Hydrogen-Fed Proton Exchange Membrane Fuel Cells"*; **ChemSusChem**, 8 (2015), p.524-533.

M. Bellini, M. Bevilacqua, J. Filippi, A. Lavacchi; A. Marchionni, H.A. Miller, W. Oberhauser, F. Vizza, S.P. Annen, H. Grutzmacher. *"Energy and Chemicals from the Selective Electrooxidation of Renewable Diols by Organometallic Fuel Cells"*; **ChemSusChem**, 7 (2014), p. 2432-2435. This article is represented in the ChemSusChem "cover picture" of the volume 7, September 2014.

M. Bellini, M. Bevilacqua, M. Innocenti, A. Lavacchi, H.A. Miller, J. Filippi, A. Marchionni, W. Oberhauser, L. Wang and F. Vizza. *"Energy & Chemicals from Renewable Resources by Electrocatalysis"*; **J. Electrochem. Soc**. 161 (2014), p. D3032-D3043.

B.F. Machado, A. Marchionni, R.R. Bacsa, **M. Bellini**, J. Beausoleil, W. Oberhauser, F. Vizza, P. Serp. *"Synergistic effect between few layer graphene and carbon nanotube supports for palladium catalyzing electrochemical oxidation of alcohols"*; **J.Energy Chemistry**, 22 (2013), p. 296-304.

9.2. Posters and communications to conferences:

Author of the poster: **M. Bellini**, M. Bevilacqua, J. Filippi, A. Lavacchi, A. Marchionni, H.A. Miller, W. Oberhauser, L. Wang, F. Vizza. *"Platinum free electrocatalysts for* H_2/O_2 *Alkaline Membrane Fuel Cells (AMFC)"*; **"Giornate DSCTM 2015"; Cetraro (Italy), October 7-9, 2015**.

Coauthor of the oral communication: F. Vizza, **M. Bellini**, M. Bevilacqua, M. Innocenti, A. Lavacchi, A. Marchionni, H.A. Miller, J. Filippi, L.Q. Wang. *"Energy and chemicals from renewable resources by electrocatalysis"*; **"XXV convegno nazionale della società chimica italiana"; Rende (Italy), September 7-12, 2014.**

Coauthor of the poster:” L. Wang, **M. Bellini**, M. Bevilacqua, J. Filippi, A. Lavacchi, A. Marchionni, H.A. Miller, F. Vizza. “*Understanding palladium Electrocatalyst Deactivation”*; **“65th annual meeting of the International Society of Electrochemistry”; Lausanne (Switzerland), August 31 – September 5, 2014.**

Author of the poster and of the oral communication: **M. Bellini,** M. Bevilacqua, J. Filippi, A. Lavacchi, A. Marchionni, H.A. Miller, W. Oberhauser, F. Vizza, S.P. Annen, H. Grützmacher. *“Selective electro-oxidation of renewable diols in OrganoMetallic Fuel Cells (OMFCs) for both energy and chemicals production”*; **“X Spanish-Italian Symposium of Organic Chemistry – SISOC X”; Florence (Italy), July 17-20, 2014.**

Author of the poster: M. Bellini, M. Bevilacqua, J. Filippi, A. Lavacchi, A. Marchionni, H.A. Miller, W. Oberhauser, L. Wang, F. Vizza. *“Platinum free electrocatalysts for* H_2/O_2 *Alkaline Membrane Fuel Cells (AMFC)”*; **“European technical school on hydrogen and fuel cells”; Retymno (Crete-Greece), June 23-27, 2014.**

Coauthor of the oral communication: **M. Bellini**, M. Bevilacqua, J. Filippi, A. Lavacchi, A. Marchionni, H.A. Miller, W. Oberhauser, F. Vizza. *“Electrochemical Exploitation of Biomass”*; **“2014 Electrochemical Conference on Energy & the Environment – ECEE”; Shanghai (R.P. Cinese), March, 13-16 2014.**

Coauthor of the poster: F. Vizza, **M. Bellini**, M. Bevilacqua, J. Filippi, M. Innocenti, A. Lavacchi, A. Marchionni, H.A. Miller, W. Oberhauser, L. Wang. *"Higly efficienty palladium-based anode electrocatalysts for direct ethylene glycol and glycerol fuel cells"*; **"224th ECS Meeting" San Francisco (California-USA); October 27-November 1, 2013.**

Author of the oral communication: **M. Bellini**, B.F. Machado, A. Marchionni, R.R. Bacsa, J. Beausoleil, W.Oberhauser, F. Vizza, P. Serp. *"Synergistic Effect Between Few Layer Graphene and Carbon Nanotube Supports for Palladium Catalyzing Electrochemical Oxidation of Alcohols"*; **" XXXII convegno interregionale delle sezioni Toscana, Umbria, Marche e Abruzzo della società chimica italiana – TUMA 2013"; Florence (Italy), July 1-2, 2013.**

Coauthor of the oral communication: B.F. Machado, A Marchionni, RR. Bacsa, **M. Bellini**, J. Beausoleil, W. Oberhauser, F. Vizza, P. Serp. *"Palladium supported on graphene, carbon nanotubes and graphene/carbon nanotube composites for the electrochemical oxidation of alcohols in alkaline media"*; **"245th ACS National Meeting – 2013" New Orleans Louisiana (USA)"; April 7-11, 2013.**

Coauthor of the oral communication: B.F. Machado, A. Marchionni, R.R. Bacsa, **M. Bellini**, J. Beausoleuil, W. Oberhauser, F. Vizza, P. Serp. *"Pd decorated few-layer graphene, carbon nanotubes and graphene/carbon nanotubes composites for the electrochemical oxidation of alcohols"*; "**2nd international symposium on chemistry for energy conversion and storage"; Berlin (Germany), January 27-30, 2013.**

Coauthor of the oral communication: P. Serp, B.F. Machado, R.R. Bacsa, **M. Bellini**, A. Marchionni, F. Vizza. *"Pd decorated few-layer graphene for the electrochemical oxidation of alcohols"*; **"CARBOCAT-V"; Bressanone (Italy), June 28-30, 2012.**

Coauthor of the oral communication: B.F. Machado, R.R. Bacsa, J. Beausoleil, V. Tishkova, **M. Bellini**, A. Marchionni, F. Vizza, C.Bianchini, P. Serp. *"Few layer graphene decorated with Pd nanoparticles: synthesis, characterisation and catalytic applications in the electrochemical oxidation of alcohols"*; **"Graphene 2012"; Bruxelles (Belgium), June 10-13, 2012.**

Acknowledgments

Desidero ringraziare l'Istituto di Chimica dei Composti Organometallici (ICCOM) del Consiglio Nazionale delle Ricerche di Firenze, rappresentato dal Dott. Maurizio Peruzzini, nelle cui strutture ho seguito il lungo percorso del dottorato di ricerca che si è concluso con questa tesi. Un doveroso ringraziamento è rivolto anche a tutti i gruppi di ricerca che hanno contribuito alla realizzazione di questo lavoro: il gruppo del Prof. Hansjörg Grützmacher dell'ETH di Zurigo, il gruppo della Prof. Eléna Pastor dell'ULL di San Cristòbal de la Laguna e il gruppo del Dott. Christoph Hasenöehrl della Victoria University di Wellington.

Il più vivo ringraziamento è rivolto al mio tutore, Dott. Francesco Vizza, che mi ha permesso di intraprendere nel suo gruppo scientifico il faticoso ma affascinante percorso del dottorato, seguendomi assiduamente durante tutte le fasi dell'attività di ricerca e di stesura di questa tesi. Il rapporto che si è creato in questi anni va ben oltre la semplice relazione lavorativa e la stima e la gratitudine che nutro nei suoi confronti è più profonda e sincera di quella che si può comunicare attraverso dei ringraziamenti formali. Nutro lo stesso sentimento nei confronti di tutti i membri del gruppo di ricerca, il Dott. Hamish Miller, il Dott. Andrea Marchionni, il Dott. Jonathan Filippi, la Dott.sa Manuela Bevilacqua, il Dott. Werner Oberhauser e il Dott. Alessandro Lavacchi, che mi hanno formato scientificamente durante questi tre anni, insegnandomi a muovermi correttamente in un laboratorio chimico e aiutandomi con la stesura di questa tesi. È impossibile non ringraziare Lianqin Wang, *Maria Folliero, Maria Pagliaro e Jacopo Ruggeri, che sono stati degli ottimi compagni di ufficio in questi tre lunghi, ma al tempo stesso troppo brevi, anni. Infine, è doveroso ringraziare tutti i "ragazzi" dell'ICCOM, in particolare il Dott. Gabriele Manca, la Dott.sa Maria Caporali, il Dott. Lorenzo Zani, il Dott. Andrea Ienco, la Dott.sa Giulia Tuci, il Dott. Samuele Staderini, la Dott.sa Irene Mellone, il Dott. Manuel Serrano, il Dott. Lapo Luconi, il tecnico Carlo Bartoli, i miei compagni di corso di dottorato, Alessio, Vanessa e Fuencisla e i nuovi dottorandi Matteo e Salvatore. Tutte queste persone contribuiscono a rendere ICCOM un posto accogliente e unico.*

Infine un grazie di cuore alla mia famiglia, alla mia ragazza e a tutti i miei amici, quelli storici, quelli del mare e i miei compagni di facoltà che mi hanno supportato e sopportato in questi anni.

I wish to thank the Institute of Chemistry of the Organometallic compounds (ICCOM) and its director Dr. Maurizio Peruzzini: here I experienced a long period of study and research concluded with this thesis. I thank heartily the research groups who contributed to carry out this work: Professor Grützmacher'group (ETH, Zurich), Professor Pastor's group (ULL, San Cristòbal de la Laguna) and Dr. Hasenöehrl's group (Victoria University Wellington).

I want to show my deepest gratitude to my tutor, Dr. Francesco Vizza: he gave me the opportunity to join his research group and to start this long, hard but fascinating doctorate course, following my work of research and giving me precious suggestions for my thesis. During these three years of exciting activity and very nice time I have gained professional experience *and skills that will benefit my career. He deserves all my gratitude and esteem, not only for his guidance in scientific work but also for the deep human experience he inspired.*

I express the same feelings to all the co-workers of the research group, Dr. Hamish Miller, Dr. Andrea Marchionni, Dr. Jonathan Filippi, Dr. Manuela Bevilacqua, Dr. Werner Oberhauser and Dr. Alessandro Lavacchi all of them gave me support and help in my research, in addition they trained me to use sophisticated laboratory instruments and they helped me in writing my thesis. I also want to thank Lianqin Wang, Maria Folliero, Maria Pagliaro e Jacopo Ruggeri: they shared their office with me during this long but short time.

Last but not least, many thanks to my "ICCOM friends": Dr. Gabriele Manca, Dr. Maria Caporali, Dr. Lorenzo Zani, Dr. Andrea Ienco, Dr. Giulia Tuci, Dr. Samuele Staderini, Dr. Irene Mellone, Dr. Manuel Serrano, Dr. Lapo Luconi, Carlo Bartoli, and my doctorate school colleagues Alessio, Vanessa, Fuencisla, Matteo and Salvatore. All these persons make ICCOM a place of science and friendship.

I can't forget my family, my fiancée, and all my friends: without their support I could not have reached this goal.